Chapter 5: Palladium Nanostructures and Nickel-Palladium Nanostructures Stabilized on Iron Oxide Nanoparticles Capped with Diethylenetriamine Pentaacetic acid: Preparation, Characterization and Applications

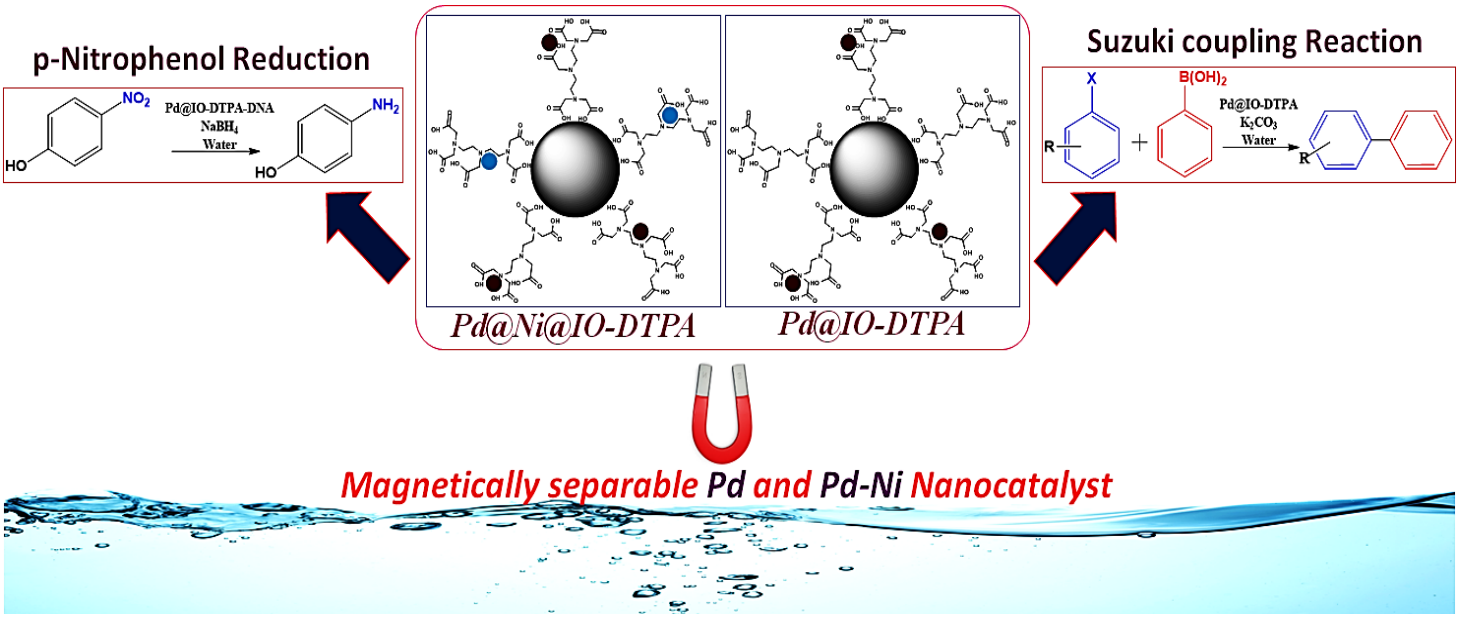

5.1. Introduction

Surface modification with appropriate capping agents offers better dispersion of the nanomaterials in appropriate solvents, and thus better performance can be anticipated in various applications. Additionally, these surface-modified nanomaterials can be employed as noble metal supports to develop heterogeneous catalysts that are more accessible to the reactants(Guin et al., 2007). Aminopolycarboxylic acids are able to form strong complexes with metal ions by donation of electron pairs from nitrogen and oxygen atoms to the metal ion to form multiple chelate rings. This property makes aminopolycarboxylic acid based ligands such as Ethylenediaminetetraacetic acid (EDTA) and Diethylenetriaminepentaacetic acid (DTPA) as versatile capping agents for metal ions and forms the basis of their applications in a wide variety of chemical, medical and environmental processes(Li et al., 2019; Malkar et al., 2014).

Esmaeilpour et al have prepared palladium nanoparticles supported on EDTA-modified Fe_3O_4@SiO_2 nanospheres and used it for Suzuki coupling and Sonogashira coupling reactions (Esmaeilpour et al., 2018). Fe_3O_4@SiO_2-EDTA-Pd catalyst showed very low TON and recyclability upto 10 cycles with successive decrease in yield after 5^{th} cycle. Heydari at al synthesized Pd(II) anchored onto ethylenediaminetetraacetic acid-coated Fe_3O_4. Its catalytic activity was checked for Nitroarene reduction and Suzuki–Miyaura coupling reaction. They got recyclability with successive decrease in yield upto 5 cycles(Azizi et al., 2015)

Nanoparticles with superparamagnetic properties are a new class of environmentally friendly catalysts support for organic transformation reactions(Stevens et al., 2005) as they can be rapidly isolated, easily recovered (Guin et al., 2007; Jinhui Tong et al., 2016; Khazaei et al., 2017) and can be utilised to immobilise Pd catalysts having the properties of heterogeneity and magnetic separability. It is possible to create magnetic nanoparticles from a variety of materials, including Fe, Co, and Ni alloys, FePt and CoPt; and ferrites, $CoFe_2O_4$, $MnFe_2O_4$, $CuFe_2O_4$, and $ZnFe_2O_4$. The majority of magnetic reusable nano-catalysts in use are metal oxides, including iron(II) oxide (FeO), magnetite (Fe_3O_4), and maghemite (γ-Fe_2O_3). Due to its ease of production (Sydnes, 2017). Magne O. Sydnes has prepared palladium on magnetic supports (Iron oxide nanoparticles) and used it as a catalyst for Suzuki Miyaura cross coupling reaction(Sydnes, 2017). Singh et. al., fabricated Palladium(II) on Schiff base functionalized $NiFe_2O_4$ and used it as phosphine-free heterogeneous catalyst for Suzuki Coupling reactions(Singh et al., 2015). Dehghani et al., synthesized magnetic zeolite Y–palladium–nickel ferrite by ultrasonic irradiation for application as a catalyst in Suzuki coupling reaction (Dehghani et al., 2019). Ghanbari et. al. prepared

palladium-nickel/iron oxide core–shell nanoalloy via ultrasonic assisted method and utilized it for Suzuki-Miyaura coupling and p-nitrophenol reduction (Ghanbari et al., 2017).

In the present chapter, we have reported the synthesis of magnetic Pd based metallic and Pd-Ni based bimetallic nanocatalyst through Diethylenetriamine Pentaacetic acid functionalized iron oxide nanoparticles (IO- DTPA & Ni@IO-DTPA).

The use of DTPA with multiple carboxyl groups not only facilitated the fabrication of capped Iron Oxide nanoparticles and Nickel doped Iron Oxide nanoparticles (IO- DTPA & Ni@IO-DTPA) but also provided active sites for the further immobilization of Pd to fabricate a magnetically recoverable nanocatalyst (Pd@IO-DTPA & Pd@Ni@IO-DTPA).

Synthesized Pd@IO-DTPA and (Pd@Ni@IO-DTPA) nanocatalysts were characterized by Transmission Electron Microscopy, Scanning Electron Microscopy, Energy Dispersive X-ray Spectroscopy, X-ray Diffraction, Vibrating Sample Magnetometer, Electron Spin Resonance Spectroscopy, X-Ray Photoelectron Spectroscopy and X-ray Absorption Near Edge Structure techniques. The effectiveness of Pd@IO-DTPA, Pd@Ni@IO-DTPA as catalysts for p-Nitrophenol reduction and Suzuki cross coupling reaction of aryl halides and aryl boronic acids was investigated. The catalysts could be recovered using a simple magnet. Simplicity of design, low cost of fabrication, high efficiency and extensive reusability make Pd@IO-DTPA, Pd@Ni@IO-DTPA promising catalysts for Suzuki coupling reaction.

5.2. Materials and methods

5.2.1. Materials

All chemicals were purchased as analytical grade from commercial suppliers and were used without further purification**.** DTPA was purchased from Spectrochem Pvt. Ltd. The synthesized nanoparticles were first dried in oven at 100°C and then used for further analysis

5.2.2. Procedure for the preparation of DTPA capped Iron oxide nanoparticles (IO-DTPA)

Magnetic nanoparticles IO-DTPA were prepared in alkaline condition at room temperature. About 0.96 g $FeSO_4 \cdot 7H_2O$ was dissolved in 10 mL 5% HCl and stirred for 10 min followed by the addition of 1.12g $FeCl_3.2H_2O$ and further stirring for 10 min. To this solution, 3 mL of DTPA solution (prepared by dissolving 0.1g DTPA in 3 ml 0.1M NaOH) was added drop wise and stirred for 30 min. The pH of the resultant solution was adjusted to 10 by the dropwise addition

of 25ml of 50% ammonia solution and the mixture was stirred at RT (30-35 °C) for 3 hours. The resultant black precipitates of IO-DTPA were separated using an external magnet and washed with water until neutral followed by10 mL acetone and then dried in oven at 100 °C for 7-8 h.

5.2.3. Procedure for the immobilization of Palladium on DTPA capped Iron oxide nanoparticles (Pd@IO-DTPA)

For the preparation of Pd@IO-DTPA, 100 mg IO-DTPA was sonicated in 20 mL ethanol for 20 min followed by the addition of 2 mg $PdCl_2$ to the suspension with gentle stirring at RT (30-35 °C) for 12h. The resultant Pd@IO-DTPA nanoparticles were separated with a handheld magnet, washed with ethanol and finally dried at 100 °C for 5 h.

5.2.4. Preparation of DTPA capped Nickel doped Iron oxide nanoparticles (Ni@IO-DTPA)

The synthesis of Ni@IO-DTPA was performed using chemical precipitation method. In a round bottom flask 0.96g $FeSO_4 \cdot 7H_2O$ was dissolved in 10 mL of 5% HCl solution and stirred for 10 min followed by the addition of 1.12 g $FeCl_3.2H_2O$ and further stirring for 10 min. Subsequently 0.1 g DTPA dissolved in 3 mL 0.1M NaOH solution was added drop wise and stirred for 30 min. The pH of the resulting solution was raised to 10 by dropwise addition of 25mL of 50% ammonia solution and stirred for 3 h which resulted in precipitation of black particles. After 3 h of stirring, 0.3M 3 mL $NiCl_2.6H_2O$ solution was added dropwise and stirred for another 3 h(Ahmad et al., 2015). The black particles of Ni@IO-DTPA were collected using an external magnet and washed with 100 mL water followed by 10 mL acetone and then dried in an oven at 100 °C for 7-8 h.

5.2.5. Procedure for the immobilization of Palladium on DTPA capped Nickel doped Iron oxide nanoparticles (Pd@Ni@IO-DTPA)

Pd@Ni@IO-DTPA nanoparticles were prepared by sonicating a suspension containing 100 mg Ni@IO-DTPA in 20 mL ethanol for 10 min. Subsequently, 2 mg $PdCl_2$ was added to Ni@IO-DTPA suspension with gentle stirring for 12 hours at room temperature. The resultant Pd@Ni@IO-DTPA nanoparticles were collected with a magnet, washed with 10 mL EtOH followed by 5 mL water and was finally oven dried at 100 °C for 5 h.

5.2.6. General method for p-Nitrophenol reduction catalysed by Pd@IO-DTPA and Pd@Ni@IO-DTPA

25 mg/L of the p-NP solution was prepared with conductivity water. In a 100 mL conical flask, 50 mL of 25 ppm p-NP solution, $NaBH_4$ (optimized amount: 10 mg for Pd@IO-DTPA and 9 mg for Pd@Ni@IO-DTPA) and 1 mg of the catalysts were added. The solutions were mixed by shaking before each measurement. The reduction reaction was monitored using UV–Vis absorption spectrophotometer within a range of 200 to 600 nm at different time intervals. A color change of the solution from bright yellow to colorless was observed.

The reusability of the catalyst was tested by a scale-up experiment with 10 mg of catalyst maintaining the same ratio of catalyst/p-NP. The catalyst was separated by hand held magnet, and washed twice in 20 mL conductivity water and 1 mL acetone, and then placed in a drying oven to dry for 5 h (at 100 °C) and then used for the next run.

5.2.7. General procedure for the Suzuki coupling reaction catalysed by Pd@IO-DTPA and Pd@Ni@IO-DTPA

The coupling reaction was carried out by taking 1.59 mmol each of aryl halide, arylboronic acid, K_2CO_3, 1 mg of catalyst under study and 10 mL H_2O in a 25 mL round-bottomed flask and heated on an oil bath at 90-100 °C with stirring for 6 to 15 h depending on the aryl halides used. The reaction was monitored by TLC. After completion of the reaction, the mixture was cooled to room temperature and the catalyst under study was collected by an external magnet. Subsequently, the mixture was extracted with ethyl acetate three times (3*5 mL). The ethyl acetate phase was then collected, dried with Na_2SO_4 and coupled products were obtained by evaporation which were further analysed by GC-MS. Crude product was purified using column chromatography packed by silica gel to obtain the desired product. NMR spectra of the purified products are given in the Supporting Information.

To test the recyclability of catalyst, after each cycle catalyst was separated by using an external magnet, washed twice with 10 mL conductivity water and ethyl acetate and further dried in an oven at 100°C for 5 h. The recovered catalyst was further used for the next cycle of reaction.

5.2.8. Characterization of synthesized nanosystems (Pd@IO-DTPA and Pd@Ni@IO-DTPA)

The structural and morphological properties of Pd@IO-DTPA and Pd@Ni@IO-DTPA were analysed by using the techniques such as, UV-Vis, IR, XRD, SEM, EDX, VSM, HRTEM, XPS, HRTEM, TG-DTA and XANES techniques as discussed in described in chapter 2 section 2.2.6

Fe K-edge XANES spectra were recorded at room temperature in the transmission mode using procedure described in chapter 3. VSM Spectra recorded on Lakeshore VSM 7410 magnetometer using procedure mentioned in chapter 3 section 3.2.8. The palladium and iron content in the catalyst and leaching study were performed by using PerkinElmer ICP-MS, NexION 2000 spectrometer. GC-MS spectra of crude products obtained after coupling reaction were recorded on Thermo fisher trace ultra GC model. NMR Spectra of column purified biphenyl products were recorded on Bruker avance III spectrometer operating at 600 MHz in $CDCl_3$ solvent using procedure described in chapter 3 section 3.2.8.

5.3. Result and Discussion

5.3.1. Characterization Studies of Pd@IO-DTPA and Pd@Ni@IO-DTPA

5.3.1.1. IR Spectra

The FT-IR spectra of the IO-DTPA, Pd@IO-DTPA, Ni@IO-DTPA and Pd@Ni-IO-DTPA are depicted in Figure 5.1. All characteristic peaks of DTPA and iron oxide were present in the FT-IR spectra of all the 4 compounds.

The bands at 630, 560 cm^{-1} in IO-DTPA, at 632, 558 cm^{-1} in Pd@IO-DTPA, 638, 580 cm^{-1} in Ni@IO-DTPA and 631, 579 cm^{-1} in Pd@Ni@IO-DTPA are ascribed to the stretching vibration of Fe-O (M_{Th}-O-M_{Oh} of the tetrahedral and octahedral sites) confirming the existence of magnetic nanoparticles (Amirmahani et al., 2021). Further the band at 443 cm^{-1} may be attributed to the Fe-O stretching mode of octahedral sites of maghemite(Arumugam et al., 2020).

FTIR spectra of synthesized DTPA-coated NPs have characteristic peaks in the spectral region from 900 to 1800 cm^{-1}. The presence of IR bands originating from the vibration of chemical bonds in the DTPA structure clearly confirm the formation of IO-DTPA and Ni@IO-DTPA providing many carboxylate groups facilitating further functionalization with Pd.

The vibrational bands observed at 1045 cm^{-1} and 978 cm^{-1} in the spectrum of DTPA can be assigned to the ν(C-N) and C-C stretching vibrations respectively. The bands observed at 3167 and 3382 cm^{-1} were ascribed to ν(C-H) and ν(O-H) stretching vibrations respectively. The bands

at 1406 cm^{-1}, 1218 cm^{-1} and 1127 cm^{-1} were attributed to $–CH_2$ and C–H stretching and wagging vibration modes respectively while the peak at 2856 cm^{-1} corresponded to the N–C–H asymmetric stretching. The peak observed at ~1625 cm^{-1} was attributed to the C=O stretching vibration of acetyl group and that observed at 1475 cm^{-1} to C=O and C–OH stretching vibrations (Silva, Carvalho, Freitas, Tormena, & Melo, 2007; Silva, Carvalho, Freitas, Tormena, & Walcl´ee C. Melo, 2007).

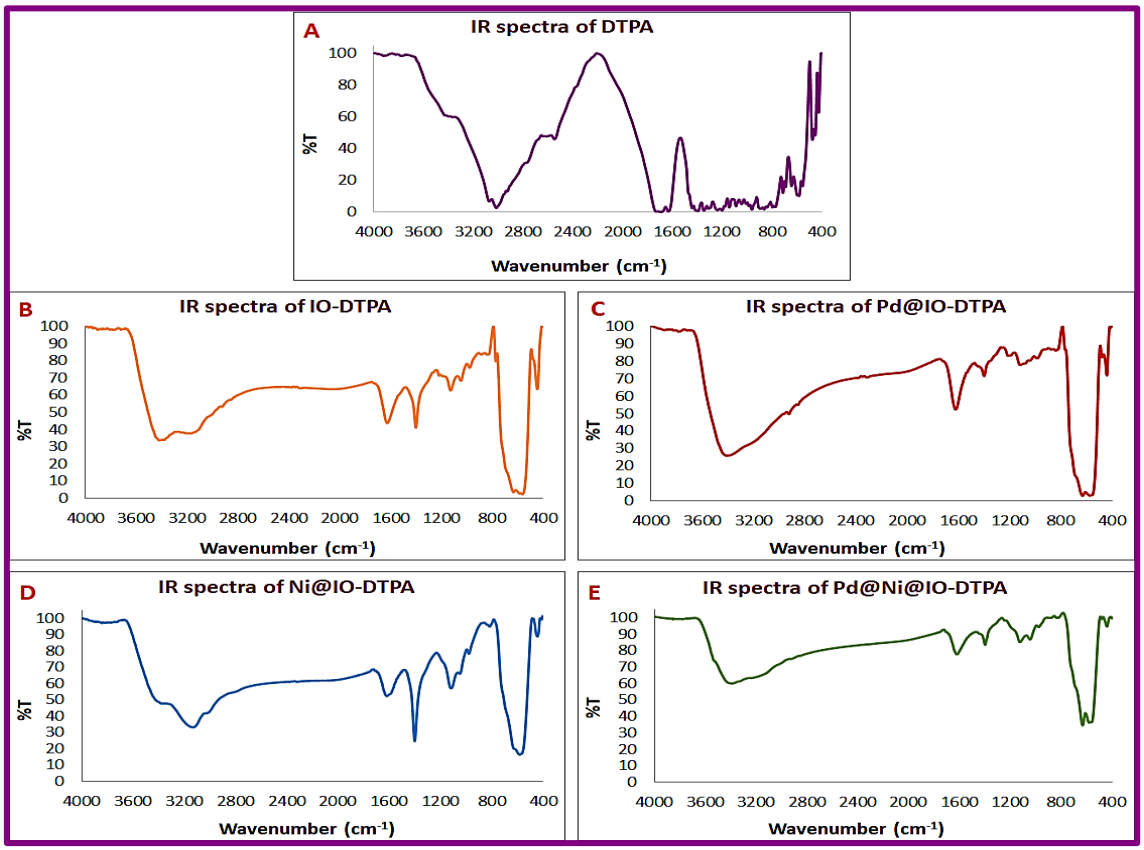

Figure 5.1: *IR spectra of (A) DTPA, (B) IO-DTPA, (C) Pd@IO-DTPA, (D) Ni@IO-DTPA, (E) Pd@Ni@IO-DTPA.*

The presence of IR bands originating from the vibration of chemical bonds of DTPA in IO-DTPA clearly confirm the capping of DTPA on IO providing many carboxylate groups facilitating further functionalization with Ni and or Pd. The IR spectra of IO-DTPA, Pd@IO-DTPA, Ni@IO-DTPA, Pd@Ni@IO-DTPA exhibited bathochromic shifts for C-O and C-N bands when compared to pristine DTPA, indicating that nitrogen and oxygen are sites for stabilization. The diminishing and shifting of peaks attributed to N-C-H, C-OH, C-N in Pd@IO-DTPA and Pd@Ni@IO-DTPA as compared to IO- DTPA and Ni@IO-DTPA respectively confirm the binding of Pd.

5.3.1.2. ICP-MS, SEM-EDX and TEM

The Pd and Fe content of Pd@IO-DTPA estimated by ICP-MS were observed to be 0.669 wt% and 54.26 wt% respectively while the Pd, Ni and Fe content of Pd@Ni@IO-DTPA estimated by ICP-MS were observed to be 1.109 wt%, 0.661 wt% and 47.41 wt% respectively.

The morphology and elemental composition were further investigated by SEM-EDX mapping (Figure 5.2 (B, E, H, K)).

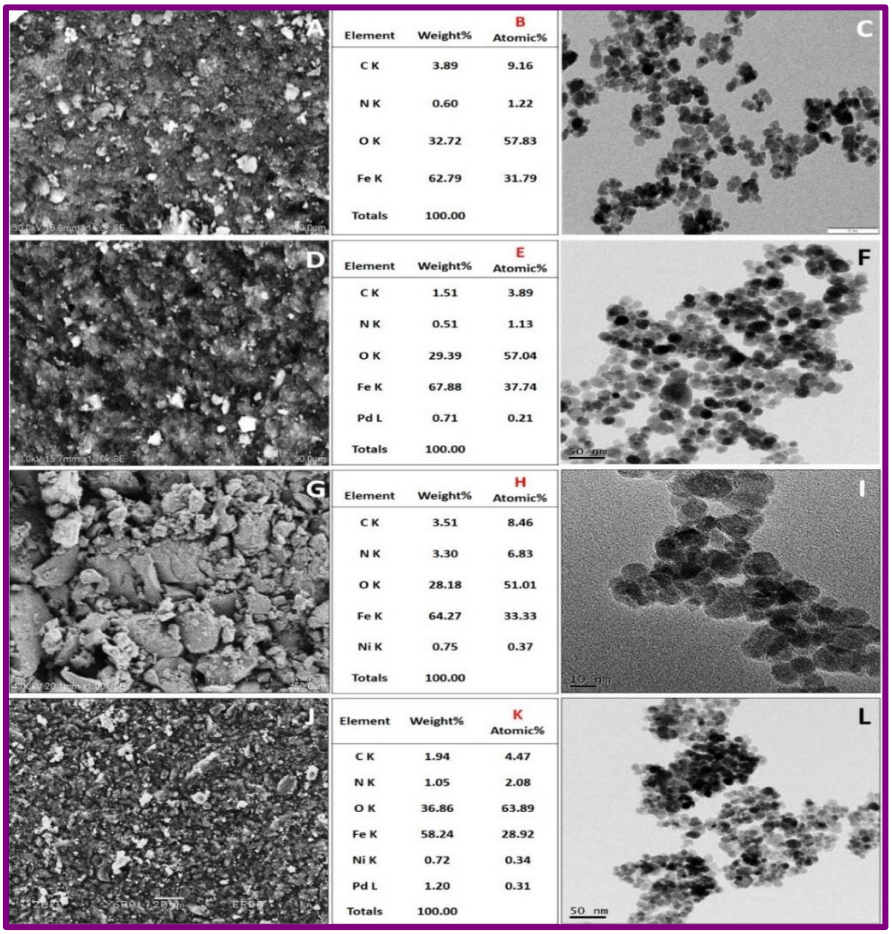

Figure 5.2: *(A) SEM image of IO-DTPA, (B) EDS of IO-DTPA, (C) TEM image of IO-DTPA, (D) SEM image of Pd@IO-DTPA, (E) EDS of Pd@IO-DTPA, (F) TEM image of Pd@IO-DTPA, (G) SEM image of Ni@IO-DTPA, (H) EDS of Ni@IO-DTPA, (I) TEM image of Ni@IO-DTPA, (J) SEM image of Pd@Ni@IO-DTPA, (K) EDS of Pd@Ni@IO-DTPA, (L) TEM image of Pd@Ni@IO-DTPA.*

The EDX spectrum confirmed the presence of C (3.89 wt%), N (0.6 wt%), O (32.72 wt%) and Fe (62.79 wt%) in IO-DTPA; C (1.51 wt%), N (0.51 wt%), O (29.39 wt%), Fe (67.88 wt%), and Pd (0.71 wt%) in Pd@IO-DTPA; C (3.51 wt%), N (3.30 wt%), O (28.18 wt%), Fe (64.27 wt%), Ni (0.75 wt%) in Ni@IO-DTPA; C (1.94 wt%), N (1.05 wt%), O (36.86 wt%), Fe (58.24 wt%),

Ni (0.72 wt%) and Pd (1.20 wt%) in Pd@Ni@IO-DTPA. The EDX mapping of Pd@IO-DTPA and Pd@Ni@IO-DTPA indicated uniform dispersion of palladium on IO-DTPA. Further, ICP-MS and EDX results indicated greater percent (165%) of Pd in Pd@Ni@IO-DTPA as compared to Pd@IO-DTPA

As shown in TEM images (Figure 5.2(C, F, I, L)), the size of the synthesized magnetic particles IO-DTPA ranged from 15-25 nm while that of Pd@IO-DTPA ranged from 15 to 30 nm. The particle size of Ni@IO-DTPA ranged from 7-15 nm and Pd@Ni@IO-DTPA ranged from 8-25 nm. The magnetic nanoparticles with near sphere-shaped morphology and monodispersity were observed.

Particle size of all the 4 nanosystems are less than 15 nm. One of the important reasons behind this observation is the use of DTPA as a capping agent which plays an important role in stability of the synthesized nanoparticles. Plausible mechanism involves covalent bond formation between surface of the particles and DTPA, causing steric hindrance between particles and the resultant stability(Rahal et al., 2017).

5.3.1.3. HRTEM and SAED images

High Resolution Transmission Electron Microscopy (HRTEM) images and Selective Area Electron Diffraction (SAED) patterns were obtained to provide morphology, particle size and structural information of Pd@IO-DTPA and Pd@Ni@IO-DTPA (Esmaeilpour et al., 2018).

The HRTEM images (Figure 5.3 (B & F)) of Pd@IO-DTPA and Pd@Ni@IO-DTPA, depicted the preferential mono deposition of palladium on IO-DTPA and Ni@IO-DTPA respectively. Regular fringes (Figure 5.3B) were clearly observed in Pd@IO-DTPA with a spacing of 0.253 nm and 0.3 nm indicating (311), (220) planes of Fe_3O_4 respectively (Lara & José G. Carriazo, 2019; Predoi et al., 2010) and 0.22 nm (111) plane of Pd (Vats et al., 2016). The fringes in Pd@Ni@IO-DTPA (Figure 5.3F) with a spacing of 0.24 nm, was attributed to (311) plane and 0.29 nm to (220) interplanar distance of the maghemite while 0.246 nm was attributed to (111) plane of NiO (Predoi et al., 2010) and 0.20 nm to (311) plane of Pd (Vats et al., 2016).

The SAED pattern of IO-DTPA (Figure 5.3A) exhibited diffraction rings indexed to (220), (222), (400), (422), (511) and (440) planes of Fe_3O_4 (JCPDS 88-0315) and γ-Fe_2O_3 (JCPDS No. 39-1346). In addition to diffraction rings of iron oxide, the SAED pattern of Pd@IO-DTPA (Figure 5.3C) exhibited (111) and (200) planes of fcc Pd nanocrystallites as well as (100), (101) and (112) diffraction planes of PdO.

The SAED pattern of Ni@IO-DTPA (Figure 5.3E), was indexed to Fe_3O_4 (JCPDS 88-0315) and γ-Fe_2O_3 (JCPDS No. 39-1346) with the diffraction rings being attributed to the (111), (220), (311), (222), (400), (422) and (511) planes as well as (111) plane of Ni. The diffraction ring of (311) plane was most intense, compared with the other rings, which reflected the preferred direction of nanocrystal growth. The SAED pattern of Pd@Ni@IO-DTPA (Figure 5.3G) corresponded to Iron oxide (maghemite and magnetite), Ni, Pd and PdO. The ring pattern exhibited (111) and (200) planes of fcc Pd and (100) and (112) diffraction planes of PdO and (111) of Pd(Ni).

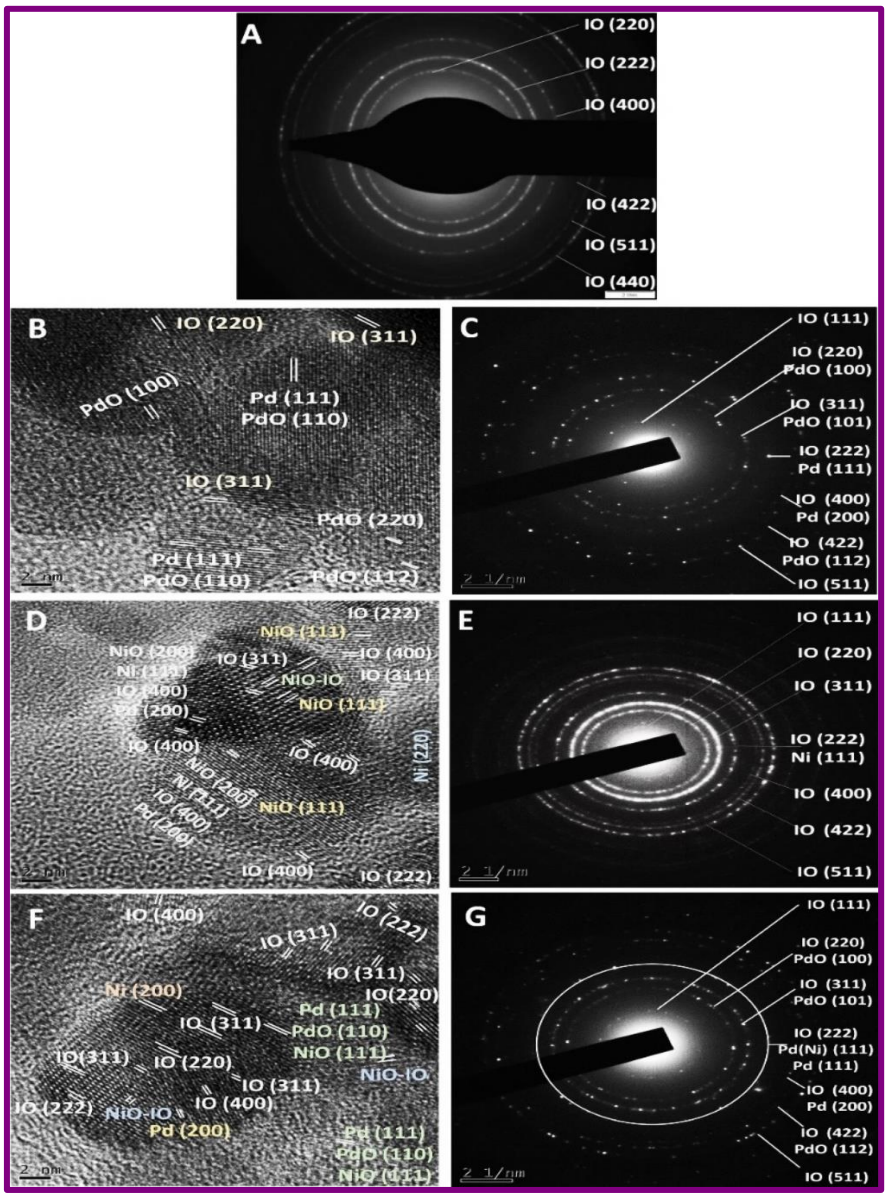

Figure 5.3: *(A) SAED image of IO-DTPA, (B) HRTEM image of Pd@IO-DTPA, (C) SAED image of Pd@IO-DTPA, (D) HRTEM image of Ni@IO-DTPA, (E) SAED image of Ni@IO-DTPA, (F) HRTEM image of Pd@Ni@IO-DTPA, (G) SAED image of Pd@Ni@IO-DTPA*

5.3.1.4. HAADF-STEM

The high-angle annular dark-field scanning transmission electron microscopy (HAADF-STEM) micrographs of Pd@Ni@IO-DTPA (Figure 5.4) and their corresponding energy dispersive X-ray spectroscopy (EDS) mappings (Figure 5.4(B-F)) show that Pd, Fe and Ni were well dispersed. Further, bimetallic character of the nanocatalyst Pd@Ni@IO-DTPA was confirmed as both the Ni and Pd were observed in the micrograph adjacent to each other.

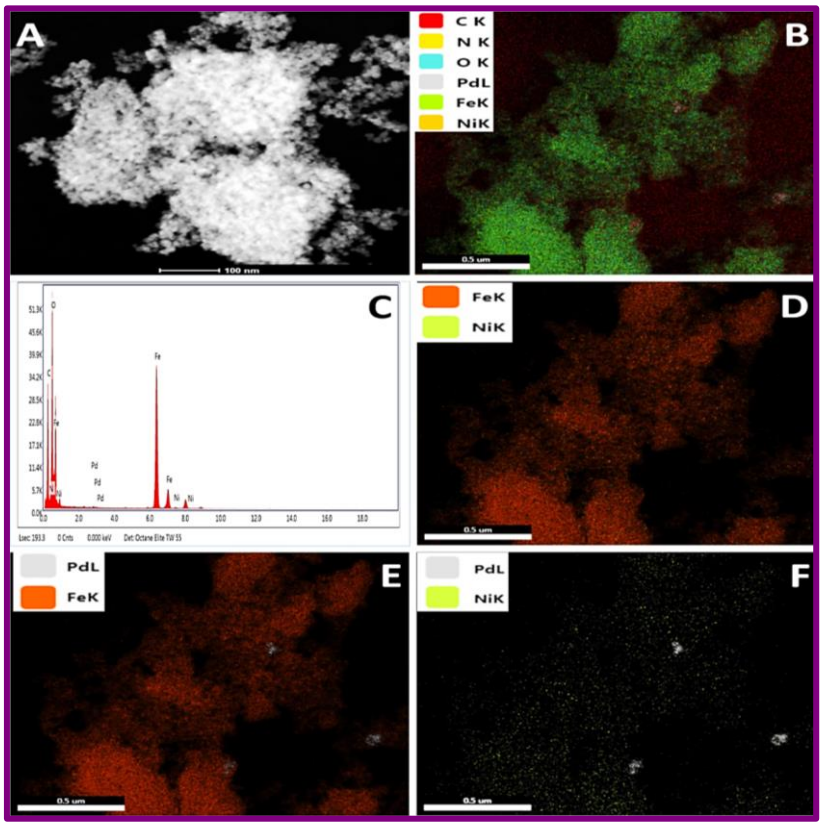

Figure 5.4: *(A) STEM image of Pd@NiFe$_2$O$_4$-DTPA (B-F) HAADF mapping of Pd@Ni@IO-DTPA*

5.3.1.5. XRD Spectra

The lattice parameters, crystallite domain size and phase composition of IO-DTPA, Pd@IO-DTPA, Ni@IO-DTPA, Pd@Ni@IO-DTPA were investigated with X-ray powder diffraction (XRD) and it confirms the nano-crystalline structure of the catalyst. (Figure 5.5)

The characteristic XRD diffraction peaks observed at 2θ= 30.1°, 35.5°, 43.1°, 54.5°, 57.6° and 63.6° for IO-DTPA were attributed to (220), (311), (400), (422), (511) and (440) crystal faces of Fe_3O_4 spinel structure (Predoi et al., 2010). The characteristic diffraction peaks of iron oxide were observed in Pd@IO-DTPA along with two diffractions positioned at 2θ of 40.1°,46.7° attributed to (111) and (200) crystalline planes of face centered Pd nanoparticles in good

agreement with (JCPDS file number 46-1043)(Vats et al., 2016). Further, the (200) plane of PdO was observed at 2θ 59.9°(Ganji et al., 2013) indicating that Pd existed as both Pd(0) and PdO. This is in good agreement with the HRTEM and SAED analysis.

The XRD pattern of the Ni@IO-DTPA (Figure 5.5C) catalyst exhibited the characteristic peaks of IO, Ni and NiO. In addition to IO peaks, XRD peaks were observed at 2θ of 42.64° and 51.75° corresponding to (111) and (200) planes of Ni(0), and at 2θ 32.51°, 72.61 which were attributed to (111), (311) planes of NiO (Richardson et al., 2003). As shown in Figure 5.5D the XRD pattern of the Pd@Ni@IO-DTPA catalyst shows the characteristic peaks of IO NPs mainly as well as Ni and NiO. Besides the characteristic peaks of IO, Ni and NiO, additional weak peaks were observed at 40.1°, 46.7° which were well-indexed to the (111) and (200) crystalline plane of face centred Pd nanoparticles (Qi et al., 2014), though the peaks are weak due to dispersion and low concentration. Further, (200) plane of PdO was observed at 2θ 59.9°(Ganji et al., 2013) indicating presence of Pd in the form of Pd(0) and PdO.

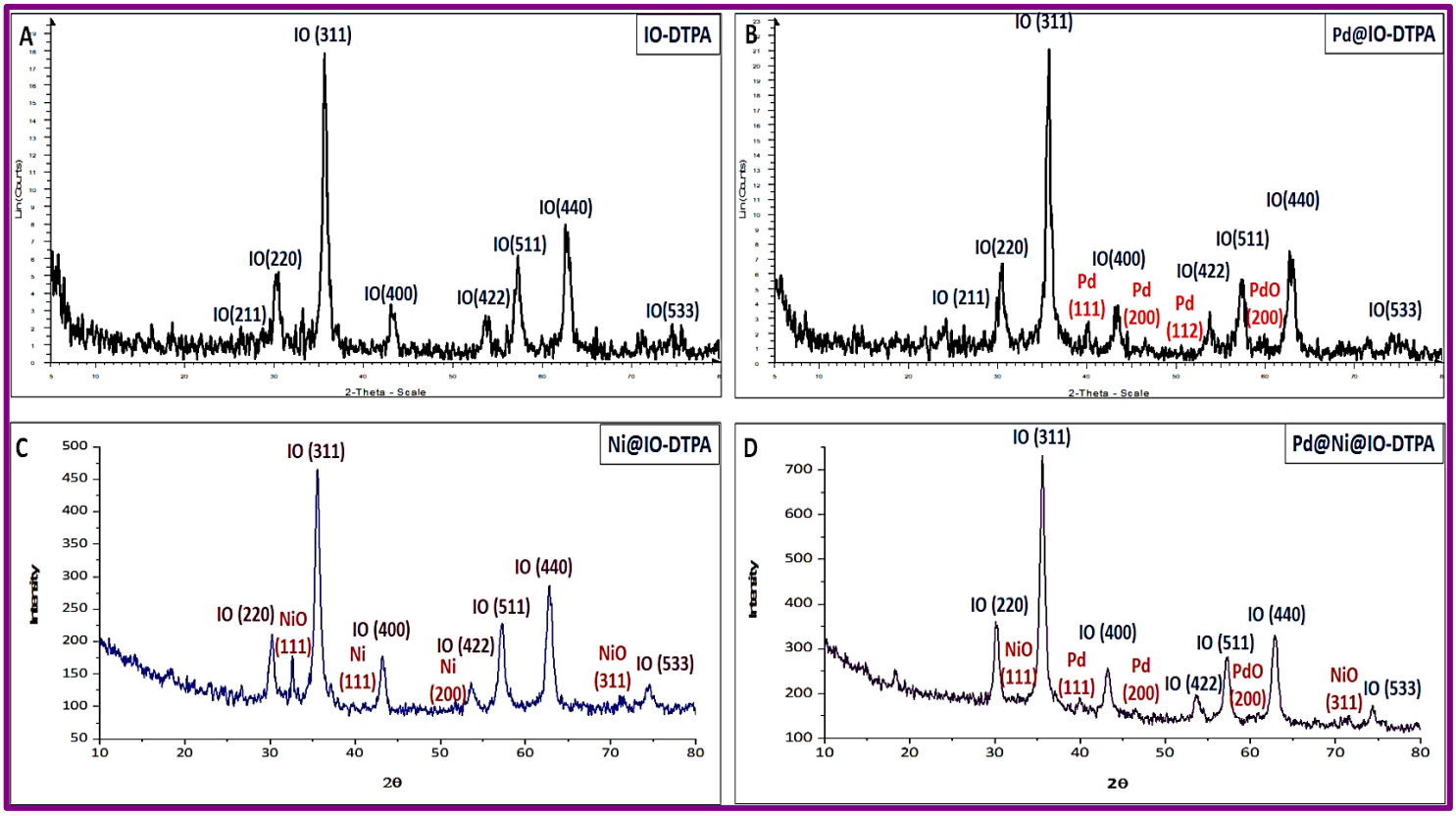

Figure 5.5: *(A) XRD spectra of IO-DTPA, (B) XRD spectra of Pd@IO-DTPA, (C) XRD spectra of Ni@IO-DTPA and (D)XRD spectra of Pd@Ni@IO-DTPA*

5.3.1.6. XPS analysis

The IO-DTPA, Pd@IO-DTPA, Ni@IO-DTPA and Pd@Ni@IO-DTPA were further evaluated by X-ray photoelectron spectroscopy (XPS). (Figure 5.6 -Figure 5.9). In addition to the peaks of Fe (2p), O (1s), C (1s) and N (1s) signals, a peak associated with Pd (3d) was observed in XPS spectrum of Pd@IO-DTPA, indicating the successful formation of Pd@IO-DTPA.

C(1s) spectrum of IO-DTPA (Figure 5.6A) exhibited 2 peaks at 284.6 and 286.08 eV attributed to binding energies of C-C/C-H and C-N bonds respectively. IO-DTPA also exhibited a N(1s) (Figure 5.6 B) binding energy peak at 399.74 eV, which corresponded to the tertiary amine group in DTPA. The O(1s) XPS spectra (Figure 5.6C) exhibited a peak at 530.4 eV that can be attributed to Fe-O bond and the peak at 532.6 eV can be attributed to C=O bond binding energies respectively. The Fe(2p1/2) peak (Figure 5.6D) was observed at 724.9eV. The absence of satellite peak at about 715 eV attributed to Fe^{2+} suggested the presence of maghemite phase(Fondell et al., 2018).

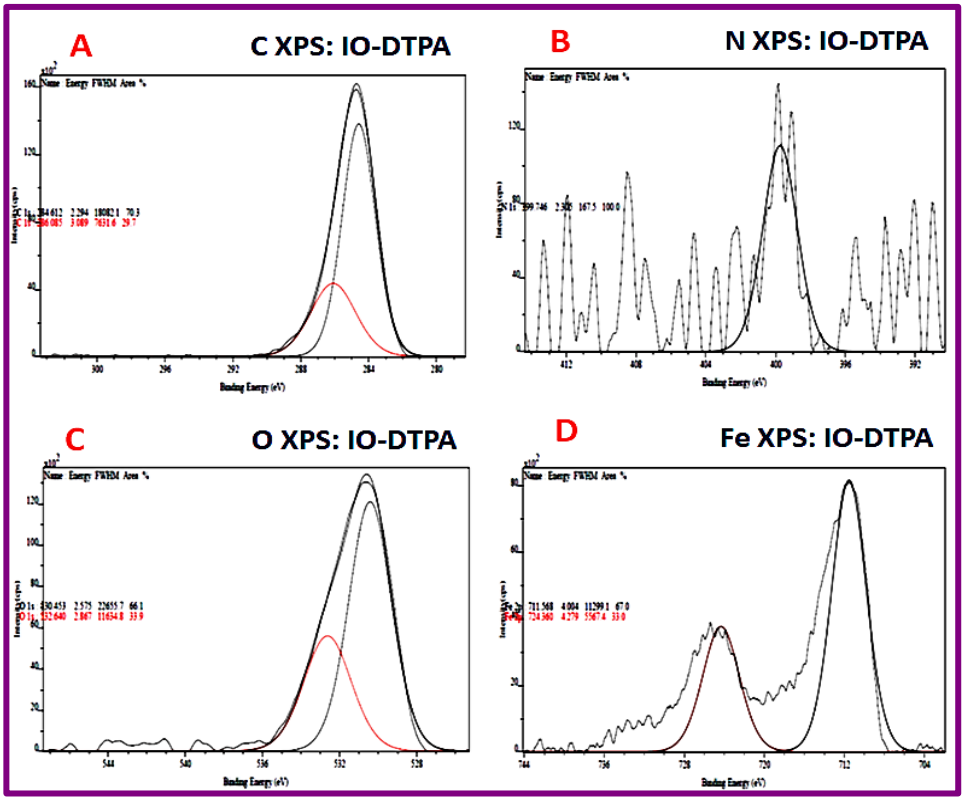

Figure 5.6: *C, N, O, Fe XPS spectra of IO-DTPA*

The Pd@IO-DTPA, survey spectrum confirmed the presence of (13.25 At%) C, (1.06 At%) N, (69.18 At%) O, (16.32 At%) Fe, (0.20 At%) Pd. The deconvoluted peaks of C(1s) (Figure 5.7A) presented 3 characteristic peaks with binding energies at 284.6, 286.08, 288.15 eV attributed to

C-C/C-H, C-N and O-C=O bonds respectively. The Nitrogen 1s spectra (Figure 5.7B) displayed binding energy at 400.98 eV representing C-N bond(Ma et al., 2021; Ravi et al., 2018; Wang et al., 2020). Similarly, O1s (Figure 5.7C) spectra exhibited peaks with binding energies at 530, 531.66, 533.05 eV that were ascribed to Fe-O/Pd-O, C=O, and C-O-C bonds(Yamashita & Hayes, 2008; Zhao et al., 2017a) respectively. The deconvoluted Fe 2p XPS spectra (Figure 5.7D) exhibited a peak at 710.25 eV attributed to octahedral Fe^{3+}(2p 3/2) of γ- Fe_2O_3 and α-Fe_2O_3 while the satellite peak of Fe^{3+} and Fe^{3+}(2p1/2) were observed at 720.44 eV, and 723.25 eV respectively. The peak at 713.94 eV can be attributed to tetrahedral Fe^{3+} in Fe_3O_4.

The Pd XPS spectra (Figure 5.7E) with peaks at binding energies of 335.4 eV and 340.5 eV were assigned to Pd(0) 3d5/2 and 3d3/2 orbitals with a spin orbit splitting of 5.1eV. The Pd 3d5/2 peak observed at 336.35eV was attributed to Pd^{2+} (Peuckert, 1985) while that observed at 338.58 eV was attributed to nanoclusters bound to the support (Kumaresan et al., 2008). The partial formation of Pd(0) species in the catalyst without the use of any additional reducing agent can be attributed to the presence of electron rich O and N in the network support which may donate electrons to Pd(II). Thus, from deconvoluted Pd XPS analysis confirmed that Pd is present at (42.17%) Pd(0), (36.2%) Pd^{2+} and (21.63%) PdO.

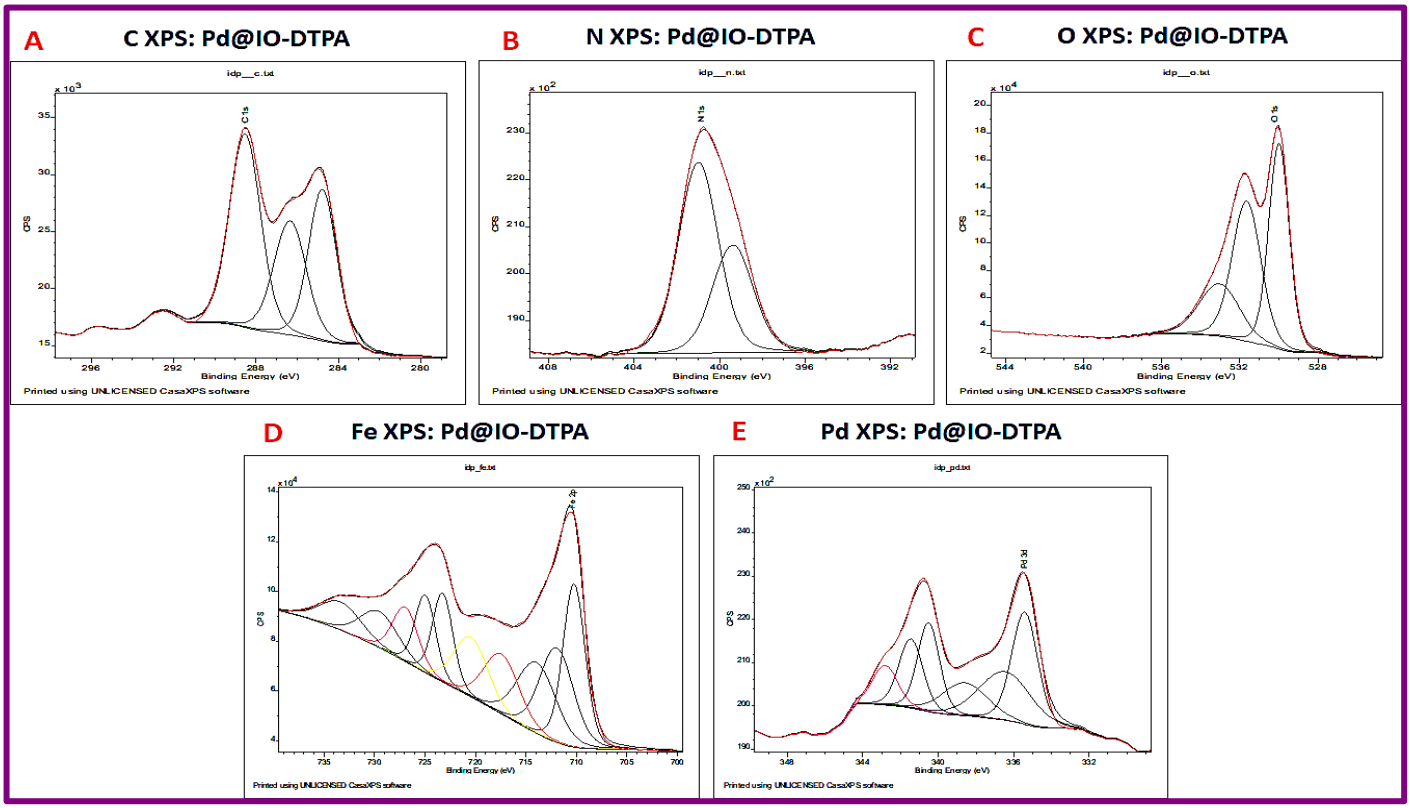

Figure 5.7*: C, N, O, Fe and Pd XPS spectra of Pd@IO-DTPA*

The de-convoluted C 1s, N 1s, O1s, Fe 2p and Ni 2p XPS spectra of Ni@IO-DTPA are shown in Figure 5.8. In the Fe2p XPS spectrum (Figure 5.8D), the signals at binding energies of about 709.98, 713.37 and 722.98 eV, 726.37 were assigned to Fe2p3/2 and Fe2p1/2 of Fe^{3+} ions along with satellite peaks. Ni 2p XPS spectra of Ni@IO-DTPA (Figure 5.8E) exhibited peaks at 852.61 eV assigned to Ni(0) and 854.40 eV to NiO. The de-convoluted O1s peak (Figure 5.8C) at binding energy 530 eV was attributed to bulk Fe-O, while the peak at 531.12 eV was attributed to O-H bond and 532.65 eV to C=O. Further, the assignment for N1s de-convoluted peaks (Figure 5.8B)with binding energy 400.97 eV was made to C-N(Ma et al., 2021). In the C 1s spectrum (Figure 5.8A) the peak with binding energy 284.5 eV was attributed to C-C/C-H, 285.48 eV to C-O, 286.34 eV to C-N and 288.23 eV to -COOH(Xu et al., 2019).

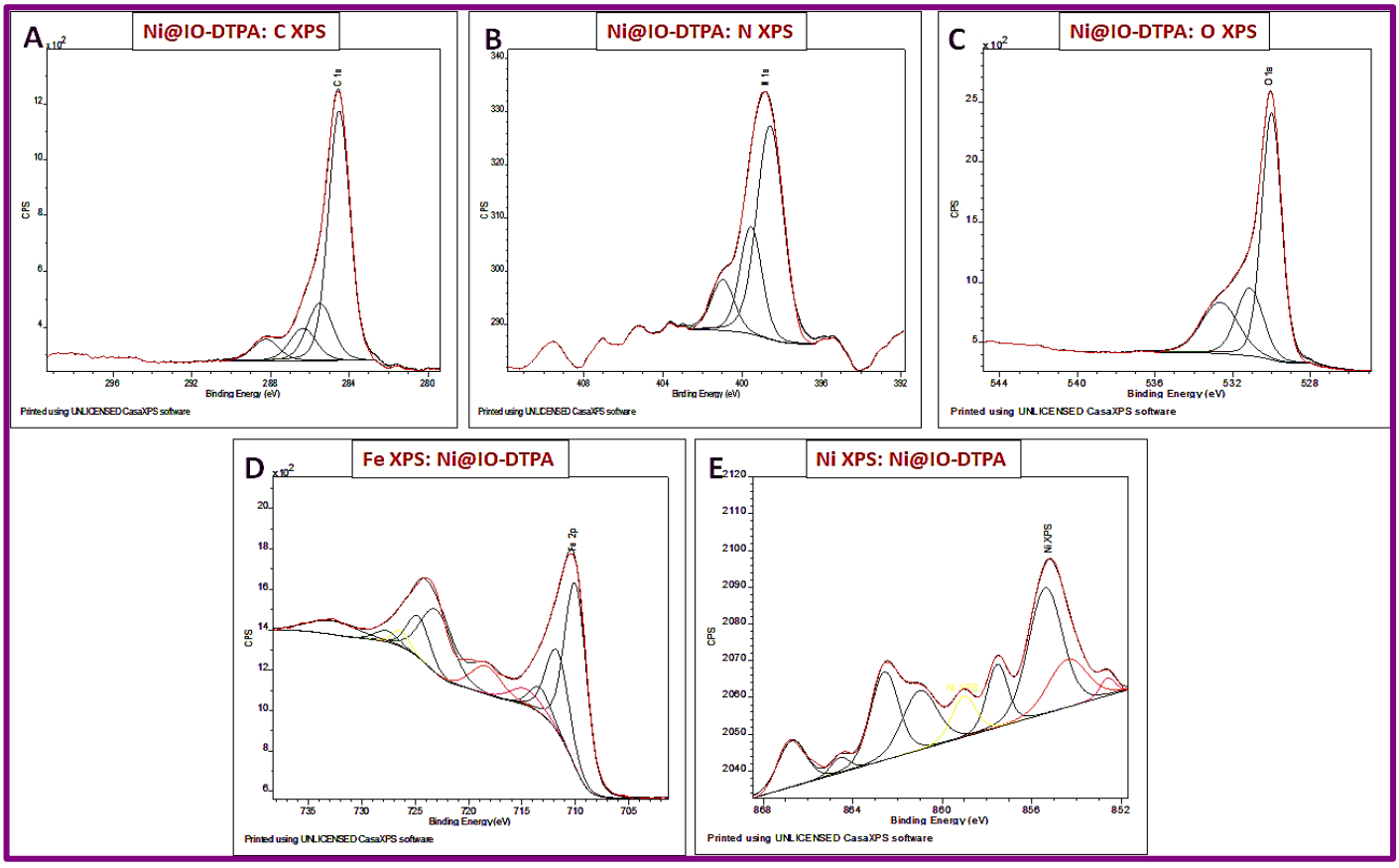

Figure 5.8*: C, N, O, Fe and Pd XPS spectra of Ni@IO-DTPA*

XPS survey spectrum of Pd@Ni@IO-DTPA confirmed the presence of C (8.55 At%), N (0.20 At%), O (62.95 At%), Fe (27.69 At%), Ni (0.25 At%) and Pd (0.36 At%). The de-convoluted XPS spectra of Pd@Ni@IO-DTPA are shown in (Figure 5.9). In Fe2p XPS spectrum (Figure 5.9D), characteristic peaks of $Fe2p_{3/2}$ and $Fe2p_{1/2}$ of Fe^{3+} were seen with satellites. Ni 2p XPS spectra (Figure 5.9E) of Pd@Ni@IO-DTPA exhibited peaks at 852.59 eV and 853.98 eV attributed to Ni2p3/2 peak of Ni(0) and NiO respectively.

In Pd 3d XPS spectrum (Figure 5.9F) the signals with binding energy 335.13 eV and 340.39 eV were assigned to Pd(0) indicating metallic character while 335.96 eV and 341.22 eV were assigned to Pd(Ni) (Zhang et al., 2015). The signal at 338.88 eV can be attributed to PdO/Pd-N and peak at 339.94 eV can be attributed to the interactions between Pd and Ni@IO-DTPA support. From deconvoluted Pd3d XPS spectra, it was found that Pd present in the nanosystem in the form of (28.95%) Pd(0), (5.87%) Pd(Ni), (45.17%) PdO.

In the O1s XPS spectrum of Pd@Ni@IO-DTPA (Figure 5.9C), the peak at binding energy of 529.93 eV was assigned to Pd-O species and Pd-O-Fe interactions while peak at binding energy of 531.22 eV was attributed to O-H of the DTPA and the peak at 533.99 eV to C=O group (Zhao et al., 2017b). Further, the assignment for N1s deconvoluted peak with binding energy 401.01 eV was attributed to C-N(C)-C (Figure 5.9B). The C 1s spectrum exhibited peaks with binding energies at 284.5, 285.7, 286.49 and 287.99 eV attributed to C-C and C-H; C-O; C–N and (–COOH) groups respectively (Figure 5.9A).

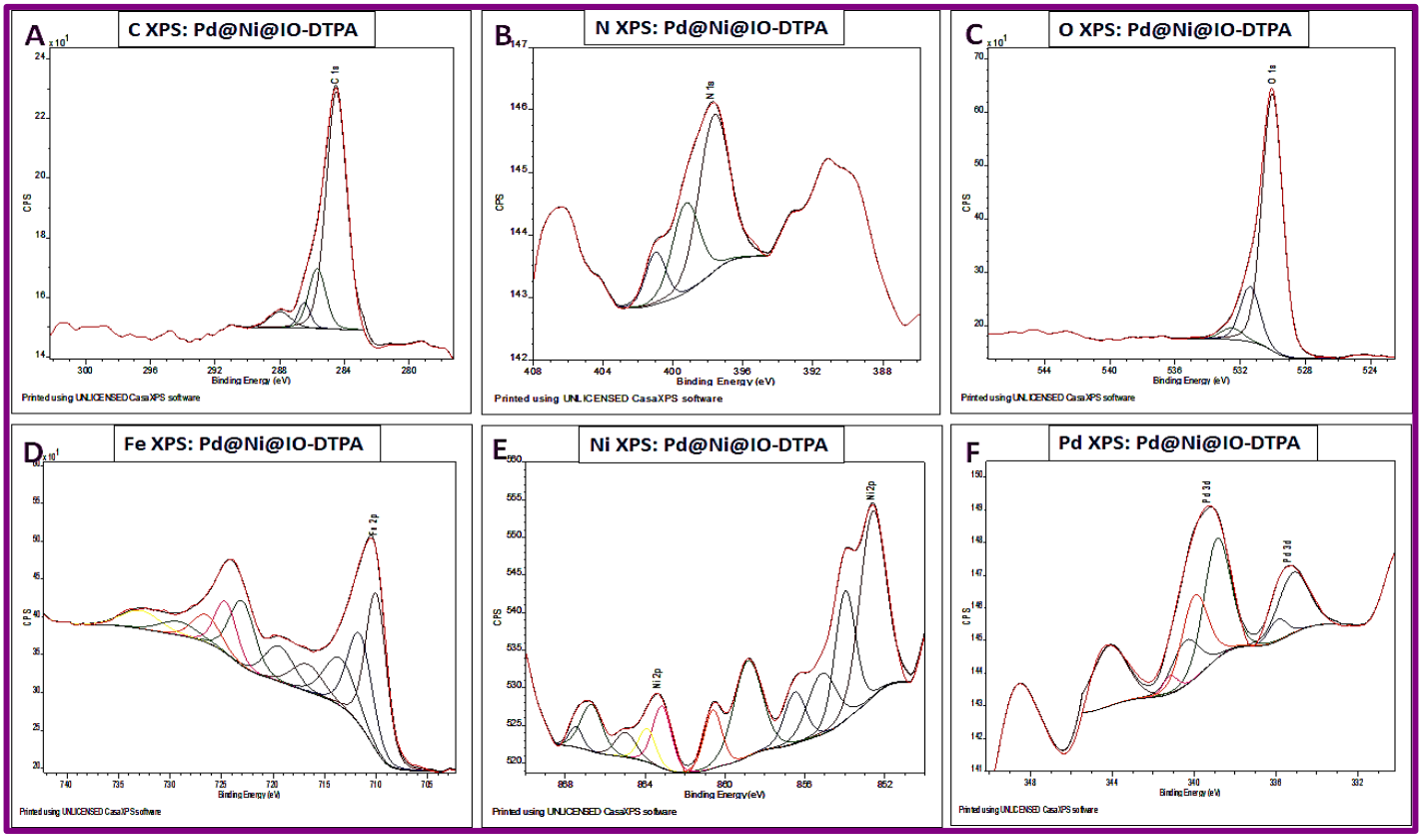

Figure 5.9*: C, N, O, Fe, Ni and Pd XPS spectra of Pd@Ni@IO-DTPA*

5.3.1.7. XANES analysis

To obtain the information of the valence state and coordination number of Nickel and Iron oxide XANES technique was used (Sciortino et al., 2011). The Fe K edge XANES spectra of Pd@IO-

DTPA showed (Figure 5.10A) that the chemical state of iron in Pd@IO-DTPA was similar to the chemical state of iron in Fe_2O_3, i.e., iron has an oxidation state of Fe^{3+} and the iron cations were surrounded by oxygen atoms in both octahedral and tetrahedral sites. (Hiroki et al., 2012).

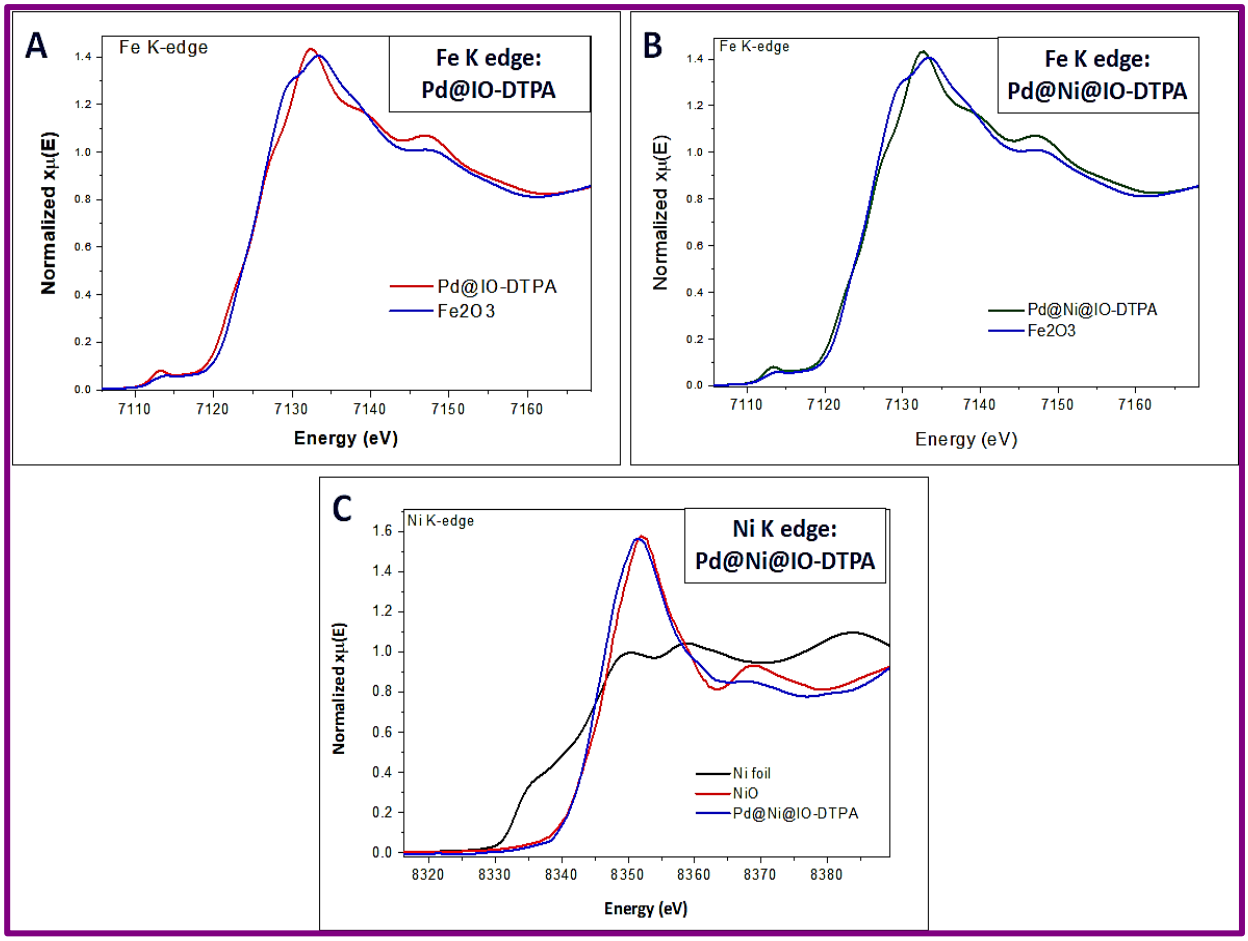

Figure 5.10: *(A) Fe k edge spectra of Pd@IO-DTPA, (B) Fe k edge spectra of Pd@Ni@IO-DTPA, and (C) Ni k edge spectra of Pd@Ni@IO-DTPA*

The Fe–K edge XANES spectra of Pd@Ni@IO-DTPA (Figure 5.10B) exhibited split pre-edge features indicating the presence of iron in 2 different states. As seen in the Fe K edge XANES Spectra (Figure 5.10B) pre- edge excitation peak at 7113 eV and main edge peak at 7132 eV are indicative of maghemite as the predominant phase. The hump at 7139.3eV suggested poorly ordered ferric compounds wherein the structure might be disturbed due to deposition of palladium/PdO. The intense white line band at 7132.5 eV can be attributed to the 1s–4p transition indicating the presence of maghemite (Fe_2O_3) (Galoisy et al., 2001). The presence of a non-stoichiometric phase of maghemite was indicated from these observations.

The Ni K edge XANES spectra (Figure 5.10C), exhibited distinct absorption characteristics at 8351.5 eV resembling NiO (Mansour & Melendres, 1994), but with lower intensity due to presence of Ni metal component. Pd@Ni@IO-DTPA exhibited particularly distinct peak at 8337 eV and 8367 eV indicating the presence of Ni and NiO in Pd@Ni@IO-DTPA.

5.3.1.8. TG-DTA analysis

Thermal stability of all the fabricated materials were studied by Thermo gravimetric analysis (TG-DTA) (Figure 5.11) under nitrogen atmosphere from 30 to 750°C with a temperature increment of 10°C/min.

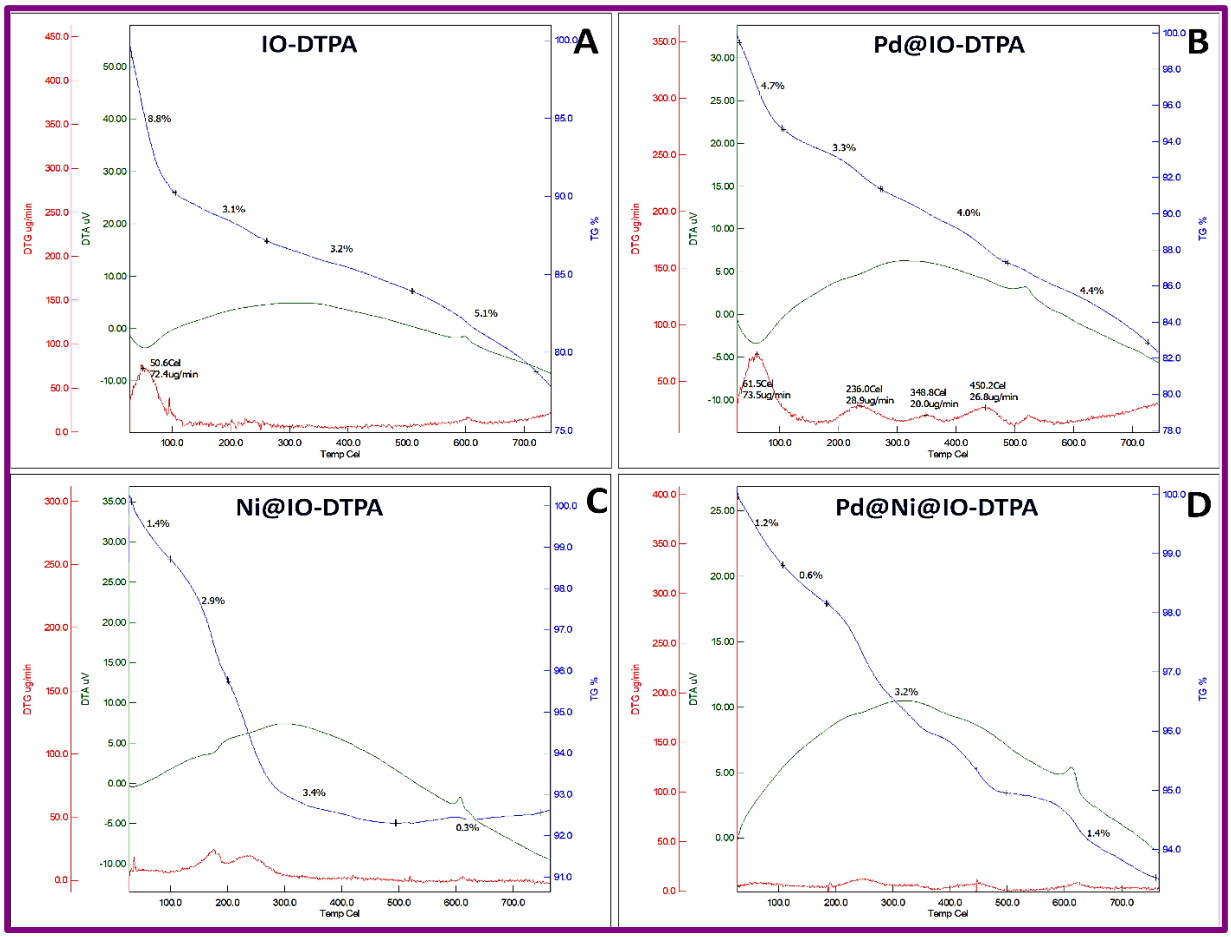

Figure 5.11: *(A) TG-DTA graph of IO-DTPA (B) TG-DTA graph of Pd@IO-DTPA and (C) Overlay VSM spectra of IO-DTPA and Pd@IO-DTPA*

Thermograms of IO-DTPA, Ni@IO-DTPA, Pd@IO-DTPA and Pd@Ni@IO-DTPA are shown in Figure 5.12(A, B, C, D) respectively. The weight losses observed upto ~100 °C was allocated to the adsorbed (surface) water (8.8% in IO-DTPA, 1.4% in Ni@IO-DTPA, 4.7% in Pd@IO-DTPA and 1.2% in Pd@Ni@IO-DTPA). The weight loss at 100-200 °C (3.1% in IO-DTPA,

2.9% in Ni@IO-DTPA, 3.3% in Pd@IO-DTPA, 0.6% in Pd@Ni@IO-DTPA) was attributed to the bound water. Further the weight loss at ~250-500 °C was attributed to the decomposition of DTPA (3.2% in IO-DTPA, 3.4% in Ni@IO-DTPA, 4.0% in Pd@IO-DTPA and 3.2% in Pd@Ni@IO-DTPA). (Aghazadeh et al., 2017). Inclusion of Ni to IO-DTPA has rendered stability as observed in thermograms of Ni@IO-DTPA and Pd@IO-DTPA

5.3.1.9. VSM analysis

The magnetization curve (Figure 5.12) for IO-DTPA, Pd@IO-DTPA, Ni@IO-DTPA and Pd@Ni@IO-DTPA confirmed the superparamagnetic behaviour of all the nanosystems from the absence of hysteresis (zero coercive force). It was also found that the magnetic response of these samples was so strong that one minute was enough to completely separate these magnetic particles by a handheld magnet.

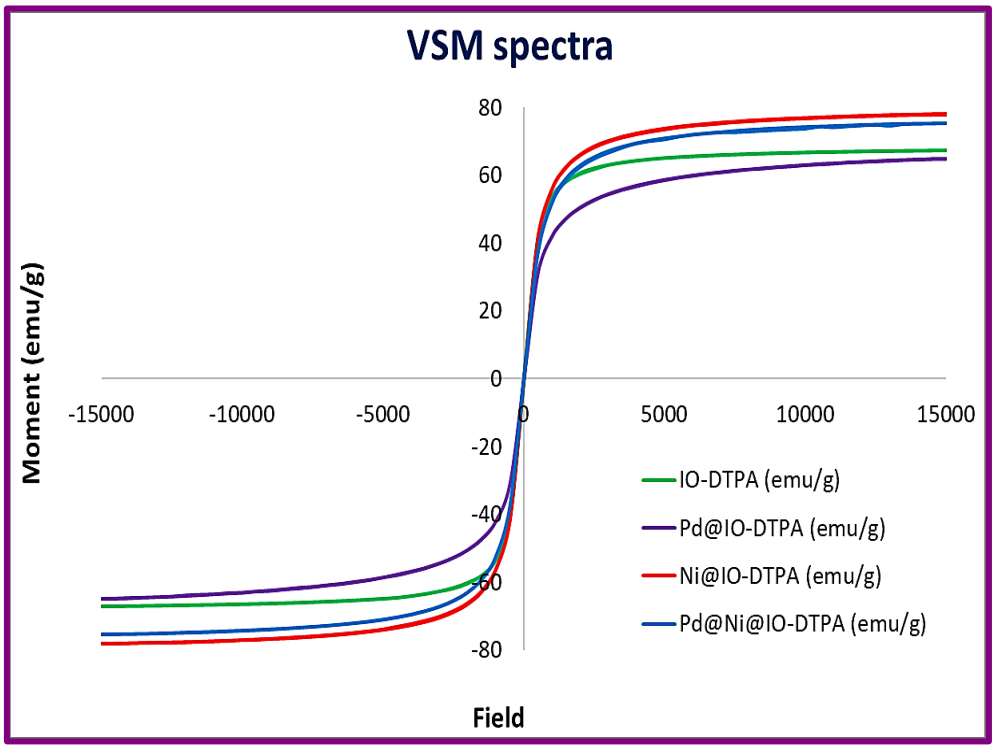

Figure 5.12: *Overlay VSM spectra of IO-DTPA, Pd@IO-DTPA, Ni@IO-DTPA and Pd@Ni@IO-DTPA*

The saturation magnetization of IO-DTPA was 67.20 emu/g which decreased to 64.948 emu/g after immobilization of nonmagnetic Pd on IO-DTPA. The saturation magnetization of Ni@IO-DTPA and Pd@Ni@IO-DTPA was observed to be 78.06 emu/g and 75.43 emu/g respectively. The increase in saturation magnetization in Ni@IO-DTPA may be attributed to changes in exchange interactions between tetrahedral and octahedral sub-lattices with the presence of Ni^{2+}

and Fe^{3+} ions in both octahedral and tetrahedral sites(Alarifi et al., 2009; Nejati & Zabihi, 2012; Pradeep et al., 2008).The decrease in Pd@Ni@IO-DTPA was due to the inclusion of nonmagnetic Pd. Furthermore, the catalyst could be easily and uniformly dispersed in solution again after the magnetic separation due to its superparamagnetism..(Lara & José G. Carriazo, 2019)

5.4. Catalytic performance of Pd@IO-DTPA and Pd@Ni@IO-DTPA

5.4.1. Catalytic reduction of p-NP in the presence of Pd@IO-DTPA and Pd@Ni@IO-DTPA

The catalytic performance of Pd@IO-DTPA and Pd@Ni@IO-DTPA catalysts was examined for reduction of p-NP to p-AP in water at room temperature (25-30℃) (Figure 5.13). An absorption peak for p-NP was observed at 319 nm. When $NaBH_4$ was added to the p-NP aqueous solution, it was found that the p-NP absorption peak shifted to a higher wavelength (403 nm), and the yellow colour of the solution changed to bright yellow as a result of the formation of 4-nitrophenolate ions (Baran & Nasrollahzadeh, 2019; Kumar et al., 2019). Upon the addition of catalyst to the reaction medium, the p-NP absorption peak at 403 nm slowly decreased and disappeared after completion of the reduction. A new absorption band was also observed at ~300 nm attributed to formation of p-Aminophenol. The bright yellow color of the solution changed to colourless at the end of the reduction.

To achieve maximum conversion, the reaction conditions were optimized. The optimum conditions for the p-NP reduction reaction for 50 mL 25 ppm p-NP were found to be, 10 mg $NaBH_4$ for Pd@IO-DTPA and 9 mg for Pd@Ni@IO-DTPA, 1 mg catalyst, and 10 min and 12 min time interval for Pd@IO-DTPA and Pd@Ni@IO-DTPA respectively (Figure 5.13(A&B)). A blank reaction in the absence of catalysts was conducted wherein no reduction was observed. Reduction performed with Ni@IO-DTPA gave 5.998% conversion while with IO-DTPA 0% conversion was obtained (Figure 5.13 (C&D)) indicating the role of Pd.

Kinetic studies were performed on the reduction of p-NP using Pd@IO-DTPA and Pd@Ni@IO-DTPA catalyst (Figure 5.13 (E&F). The pseudo-first-order kinetic model was used to calculate the rate constants (k). The pseudo-first-order was confirmed by the linear relations of $\ln(A_t/A_o)$ against reaction time where A_t and A_o were the final and initial absorbance of p-NP. The rate constant (k) determined from slope of logarithmic plot and was 0.2878 min^{-1} for Pd@IO-DTPA and 0.3218 min^{-1} for Pd@Ni@IO-DTPA.

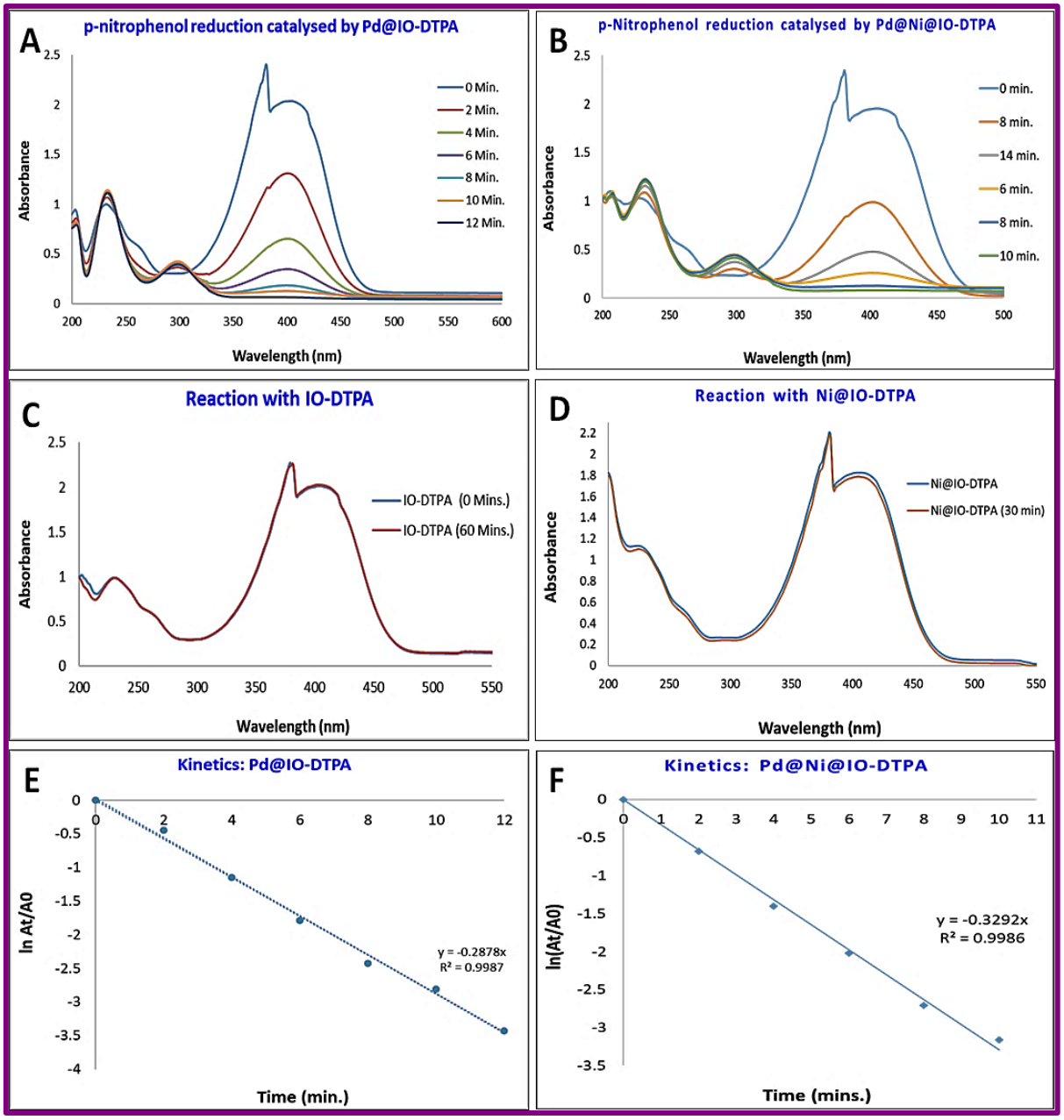

Figure 5.13: *(A, B) p-Nitrophenol reduction catalysed by Pd@IO-DTPA & Pd@Ni@IO-DTPA monitored by UV-Vis spectroscopy, (C) Reaction with IO-DTPA, (D) Reaction with Ni@IO-DTPA and (E, F) kinetic plot of ln(At/A0) vs time.* ***Reaction conditions:*** *50 ml 25 ppm p-NP, 10 mg $NaBH_4$, 1 mg catalyst*

The recyclability of Pd@IO-DTPA catalyst was also investigated for catalysing the p-NP reduction reaction. After each catalytic cycle catalyst was easily separated by magnet, dried and used for subsequent cycles. Recyclability experiments showed that Pd@IO-DTPA has high recovery efficiency and can work up to fifteen cycles for p-NP reduction. After fifteen cycles reaction time has increased to 16 min and the catalytic efficiency remained the same up to twenty-one cycles. On the other hand, Pd@Ni@IO-DTPA exhibited recovery efficiency up to

twenty-four cycles. After 24 cycles reaction time has increased to 16 mins up to 27 cycles and to 21 min up to 29 cycles.

5.4.2. Application of Pd@IO-DTPA and Pd@Ni@IO-DTPA in Suzuki−Miyaura Cross-Coupling Reactions.

To explore the catalytic activity of Pd@IO-DTPA and Pd@Ni@IO-DTPA, the cross-coupling between Iodobenzene and Phenylboronic acid was chosen as the model reaction. Yields were obtained by GC-MS analysis. Figure 5.A1 to 5.A13 (Annexures) show the representative GC MS spectra of standard biphenyl and products obtained in respective solvents.

The influence of various reaction parameters through the variation of solvents, temperature, base, time and dosages of the catalyst for coupling reaction of Iodobenzene with Phenyl boronic acid catalyzed by Pd@IO-DTPA and Pd@Ni@IO-DTPA are shown in Figure 5.14. Initially, optimizations studies were carried out in water as solvent considering green chemistry, economical and industrial aspects. Different amounts of Phenylboronic acid, ranging from 2.38 to 1.59 mmol. (i.e., 2-1 mol%) was reacted with 1.59 mmol Iodobenzene. Quantitative aryl halide conversion and formation of biphenyl was accomplished using 1.59 mmol phenylboronic acid (i.e.,1 mol%). Further increase in Phenylboronic acid led to the presence of unreacted boronic acid. Therefore 1 mol% of phenylboronic acid was used for further studies.

The performance of the reaction in different solvents was investigated (Figure 5.14A). Use of DMF, THF and toluene gave very low conversions. Neat alcohols like EtOH and i-PrOH were discovered to be ineffective solvents. However, different ratios of Isopropanol with water gave efficient catalytic conversion with both the catalysts. Pd@Ni@IO-DTPA showed good activity with ethanol and water mixture while no yield was observed with Pd@IO-DTPA. Water is clearly the ideal solvent for both the catalytic systems under study (Pd@IO-DTPA and Pd@Ni@IO-DTPA), possibly as a result of the excellent dispersion of the catalyst and the reactants as well as the high solubility of bases in water for the activation of phenylboronic acid.

Investigation of the effect of different bases on the Suzuki coupling reaction using Pd@IO-DTPA (Figure 5.14B) revealed that K_2CO_3, Na_2CO_3 were most effective in the temperature range 30°C-100°C. However, TEA dissolved Pd@IO-DTPA in the reaction system and was not magnetically separable. Other bases such as alkali metal hydroxide were effective only at 100°C (Table 5.A13, entries 6-9). On the other hand, Pd@Ni@IO-DTPA exhibited excellent activity

with K_2CO_3, Na_2CO_3, KOH and NaOH at room temperature (30 °C) (Table 5.A15, entries 16-20).

For the optimization of amount of base, different amounts of K_2CO_3 (2 to 0.1 equivalent) were used (Figure 5.14C). Complete conversion was obtained even when 0.5 equivalent of K_2CO_3 was used in the reaction. In the absence of base, the reaction did not proceed to completion even after 15 h (Table 5.A13, entry 12). Reactions with bromobenzene and chlorobenzene required higher amount of base. 0% yield were obtained at 100 °C with 0.2 to 0.5 equivalent of K_2CO_3. Therefore, 1 equivalent of K_2CO_3 was used in the further reactions. The coupling could be performed in water effectively in the temperature range (30 -100 °C) (Table 5.A13, entry 13 and table 5.A15, entries 12-16)).

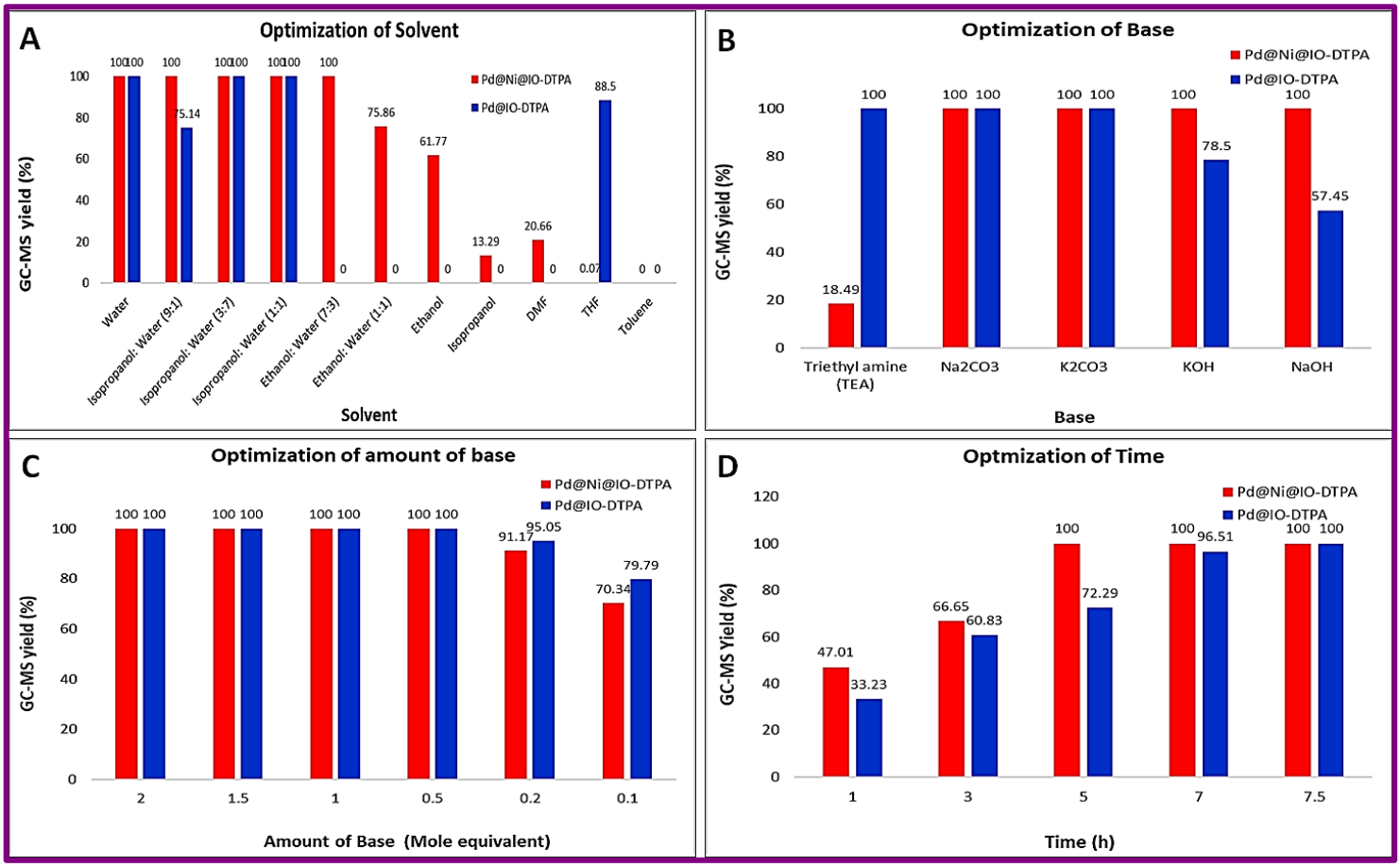

Figure 5.14: *(A)Optimizations of Solvent, (B) Optimizations of base, (C) Optimizations of base amount, and (D) Optimizations of time for reaction between Iodobenzene and Phenyboronic acid in aqueous medium.* ***Reaction condition:*** *Iodobenzene (1.59 mmol), Phenylboronic acid (1.59 mmol), catalyst dose:1 mg, solvent (10 ml water), Base-* K_2CO_3 (1 equi.), *TLC (n-hexane), GC-MS (HPLC grade chloroform)*

The optimum reaction temperature for the catalytic conversion of Iodobenzene and Phenyl boronic acid was found to be at ambient temperature. For other biphenyl derivatives the reactions could not be performed at room temperature, improvement in yield was observed with increase in temperature, therefore further reactions and studies were carried out at 100 ℃. (Table 5.1, entries 2-7)

Investigation of catalyst amount (Table 5.A13, entries 1-3 and Table 5.A15 Entries 33-35) on the reaction showed that, complete conversion was obtained with 1 mg of catalyst (0.0037 mol% Pd in Pd@IO-DTPA and 0.00704 mol% Pd in Pd@Ni@IO-DTPA) in aqueous medium with 1.59 mmol Iodobenzene and Phenylboronic acid.

While coupling of 2.0 mmol Iodobenzene and Phenylboronic acid gave 99.9% yield only at 100°C with Pd@IO-DTPA, Suzuki coupling of 2.0 mmol Iodobenzene and Phenylboronic acid with 1 mg Pd@Ni@IO-DTPA catalyst (0.0056 mol% Pd) gave 99.9% yield at 100°C as well as at room temperature. The reaction when performed in the absence of catalyst and in the presence of IO-DTPA and Ni@IO-DTPA under optimized conditions did not yield any product.

It was observed that quantitative yields with Pd@IO-DTPA were obtained with progressive increase of time from 1 to 7 h at 100 ℃ for all the substrates under study. Monitoring of the reaction time indicated that the reaction between Iodobenzene and Phenylboronic acid was completed in 7 h from the start of the reaction at 30 ℃ (Figure 5.15D). The optimized reaction conditions with Pd@IO-DTPA for the model coupling reaction in water were: Iodobenzene,1.59 mmol; Phenylboronic acid,1.59 mmol; 0.0037 mol% Pd present as Pd@IO-DTPA, K_2CO_3, 1 mmol; reaction time, 7h; water, 10mL.

On the other hand, quantitative yield was achieved with Pd@Ni@IO-DTPA catalyst in 5 h at room temperature (30 °C), Quantitative yield could be achieved even with 2 mmol Iodobenzene and Phenyl boronic acid (2 mmol) in water using K_2CO_3 (1 equi.) in the presence of Pd@Ni@IO-DTPA catalyst (0.0056 mol% Pd) at 30°C for about 5 h.

The applicability of the catalyst under study was further investigated using various aryl halides with electron-donating or electron-withdrawing groups (Table 5.1). All coupling reactions were accomplished with good to excellent yields using very low amounts of catalyst (Pd@IO-DTPA(0.0037 mol% Pd) and Pd@Ni@IO-DTPA (0.0056 mol% Pd)) under aqueous conditions. Iodobenzene and bromobenzene (Table 5.1, entries 1 & 6) had almost comparable activity, with bromobenzene taking a little longer time (8h for Pd@IO-DTPA and 6.5h for Pd@Ni@IO-DTPA) for complete reaction, while chlorobenzene was the most challenging and required a

higher temperature of 100 °C (10h for Pd@IO-DTPA and 8h for Pd@Ni@IO-DTPA). (Table 5.1, entry 7)

It was noticed that with electron-rich halides the yields were low as compared to electron-deficient substrates, though the oxidative addition was slower for aryl halides with electron-donating groups (Barder et al., 2005) The electron withdrawing group may have facilitated the rate limiting oxidative addition step. Therefore, the aryl iodide with electron deficient group (-CHO) gave more yield as compared to electron rich group (-CH_3). On the other hand, ortho-substituted Iodobenzene with electron donating group (-CH_3) gave slightly lower yield as compared to para substituted Iodobenzene (Table 5.1, entries 2&3).

Thin layer chromatography (TLC) technique was used to monitor the progress of the reaction. The spots for the starting material on TLC vanished after a definite time, indicating that the reactant had completely converted to the product. During workup, an external hand held magnet was used to separate the catalyst from the flask. In order to isolate the product from the aqueous medium, the reaction mass was subjected to solvent extraction with ethyl acetate(Islam et al., 2011). This was followed by spectroscopic characterizations of the product using ^{1}H NMR, and GC-MS (Supporting Information). The Pd catalysts were washed several times with ethyl acetate and water and dried in oven at 100 °C. More than 99% of the catalyst could usually be recovered (based on the weight).

Table 5.1 Suzuki Coupling Reaction catalysed by Pd@IO-DTPA and Pd@Ni@IO-DTPA at 30 °C, 60 °C and 100 °C

Reaction condition for Pd@IO-DTPA: *Arylhalide (1.59 mmol), phenylboronic acid (1.59 mmol), solvent (10 ml), catalyst (Pd@IO-DTPA) (1 mg), base (1 equiv.), Temperature: 30°C, 60°C and 100 °C, TLC (n-hexane), GC-MS (HPLC grade chloroform), Yields were obtained by GC-MS analysis*

Reaction condition for Pd@Ni@IO-DTPA: *Arylhalide (2 mmol), phenylboronic acid (2 mmol), solvent (10 ml), catalyst (Pd@Ni@IO-DTPA) (1 mg), base (1 equiv.), Temperature: 30°C, 60°C and 100 °C, TLC (n-hexane), GC-MS (HPLC grade chloroform), Yields were obtained by GC-MS analysis*

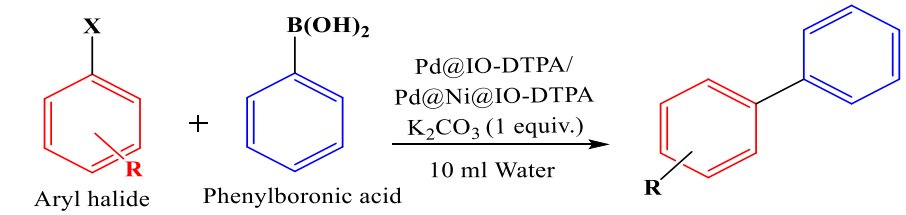

Aryl halide
X= I, Br
R= H, CH_3, CHO

Phenylboronic acid

R= H, CH_3, CHO

Sr. No.	X	R	At 30°C *Pd@IO-DTPA/ Pd@Ni@IO-DTPA*		At 60°C *Pd@IO-DTPA/ Pd@Ni@IO-DTPA*		At 100°C *Pd@IO-DTPA/ Pd@Ni@IO-DTPA*		
			Time	GC-MS Yield (%)	Time	GC-MS Yield (%)	Time	GC-MS Yield (%)	Isolated Yield (%)
1	I	H	8 h	100	7 h	100	7 h.	100	99.99
			6h	100	5h	100	5 h.	100	99.99
2	I	p-CH_3	13 h	54.42	12 h	73.8	12 h	92.3	92.0
			11 h	59.13	10h	67.99	10 h	95.33	94.98
3	I	o-CH_3	15 h	trace	14 h	72	13 h	84.3	81.78
			16 h	51.19	14h	58.48	11 h	92.03	91.76
4	I	o-CHO	20 h	70.9	18 h	92.8	17 h	100	99.9
			17 h	89.74	15h	94.95	14 h	100	99.84
5	I	p-CHO	15 h.	92.2	14 h	96.3	12 h	100	99.9
			11h	91.83	11h	96.54	10 h	100	99.96
6	Br	H	12 h	34.80	10 h	97.14	8 h	100	99.9
			10h	71.78	8h	88.35	6.5 h	100	99.99
7	Cl	H	15 h	6.1	12 h	24.8	10 h	75.6	75.1
			12h	15.34	11h	39.20	8 h	100	99.99

Table 5.1: *Suzuki cross-coupling of several aryl halides with arylboronic acids that were investigated using nanoparticle-supported Pd catalysts.*

To study the heterogeneous nature of the catalysts, a hot filtration test was carried out under optimized conditions. The catalyst was separated after two hours and the reaction was then carried out for an additional ten hours. Products were isolated and analysed using GC-MS (Figure 5.A38&39), There was no increase in yield of the desired product after magnetic removal of the catalyst, revealing the heterogeneous nature of the catalyst under study.

5.4.3. Recyclability of catalyst (Pd@IO-DTPA and Pd@Ni@IO-DTPA**)**

The potential recyclability of the catalyst (Pd@IO-DTPA and Pd@Ni@IO-DTPA) was explored in the model cross-coupling of Iodobenzene and phenylboronic acid. The catalyst was magnetically separated, washed with water and subsequently with acetone, dried in oven at 100 ℃ and employed for another round of reactions. Recycled catalysts were characterized by IR, VSM, SEM, TGA and XPS techniques and Pd leaching was tested by ICP-MS.

The reusability of the catalysts was examined by using a reaction between Iodobenzene and Phenylboronic acid. Pd@Ni@IO-DTPA showed an isolation yield of 100% up to 13 cycles and no discernible loss of catalytic activity as well as no significant amount of Pd leaching was found by ICP-MS (Figure 5.18F), while Pd@IO-DTPA showed recyclability upto 6 cycles with no significant amount of Pd leaching (Figure 5.16A&E)

SEM images of recycled Pd@IO-DTPA catalyst showed an aggregation of Pd (Figure 5.15). There was no change in Fe K edge spectra of catalyst suggesting the stability of DTPA capped IO nanostructure under the reaction conditions.

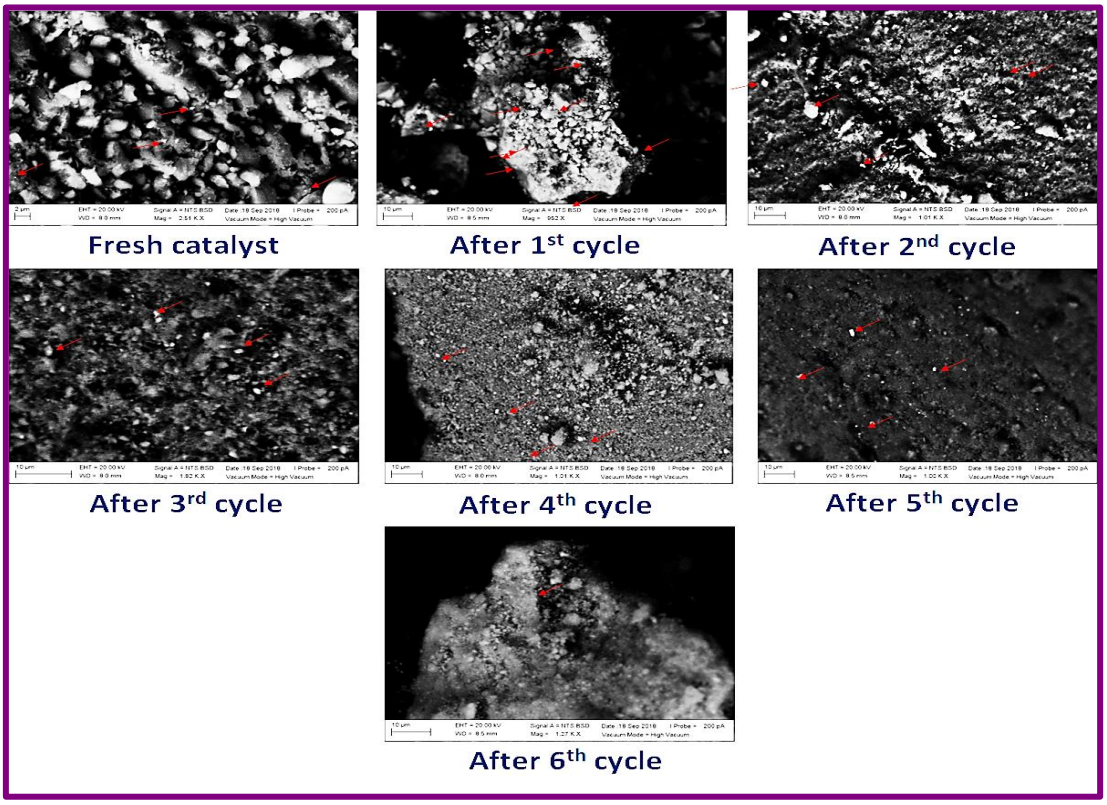

Figure 5.15: *SEM images of Recycled catalyst (Pd@IO-DTPA)*

According to the VSM spectra of recycled Pd@IO-DTPA catalyst, the superparamagnetic property (Figure 5.16C) of the catalyst was retained even after the 6th cycle. The catalyst could

be easily separated by a magnet and could be uniformly dispersed in reaction system again after the magnetic separation. The magnetic response of the recycled catalyst was decreased from 64.948 to 31.29 emu/g. The weight loss observed at ~30-100 °C during TGA-DTA analysis recycled Pd@IO-DTPA catalyst (Figure 5.16D), attributed to the adsorbed water increased from 4.7% in fresh Pd@IO-DTPA as compared to 11.4% in recycled catalyst (after 6th cycle). However, the weight loss of 4.0% in fresh Pd@IO-DTPA at ~250-500 °C associated to decomposition of the grafted DTPA did not show significant change in recycled catalyst (is almost same (3.9%)).

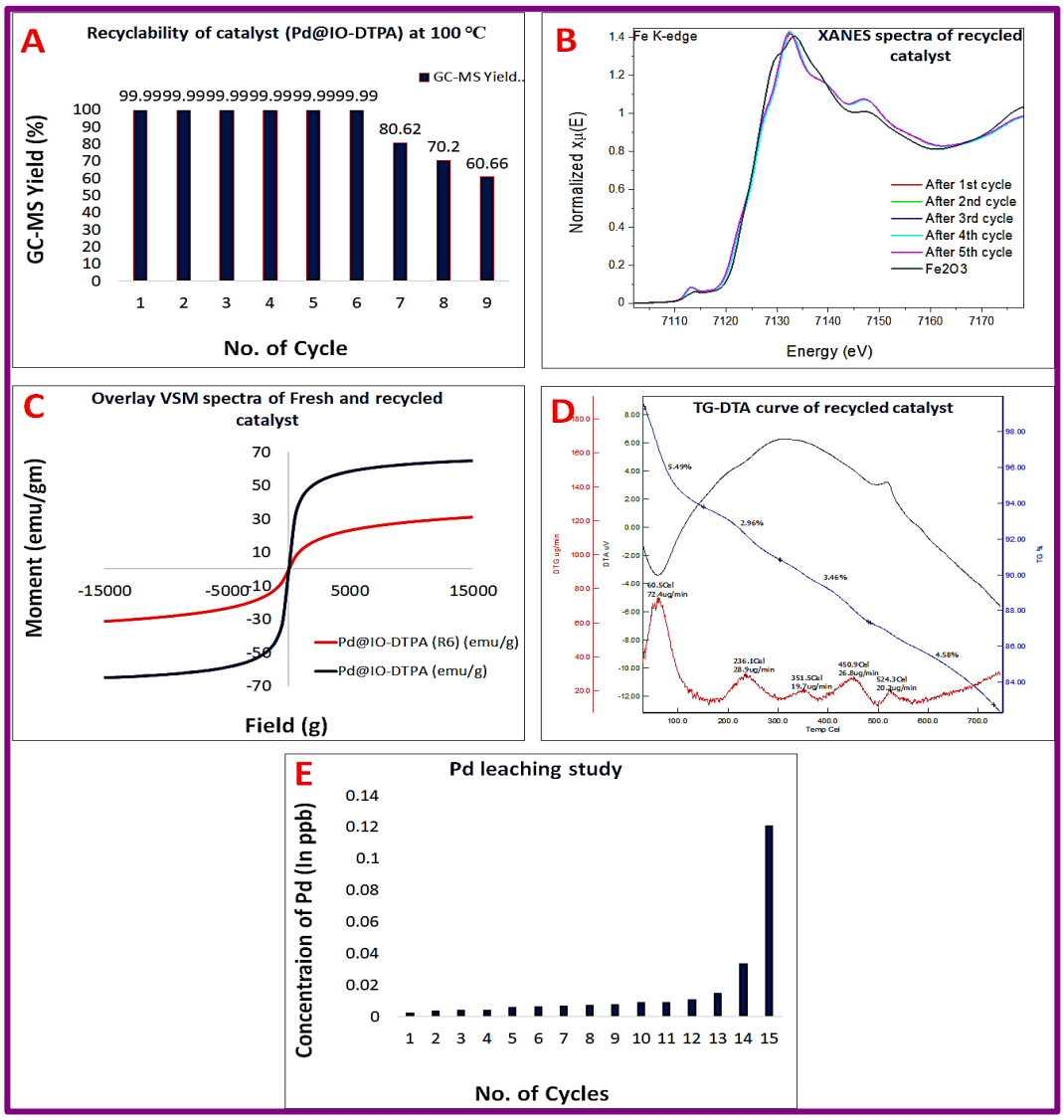

Figure 5.16: *(A) Recyclability of the catalyst, (B) overlay Fe K-edge XANES spectra of fresh and recycled catalyst, (C) Overlay VSM spectra of Fresh and recycle catalyst (After 6th cycle), (D) TG-DTA data of recycled catalyst (After 6th cycle), (E) Pd leaching study by ICP-MS*

The XPS spectra of recycled Pd@IO-DTPA catalyst (after the 6th reaction cycle) (Figure 5.17) exhibited the same characteristic peaks as observed in the fresh catalyst. The Fe Content was decreased by 2%. There was 0.5% increase in nitrogen, 6% increase in O and 7.5% increase in C content suggesting poisoning of the catalyst with reactants. Detailed XPS assignment of the fresh and recycled catalyst are provided in Tables 5.A1-5.A2

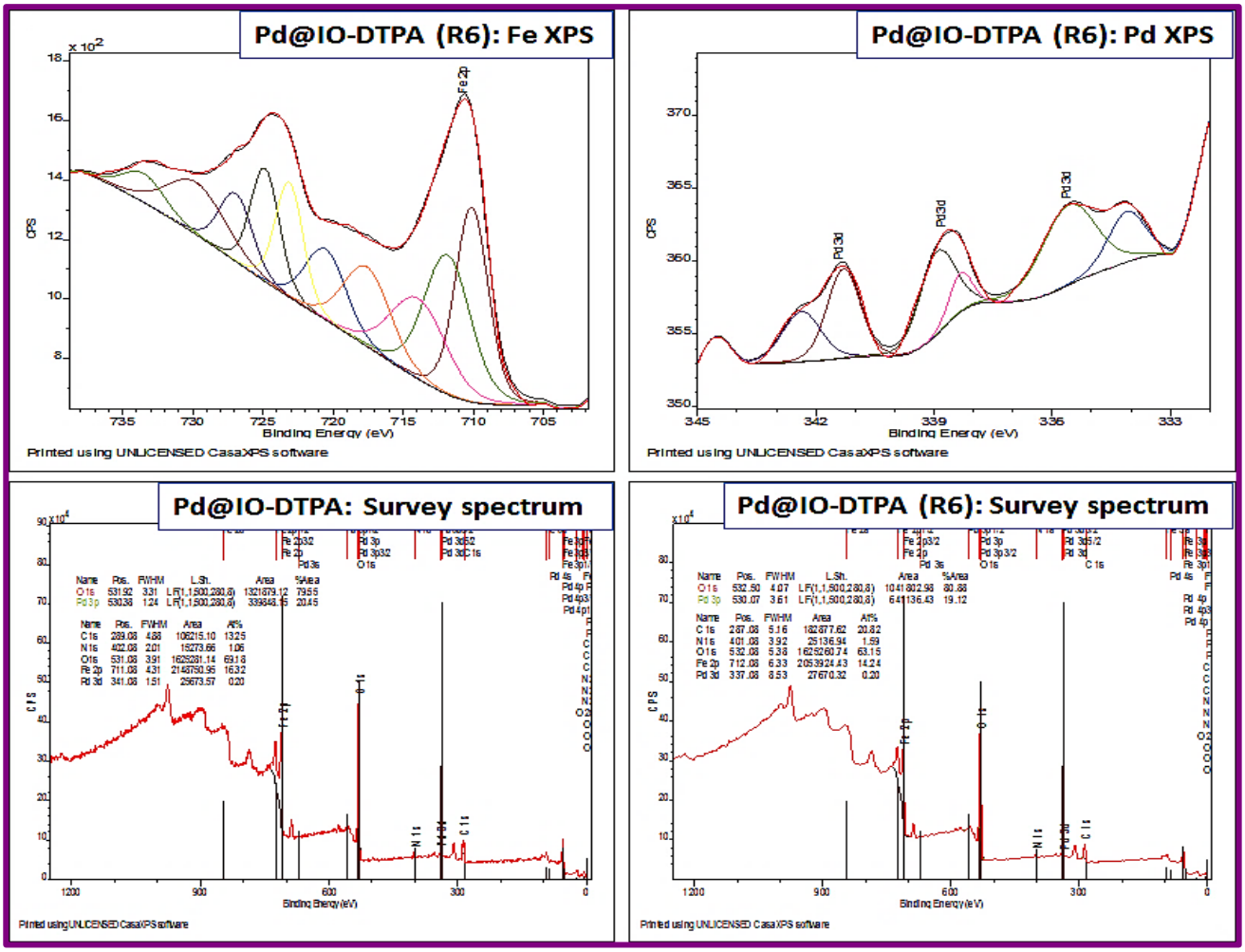

Figure 5.17: *Fe, Pd XPS Spectra of Recycled catalyst, survey spectrum of fresh and recycled catalyst (after 6th cycle)*

SEM images of recycled Pd@Ni@IO-DTPA catalyst showed aggregation of Pd (Figure 5.18 (A-C)). A 4% decrease in yield was observed during the 14th cycle (Figure 5.A36) and leaching was also confirmed from ICP-MS data after 14th cycle (Figure 5.18F). Recycled catalyst was also investigated by VSM technique. The superparamagnetic response of the recycled catalyst was decreased from 75.43 to 39.98 emu/g, the catalyst could be still be easily separated by a magnet and could be uniformly dispersed in reaction system again after the magnetic separation due to the retainment of its super paramagnetic property (Figure 5.18E) even after the 13th cycle.

Recycled catalyst was further characterized by TG-DTA ((Figure 5.18D). Total weight loss of 26.3% in fresh catalyst while in the case of recycled catalyst i.e, 19.51% at ~30-750 °C.

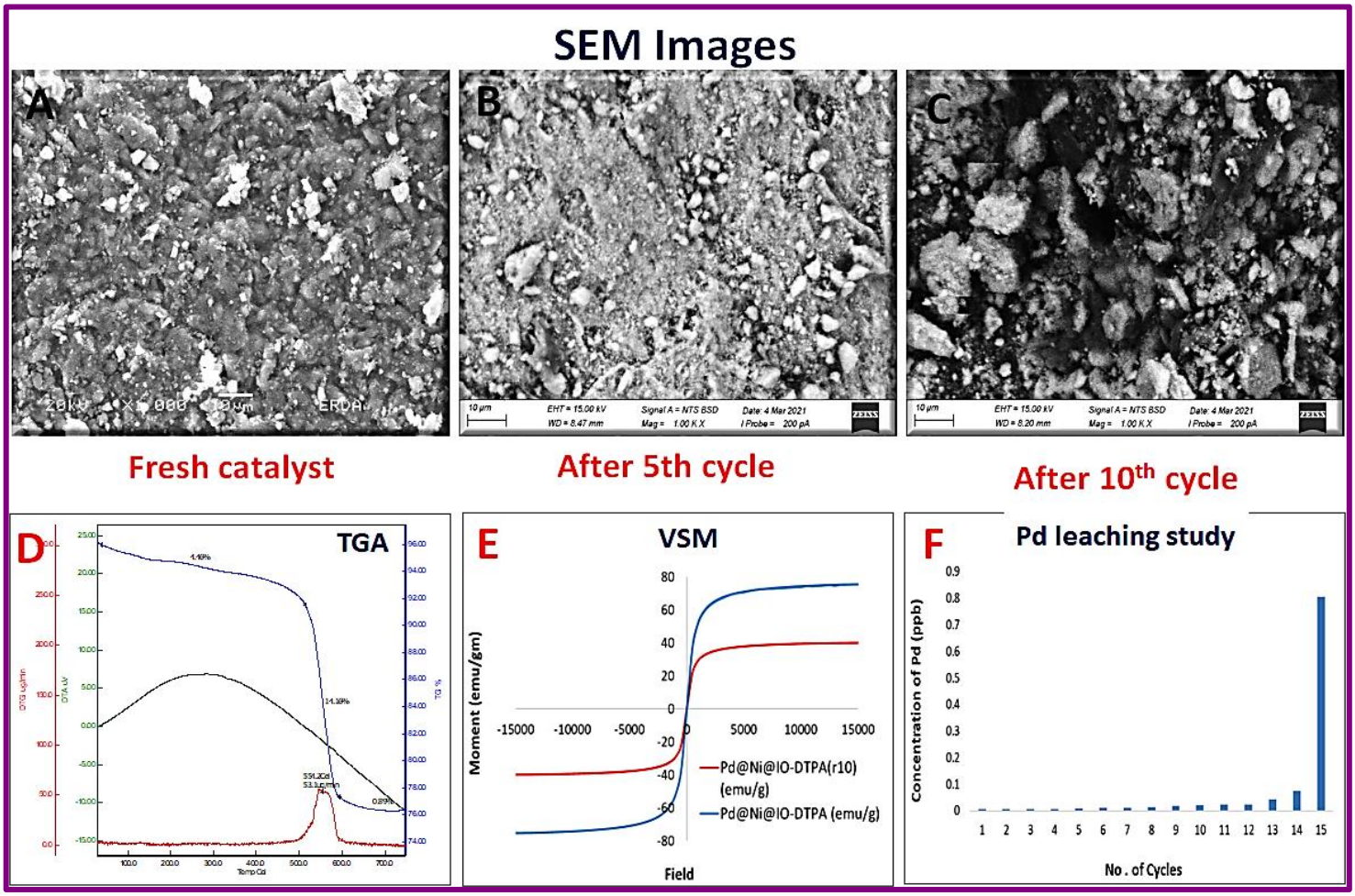

Figure 5.18: (*A-C) SEM images of Recycled catalyst, (D) TGA of recycled catalyst, (E) VSM spectra of fresh and recycled catalyst (F) Pd leaching study by ICP-MS*

The recycled Pd@Ni@IO-DTPA catalyst (after the 13th run) was further investigated by XPS. The Fe, Ni, Pd, O, N, C XPS (Figure 5.19)) exhibited the same characteristic peaks as observed in the fresh catalyst. There was 46% decrease in Fe content. There was 0.5% decrease in N, 26% increase in O and 22% increase in C content suggesting poisoning of the catalyst with reactants. Fresh catalyst contains 0.38 at% Pd (72.62% Pd(0), 27.37% Pd^2 from deconvoluted spectra). Pd XPS spectra of recycled catalyst confirmed that Pd content was decreased to 0.28 at% and from deconvoluted spectra it was found that 28.86% Pd(0), 45.6% Pd(2+) and 25.53% PdO were present in the sample. XPS Survey spectrum also revealed tha Nickel content was decreased to 0.21 at% (36.96% Ni(0), 33.98% Ni^{2+}). Detailed XPS assignment of the fresh and recycled catalyst are given in Tables S5.6-S5.11.

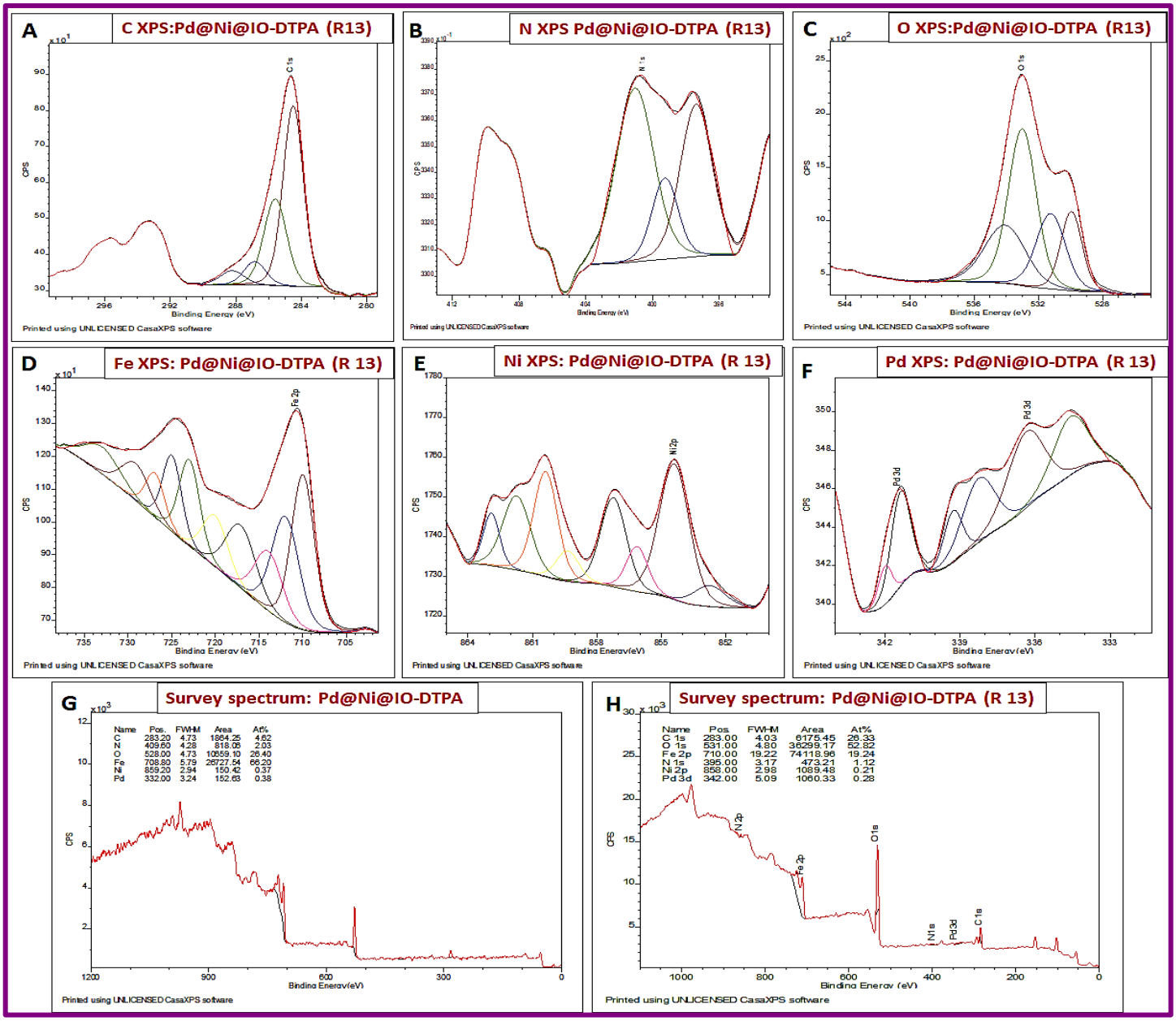

Figure 5.19*:(A-C) C, N, O XPS spectra of recycles catalyst. (D) Fe XPS spectra of Recycled catalyst, (E) Ni XPS spectra of Recycled catalyst, (F) Pd XPS spectra of Recycled catalyst (G) XPS Survey spectrum of Fresh catalyst (H) XPS Survey spectrum of Recycled catalyst*

5.5. Conclusions

In conclusion, a novel catalytic system comprising Pd nanoparticles supported on DTPA stabilized Iron oxide nanoparticles (Pd@IO-DTPA) and Ni doped DTPA stabilized Iron oxide nanoparticles (Pd@Ni@IO-DTPA) was fabricated at room temperature in aqueous medium without using reducing agent.

Characterization studies of Pd@IO-DTPA revealed that Pd and PdO were dispersed on IO-DTPA and that of Pd@Ni@IO-DTPA confirmed the presence of well dispersed Pd, PdO, Ni,

NiO on support. Both the catalysts showed excellent catalytic activity for Suzuki coupling reaction and p-Nitrophenol reduction with very high recoverability.

Superparamagnetic property of IO-DTPA (67.20 emu/g) has increased after loading of Nickel on IO-DTPA (Ni@IO-DTPA) (78.06 g/emu). The separation of Pd@Ni@IO-DTPA (75.43 emu/g) was faster and easier than the Pd@IO-DTPA (64.948 emu/g) due to their magnetic prperties. Therefore, recyclability of the catalyst had increased. Pd@Ni@IO-DTPA can be reused for 29 times for the reduction of p-NP and 13 times in Suzuki coupling reaction. While Pd@IO-DTPA can be reused upto 21 times in p-NP reduction and 6 times for Suzuki coupling reaction.

Furthermore, combining non noble metal Ni with noble metal Pd can affect the electronic structure of Pd by the electron transfer which can disturb the highest occupied and lowest unoccupied molecular orbitals of Pd and this further reduces the activation energies. So, fabrication of Pd@Ni@IO-DTPA catalyst is a potential strategy to enhance the catalytic activity with high TON and high reusability.

5.6. References

Aghazadeh, M., Karimzadeh, I., & Ganjali, M. R. (2017). Ethylenediaminetetraacetic acid capped superparamagnetic iron oxide (Fe3O4) nanoparticles : A novel preparation method and characterization. *Journal of Magnetism and Magnetic Materials*, *439*, 312–319. https://doi.org/10.1016/j.jmmm.2017.05.042

Ahmad, T., Bae, H., Iqbal, Y., Rhee, I., & Hong, S. (2015). Chitosan-coated nickel-ferrite nanoparticles as contrast agents in magnetic resonance imaging. *Journal of Magnetism and Magnetic Materials*, *381*, 151–157. https://doi.org/10.1016/j.jmmm.2014.12.077

Alarifi, A., Deraz, N. M., & Shaban, S. (2009). Structural, morphological and magnetic properties of NiFe2O4 nano-particles. *Journal of Alloys and Compounds*, *486*, 501–506. https://doi.org/10.1016/j.jallcom.2009.06.192

Amirmahani, N., Mahmoodi, N. O., Malakootian, M., Pardakhty, A., & Seyedi, N. (2021). Introduction of PdCl2 supported on tartaric acid modified magnetite nanoparticles (Fe3O4@TA-Pd) as a novel catalytic system in Suzuki–Miyaura coupling reaction. *Materials Chemistry and Physics*, *267*, 124698. https://doi.org/10.1016/j.matchemphys.2021.124698

Arumugam, S., Toku, Y., & Ju, Y. (2020). Fabrication of γ -Fe2O3 Nanowires from Abundant and Low-cost Fe Plate for Highly Effective Electrocatalytic Water Splitting. *Scientific Reports*, *10*(1), 5407. https://doi.org/10.1038/s41598-020-62259-6

Azizi, K., Ghonchepour, E., Karimi, M., & Heydari, A. (2015). Encapsulation of Pd(II) into superparamagnetic nanoparticles grafted with EDTA and their catalytic activity towards reduction of nitroarenes and Suzuki – Miyaura coupling. *Appl. Organometal. Chem.*,

29(4), 187–194. https://doi.org/10.1002/aoc.3258

Baran, T., & Nasrollahzadeh, M. (2019). Facile synthesis of palladium nanoparticles immobilized on magnetic biodegradable microcapsules used as effective and recyclable catalyst in Suzuki-Miyaura reaction and p -nitrophenol reduction. *Carbohydrate Polymers*, *222*, 115029. https://doi.org/10.1016/j.carbpol.2019.115029

Barder, T. E., Walker, S. D., Martinelli, J. R., & Buchwald, S. L. (2005). Catalysts for Suzuki - Miyaura Coupling Processes : Scope and Studies of the Effect of Ligand Structure. *J. Am. Chem. Soc.*, *127*(13), 4685–4696. https://doi.org/10.1021/ja042491j

Dehghani, M., Tadjarodi, A., & Chamani, S. (2019). Synthesis and Characterization of Magnetic Zeolite Y−Palladium−Nickel Ferrite by Ultrasonic Irradiation and Investigating Its Catalytic Activity in Suzuki − Miyaura Cross-Coupling Reactions [Research-article]. *ACS Omega*, *4*, 10640–10648. https://doi.org/10.1021/acsomega.9b00666

Esmaeilpour, M., Zahmatkesh, S., Fahimi, N., & Nosratabadi, M. (2018). Palladium nanoparticles immobilized on EDTA - modified Fe3O4@SiO2 nanospheres as an efficient and magnetically separable catalyst for Suzuki and Sonogashira cross - coupling reactions. *Appl. Organometal. Chem.*, *32*(4), 4302. https://doi.org/10.1002/aoc.4302

Fihri, A., Bouhrara, M., Nekoueishahraki, B., Basset, J.-M., & Polshettiwar, V. (2011). Nanocatalysts for Suzuki cross-coupling reactions. *Chem. Soc. Rev.*, *40*(10), 5181–5203. https://doi.org/10.1039/c1cs15079k

Fondell, M., Gorgoi, M., Boman, M., & Lindblad, A. (2018). Surface modification of iron oxides by ion bombardment – Comparing depth profiling by HAXPES and Ar ion sputtering. *Journal of Electron Spectroscopy and Related Phenomena*, *224*, 23–26. https://doi.org/10.1016/j.elspec.2017.09.008

Ganji, S., Bukya, P., Vakati, V., Rao, K. S. R., & Burri, D. R. (2013). Highly efficient and expeditious PdO/SBA-15 catalysts for allylic oxidation of cyclohexene to cyclohexenone. *Catalysis Science & Technology*, *3*(409–414). https://doi.org/10.1039/c2cy20627g

Ghanbari, N., Hoseini, S. J., & Bahrami, M. (2017). Ultrasonic assisted synthesis of palladium-nickel/iron oxide core-shell nanoalloys as effective catalyst for Suzuki-Miyaura and p -nitrophenol reduction reactions. *Ultrasonics - Sonochemistry*, *39*, 467–477. https://doi.org/10.1016/j.ultsonch.2017.05.015

Guin, D., Baruwati, B., & Manorama, S. V. (2007). Pd on Amine-Terminated Ferrite Nanoparticles : A Complete Magnetically Recoverable Facile Catalyst for Hydrogenation Reactions. *Organic Letters*, *9*(7), 1419–1421. https://doi.org/10.1021/ol070290p

Hiroki, O., Akira, Y., Kei, M., Maki, O., Takashi, T., & Shinichi, K. (2012). Local structure of magnetite and maghemite and chemical shift in Fe K-edge XANES. *Journal of Mineralogical and Petrological Sciences*, *107*, 127–132. https://doi.org/10.2465/jmps.110624

Islam, R. U., Witcomb, M. J., Van Der Lingen, E., Scurrell, M. S., Van Otterlo, W., & Mallick, K. (2011). In-situ synthesis of a palladium-polyaniline hybrid catalyst for a Suzuki coupling reaction. *Journal of Organometallic Chemistry*, *696*(10), 2206–2210. https://doi.org/10.1016/j.jorganchem.2010.11.039

Jinhui Tong, Lingdi Su, Lili Bo, Xiaodong Cai, Qianping Zhang, & Qizhao Wang. (2016). Mesoporous palladium-copper ferrites as highly efficient and. *Materials Research Bulletin*, *73*, 240–246. https://doi.org/10.1016/j.materresbull.2015.09.013

Khazaei, A., Khazaei, M., & Nasrollahzadeh, M. (2017). Nano-Fe3O4@SiO2 supported Pd (0) as a magnetically recoverable nanocatalyst for Suzuki coupling reaction in the presence of waste eggshell as low-cost natural base. *Tetrahedron*, *73*(38), 5624–5633. https://doi.org/10.1016/j.tet.2017.05.054

Kumar, A., Belwal, M., Raman, R., Mohan, V., & Vishwanathan, V. (2019). Heterogeneous catalytic reduction of anthropogenic pollutant , 4-nitrophenol by Au / AC nanocatalysts. *Materials Science for Energy Technologies*, *2*, 526–531. https://doi.org/10.1016/j.mset.2019.05.007

Kumaresan, R., Sabharwal, K. N., Srinivasan, T. G., Rao, P. R. V., & Dhekane, G. (2008). Studies on the Sorption of Palladium using Cross - Linked Poly (4 - Vinylpyridine - Divinylbenzene) Resins in Nitric Acid Medium. *Solvent Extraction and Ion Exchange*, *26*, 643–671. https://doi.org/10.1080/07366290802301465

Lara, V. N., & José G. Carriazo. (2019). Fe3O4-TiO2 and Fe3O4-SiO2 Core-shell Powders Synthesized from Industrially Processed Magnetite (Fe3O4) Microparticles. *Materials Research*, *22*(3), 20180660. https://doi.org/10.1590/1980-5373-mr-2018-0660

Li, L., Li, Y., Yan, J., Cao, H., Dongyun Shao, & Bao, J. J. (2019). A magnetically recyclable superparamagnetic silica supported Pt nanocatalyst through a multi- carboxyl linker: synthesis, characterization, and applications in alkene hydrosilylation. *RSC Adv.*, *9*, 12696–12709. https://doi.org/10.1039/c9ra00375d

Ma, Z., Li, F., Jia, A., Zhang, X., & Wang, Y. (2021). Facile synthesis of EDTA grafted 3D spherical-chain porous silica with high capacity for rapidly selective adsorption of Cu(II) from aqueous solutions. *Journal of Porous Materials*, *28*, 299–310. https://doi.org/10.1007/s10934-020-00991-0

Malkar, V. V, Mukherjee, T., & Kapoor, S. (2014). Synthesis of silver nanoparticles in aqueous aminopolycarboxylic acid solutions via γ -irradiation and hydrogen reduction. *Materials Science & Engineering C*, *44*, 87–91. https://doi.org/10.1016/j.msec.2014.08.002

Mansour, A., & Melendres, C. (1994). X-ray absorption spectra and structure of some nickel oxides (hydroxides). *Electrochemical Society Extended Abstracts Volume*, *94*(2).

Nejati, K., & Zabihi, R. (2012). Preparation and magnetic properties of nano size nickel ferrite particles using hydrothermal method. *Chemistry Central Journal*, *6*(23), 1–6. https://doi.org/10.1186/1752-153X-6-23

Peuckert, M. (1985). XPS study on surface and bulk palladium oxide, its thermal stability, and a comparison with other noble metal oxides. *Journal of Physical Chemistry*, *89*, 2481–2486. https://doi.org/10.1021/j100258a012

Pradeep, A., Priyadharsini, P., & Chandrasekaran, G. (2008). Production of single phase nano size NiFe2O4 particles using sol – gel auto combustion route by optimizing the preparation conditions. *Materials Chemistry and Physics*, *112*, 572–576.

https://doi.org/10.1016/j.matchemphys.2008.05.090

Predoi, D., Andronescu, E., Radu, M., Munteanu, M. C., & A. DINISCHIOTU. (2010). SYNTHESIS AND CHARACTERIZATION OF BIO-COMPATIBLE MAGHEMITE NANOPARTICLES. *Digest Journal of Nanomaterials and Biostructures*, *5*(3), 779–786.

Qi, B., Di, L., & Zhang, X. (2014). Dry plasma reduction to prepare a high performance Pd/C catalyst at atmospheric pressure for CO oxidation †. *Journal of Materials Chemistry A*, *2*, 11885–11890. https://doi.org/10.1039/c4ta02155j

Rahal, H. T., Awad, R., & Bakeer, D. E. (2017). Synthesis , Characterization , and Magnetic Properties of Pure and EDTA-Capped NiO Nanosized Particles. *Journal of Nanomaterials*, *2017*. https://doi.org/10.1155/2017/7460323

Ravi, S., Zhang, S., Lee, Y. R., Kang, K. K., Kim, J. M., Ahn, J. W., & Ahn, W. S. (2018). EDTA-functionalized KCC-1 and KIT-6 mesoporous silicas for Nd3+ ion recovery from aqueous solutions. *Journal of Industrial and Engineering Chemistry*, *67*, 210–218. https://doi.org/10.1016/j.jiec.2018.06.031

Richardson, J. T., Scates, R., & Twigg, M. V. (2003). X-ray diffraction study of nickel oxide reduction by hydrogen. *Applied Catalysis A : General*, *246*, 137–150. https://doi.org/10.1016/S0926-860X(02)00669-5

Silva, L., Carvalho, R., Freitas, M. P., Tormena, C. F., & Melo, W. C. (2007). Spectrometric and theoretical investigation of the structures of Cu and Pb / DTPA complexes. *Structural Chemistry*, *18*(5), 605–609. https://doi.org/10.1007/s11224-007-9192-8

Silva, L., Carvalho, R., Freitas, M. P., Tormena, C. F., & Walcl´ee C. Melo. (2007). Structural determination of Zn and Cd – DTPA complexes : MS , infrared , 13 C NMR and theoretical investigation. *Spectrochimica Acta Part A*, *68*, 1197–1200. https://doi.org/10.1016/j.saa.2007.01.020

Singh, A. S., Shelkar, R. S., & Nagarkar, J. M. (2015). Palladium(II) on functionalized NiFe2O4: An efficient and recyclable phosphine-free heterogeneous catalyst for suzuki coupling reaction. *Catalysis Letters*, *145*, 723–730. https://doi.org/10.1007/s10562-014-1455-6

Stevens, P. D., Fan, J., Gardimalla, H. M. R., & Yen, M. (2005). Superparamagnetic Nanoparticle-Supported Catalysis of Suzuki Cross-Coupling Reactions. *Organic Letters*, *7*(11), 2085–2088. https://doi.org/10.1021/ol050218w CCC:

Sydnes, M. O. (2017). The Use of Palladium onMagnetic Support as Catalyst for Suzuki–Miyaura Cross-Coupling Reactions. *CATALYSTS*, *7*, 35. https://doi.org/10.3390/catal7010035

Vats, T., Dutt, S., Kumar, R., & Siril, P. F. (2016). Facile synthesis of pristine nanocomposites with extraordinary catalytic activities using swollen liquid crystals. *Scientific Reports*, *6*, 33053. https://doi.org/10.1038/srep33053

Wang, J., Mao, M., Atif, S., & Chen, Y. (2020). Adsorption behavior and mechanism of aqueous Cr(III) and Cr(III)-EDTA chelates on DTPA-chitosan modified Fe3O4@SiO2. *Reactive and Functional Polymers*, *156*, 104720.

https://doi.org/10.1016/j.reactfunctpolym.2020.104720

Xu, W., Lin, Z., Li, G., Long, H., Du, M., Fu, G., & Pu, L. (2019). Linear PVA–DTPA–Gd conjugate for magnetic resonance imaging. *RSC Adv.*, *9*, 37052–37056. https://doi.org/10.1039/c9ra05607f

Yahya, R. O. (2022). Magnetic Graphene Oxide / Carboxymethyl - Imidazolium - Grafted Chitosan Schiff Base Nanocomposite : A New PdNPs Support for Efficient Catalytic Reduction of Hazardous Nitroarenes. *Journal of Inorganic and Organometallic Polymers and Materials*. https://doi.org/10.1007/s10904-022-02368-z

Yamashita, T., & Hayes, P. (2008). Analysis of XPS spectra of Fe2+ and Fe3+ ions in oxide materials. *Applied Surface Science*, *254*, 2441–2449. https://doi.org/10.1016/j.apsusc.2007.09.063

Zhang, Q., Wu, X., Zhao, G., Li, Y., Wang, C., Liu, Y., Gong, X., Lu, Y., Gong, X.-Q., & Lu, Y. (2015). High-performance PdNi alloy structured in situ on monolithic metal foam for coalbed methane deoxygenation via catalytic combustion. *Chem. Commun.*, *51*, 12613–12616. https://doi.org/10.1039/c5cc04389a

Zhao, D., Zhang, Q., Xuan, H., Chen, Y., Zhang, K., Feng, S., Alsaedi, A., Hayat, T., & Chen, C. (2017a). EDTA functionalized Fe 3 O 4 / graphene oxide for efficient removal of U (VI) from aqueous solutions. *Journal of Colloid And Interface Science*, *506*, 300–307. https://doi.org/10.1016/j.jcis.2017.07.057

Zhao, D., Zhang, Q., Xuan, H., Chen, Y., Zhang, K., Feng, S., Alsaedi, A., Hayat, T., & Chen, C. (2017b). Journal of Colloid and Interface Science EDTA functionalized Fe3O4/graphene oxide for efficient removal of U(VI) from aqueous solutions. *Journal of Colloid And Interface Science*, *506*, 300–307. https://doi.org/10.1016/j.jcis.2017.07.057

Appendix

XPS data interpretation of Pd@IO-DTPA

Table 5.A1: C 1s XPS

Element	IO-DTPA		Pd@IO-DTPA		Pd@IO-DTPA (R6)		Interpretation
	Peak (ev)	Area%	Peak (ev)	Area%	Peak (ev)	Area%	
C 1s	284.612	70.3	284.34	30.27	284.84	70.37	C-C/C-H
C 1s	286.085	29.7	286.34	26.57	286.12	22.83	C-N
C 1s			288.53	43.16	288.15	6.8	-COOH

Table 5.A2: N 1s XPS

Element	IO-DTPA		Pd@IO-DTPA		Pd@IO-DTPA(R6)		Interpretation
	Peak (ev)	Area%	Peak (ev)	Area%	Peak (ev)	Area%	
N 1s			399.38	36.64	399.69	50.78	
N 1s	399.746	100	400.99	63.36	400.98	49.22	C-N(C)-C

Table 5.A3: O 1s XPS

Element	IO-DTPA		Pd@IO-DTPA		Pd@IO-DTPA (R6)		Interpretation
	Peak (ev)	Area%	Peak (ev)	Area%	Peak (ev)	Area%	
O 1s	530.453	66.1	530	40.50	529.99	38.22	Bulk Fe-O, Pd-O
O 1s					531.17	20.03	-OH
O 1s	532.640	33.9	531.66	39.09	532.57	29.07	C=O
O 1s			533.05	20.41	533.76	12.68	C-O-C

Table 5.A4: Fe 2p XPS

Element	IO-DTPA		Pd@IO-DTPA		Pd@IO-DTPA(R6)		Interpretation
	Peak (ev)	Area%	Peak (ev)	Area%	Peak (ev)	Area%	
Fe 2p3/2			710.25	17.21	710.12	17.34	Fe^{3+} octahedral
Fe 2p3/2	711.568	67.0	711.96	15.21	711.05	17.60	Fe^{3+} octahedral
Fe 2p3/2			713.94	13.06	713.92	12.13	Fe^{3+} Tetrahedral

Fe 2p3/2			717.43	9.99	717.58	10.07	Fe^{2+} octahedral
Fe 2p3/2			720.44	9.67	720.52	7.78	Satellite peak
Fe 2p1/2			723.25	8.61	723.12	8.67	Fe^{3+} octahedral
Fe 2p1/2	724.360	33.0	724.96	7.61	724.85	8.80	Fe^{3+} octahedral
Fe 2p1/2			726.94	6.53	726.92	6.07	Fe^{3+} Tetrahedral
Fe 2p1/2			729.51	6.54	729.73	8.28	Fe^{2+} octahedral
Fe 2p1/2			733.36	5.59	733.48	3.26	Satellite peak

Table 5.A5: Pd 3d XPS

Element	Pd@IO-DTPA		Pd@IO-DTPA (R6)		Interpreatation
	Peak (eV)	Area%	Peak (eV)	Area%	
Pd 3d5/2			334.11	12.52	Pd (0) (higher electron density) indication aggregation of Pd nano
Pd 3d5/2	335.41	25.30			Pd (0)
Pd 3d5/2	336.35	21.72	335.58	28.89	Pd (2+)
Pd 3d5/2	338.58	12.98	338.32	5.92	PdO
Pd 3d3/2			338.92	19.89	Pd (0)
Pd 3d3/2	340.51	16.87			Pd (0)
Pd 3d3/2	341.45	14.48	341.29	19.76	Pd (2+)
Pd 3d3/2	342.82	8.65	342.36	13.02	PdO

XPS data interpretation of Pd@Ni@IO-DTPA

Table 5.A6: C 1s XPS

Element	Ni@IO-DTPA		Pd@Ni@IO-DTPA		Pd@Ni@IO-DTPA (R10)		Interpretation
	Peaks (eV)	Area%	Peaks (eV)	Area%	Peaks (eV)	Area%	
C 1s	284.5	65.13	284.5	74.21	284.5	56.50	C-C/C-H
C 1s	285.48	17.19	285.7	15.68	285.59	30.27	C-0-C/C-O
C 1s	286.34	10.28	286.49	4.71	286.83	7.97	C-N

C 1s	288.23	6.68	287.99	5.39	288.20	5.26	-COOH

Table 5.A7: N 1s XPS

Element	Ni@IO-DTPA		Pd@Ni@IO-DTPA		Pd@Ni@IO-DTPA (R10)		Interpretation
	Peaks (eV)	Area%	Peaks (eV)	Area%	Peaks (eV)	Area%	
N 1s	398.59	61.73	397.65	57.56	397.37	36.06	
N 1s	399.55	25.74	399.26	29.42	399.24	15.68	
N 1s	400.97	12.53	401.01	12.83	401.04	48.27	C-Ni-C

Table 5.A8: O1s XPS

Element	Ni@IO-DTPA		Pd@Ni@IO-DTPA		Pd@Ni@IO-DTPA (R10)		Interpretation
	Peaks (eV)	Area%	Peaks (eV)	Area%	Peaks (eV)	Area%	
O 1s	530	56.81	530.03	79.79	529.93	15.75	Bulk Fe-O, Pd-O
O 1s	531.12	21.20	531.40	16.30	531.22	20.69	-OH
O 1s	532.65	21.99	532.52	3.91	532.99	41.11	C=O
O 1s					534.06	22.45	C-O-C

Table 5.A9: Fe2p XPS

Element	Ni@IO-DTPA		Pd@Ni@IO-DTPA		Pd@Ni@IO-DTPA (R10)		Interpretation
	Peaks (eV)	Area%	Peaks (eV)	Area%	Peaks (eV)	Area%	
Fe2p3/2	709.98	33.94	709.99	24.06	709.97	20.59	Fe3+ octahedral
Fe2p3/2	711.71	15.50	711.60	16.47	711.96	16.66	Fe3+ octahedral
Fe2p3/2	713.37	4.37	713.49	11.08	713.9	9.56	Fe3+ Tetratahedral
Fe2p3/2	714.69	4.24					Fe^{2+} octahedral 2p3/2
Fe2p3/2			716.69	6.15	717.07	10.77	Fe2+ octahedral
Fe2p3/2	718.35	7.13					Fe^{3+} 2p3/2
Fe2p3/2			719.39	7.56	720.02	7.34	Satellite peak of Fe3+ 2p3/2
Fe2p1/2	722.98	16.97	722.99	12.03	722.97	10.30	Fe^{3+} octahedral
Fe2p1/2	724.71	7.75	724.60	8.24	724.96	8.33	Fe^{3+} octahedral
Fe2p1/2	726.37	2.18	726.49	5.54	726.9	4.78	Fe^{3+} Tetratahedral
Fe2p1/2	727.69	2.12					Fe^{2+} octahedral 2p3/2

Fe2p1/2			729.17	3.73	729.12	6.09	
Fe2p1/2	732.74	5.80	732.83	5.14	732.96	5.57	

Table 5.A10: Ni2p XPS

Element	Ni@IO-DTPA		Pd@Ni@IO-DTPA		Pd@Ni@IO-DTPA (R10)		Interpretation
	Peaks (eV)	Area%	Peaks (eV)	Area%	Peaks (eV)	Area%	
Ni2p3/2	852.61		852.59	27.40	852.62		Ni metal
Ni2p3/2	854.40	12.55	853.98	15.19	854.26	29.07	NiO
Ni2p3/2	855.39	28.84	855.14	9.92	855.99	6.89	
Ni2p3/2	857.53	8.88	856.49	6.26	857.09	16.11	
Ni2p3/2	859.04	6.69	858.85	15.37	859.21	4.91	Ni(OH)2
Ni2p3/2	861.01	13.94	860.60	5.88	860.24	17.71	Satellite (Ni metal)
Ni2p3/2	862.58	16.61	863.14	6.58	861.60	14.60	satellite (higher oxidation state of Ni
Ni2p3/2	864.57	1.97	863.90	3.23	862.77	6.06	satellite
Ni2p3/2			864.97	2.91			
Ni2p3/2	866.72	8.73	866.68	5.72			satellite (NiO)
Ni2p3/2			867.46	1.55			

Table 5.A11: Pd 3d XPS

Element	Pd@Ni@IO-DTPA		Interpretation	Pd@Ni@IO-DTPA (R10)		Interpretation
	Peaks (eV)	Area%		Peaks (eV)	Area%	
Pd3d5/2	335.13	17.77	Pd(0)	334.9	19.47	Pd(0)
Pd3d5/2	335.96	3.52	Pd(Ni)	336.37	27.47	Pd^{2+}
Pd3d5/2	338.88	27.10	Pd-O/Pd-N	338.26	20.36	Pd-O/Pd-N
Pd3d5/2	339.94	21.03				
Pd3d3/2	340.39	11.18	Pd(0)	339.28	9.39	Pd(0)
Pd3d3/2	341.22	2.35	Pd(Ni)	341.38	18.13	Pd^{2+}

Pd3d3/2	344.14	18.07	PdO/Pd-N	342	5.17	Pd-O/Pd-N

GC-MS spectra of optimization of Suzuki coupling reaction catalysed by Pd@IO-DTPA

GC MS spectra during screening of solvent for the reaction between Iodobenzene and phenylboronic acid (Figure 5.A1 **(A-O))**

Use of DMF and toluene gave very low conversions (Table **S5.12** entry 4). Alcohols such as EtOH, i-PrOH were found to be poor solvents (Table **S5.12** entries 2&3). But THF (Table 2 entry 5) as well as alcohols with water in different ratios (Table **S5.12** entries 6-9) gave good catalytic conversion

Entry	Solvent	Temp (°C)	Time (h)	GC-MS Yield
1.	Water	80	12	100
2.	Ethanol	30- 80	12	0
3.	Isopropanol	30-80	12	0-Trace
4.	DMF, Toluene	30-100	12	0
5.	THF	30	12	0
6.	THF	80	12	88.5
7.	Ethanol: Water (9:1, 7:3,1:1)	80	12	0-trace
8.	Isopropanol: Water (9:1)	80	12	100
9.	Isopropanol: Water (9:1)	30	12	75.14
10.	Isopropanol: Water (7:3, 3:7,1:1)	30-80	12	100

Table 5.A12: *Optimization of solvent,* ***Recation condition:*** *Iodobenzene (1.59 mmol), Phenylboronic acid (1.59 mmol), catalyst dose:1 mg, solvent(10 ml), TLC (n-hexane), GC-MS (HPLC grade chloroform), Base-* K_2CO_3 (2 equi.)

Optimization of Solvent

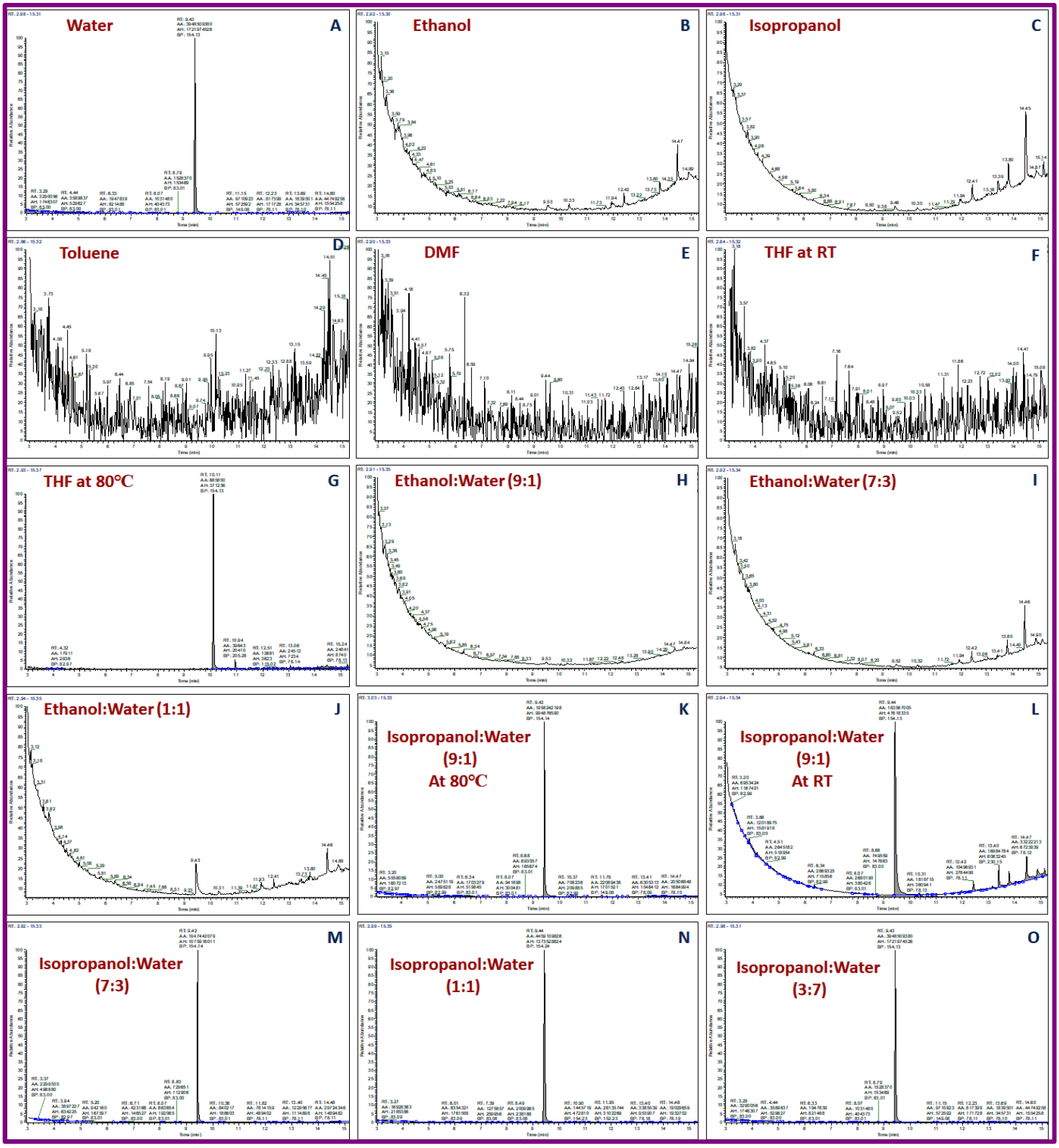

Figure 5.A1*: GC-MS spectra of the product for Pd@IO-DTPA catalysed reaction between iodobenzene and phenylboronic acid performed using K_2CO_3 In different solvents.*

GC MS spectra during screening of catalyst amount, base, amount of base and temperature for the reaction between Iodobenzene and phenylboronic acid (Figures 5.A2, 5.A3, 5.A4)

Entry	Catalyst (mg)	Base	Temp (°C)	Time (h)	GC-MS Yield
1.	1-50 mg (0.0037 - 0.18 mol% Pd)	K_2CO_3 (2 equi.)	100	12	100
2.	1 (0.0037 mol% Pd)	K_2CO_3 (2 equi.)	60	12	100
3.	1 (0.0037 mol% Pd)	K_2CO_3 (2 equi.)	30	12	100
4.	1(0.0037 mol% Pd)	Triethyl amine (TEA) (2 equi.)	30-100	12	100
5.	1	Na_2CO_3 (2 equi.)	30-100	12	100
6.	1	KOH (2 equi.)	100	12	100
7.	1	KOH (2 equi.)	30	12	78.45
8.	1	NaOH (2 equi.)	100	12	100
9.	1	NaOH (2 equi.)	30	12	57.45
10.	1	K_2CO_3 (0.2- 1.5 equi.)	100	12	100
11.	1	K_2CO_3 (0.1 equi.)	100	12	79.79
12.	1	No base	100	12	0%
13.	1	K_2CO_3 (1 equi.)	30-100	12	100

Table 5.A13: *Optimization of Base and Temperature,* ***Reaction conditions****: Iodobenzene (1.59 mmol), Phenylboronic acid (1.59 mmol), Water (solvent) (10 ml), TLC (n-hexane), GC-MS (HPLC grade chloroform), Yields were obtained by GC-MS analysis*

Optimization of catalyst amaount

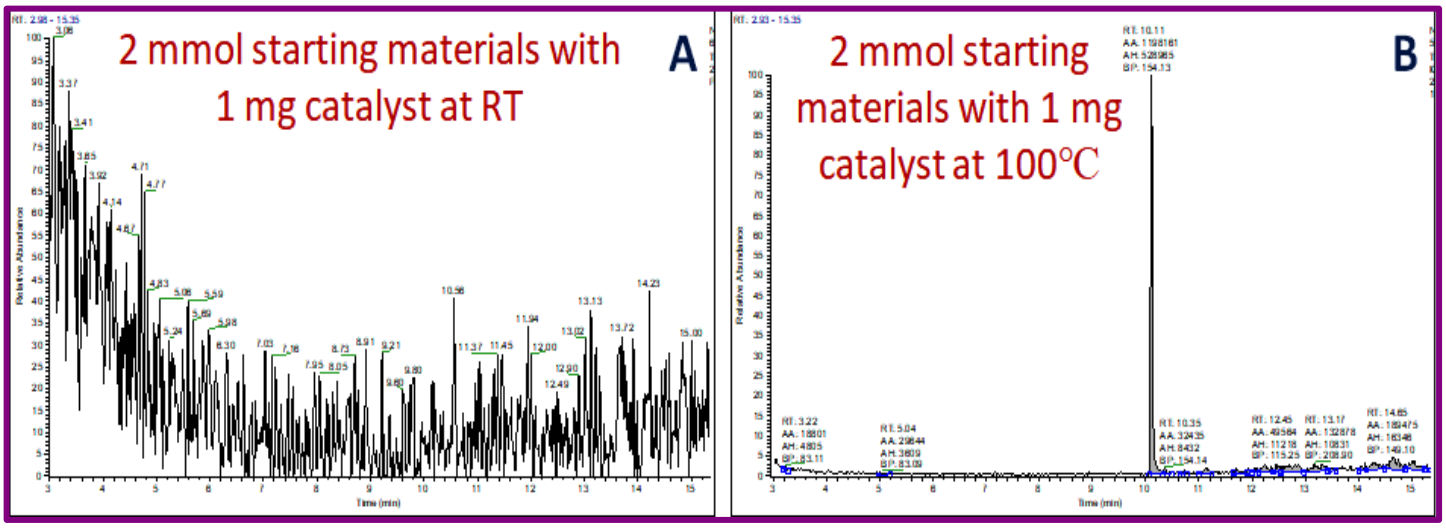

Figure 5.A2: GC-MS spectra of the product for Pd@IO-DTPA catalysed reaction between iodobenzene and phenylboronic acid performed using K_2CO_3 and water as a solvent

Optimization of Base

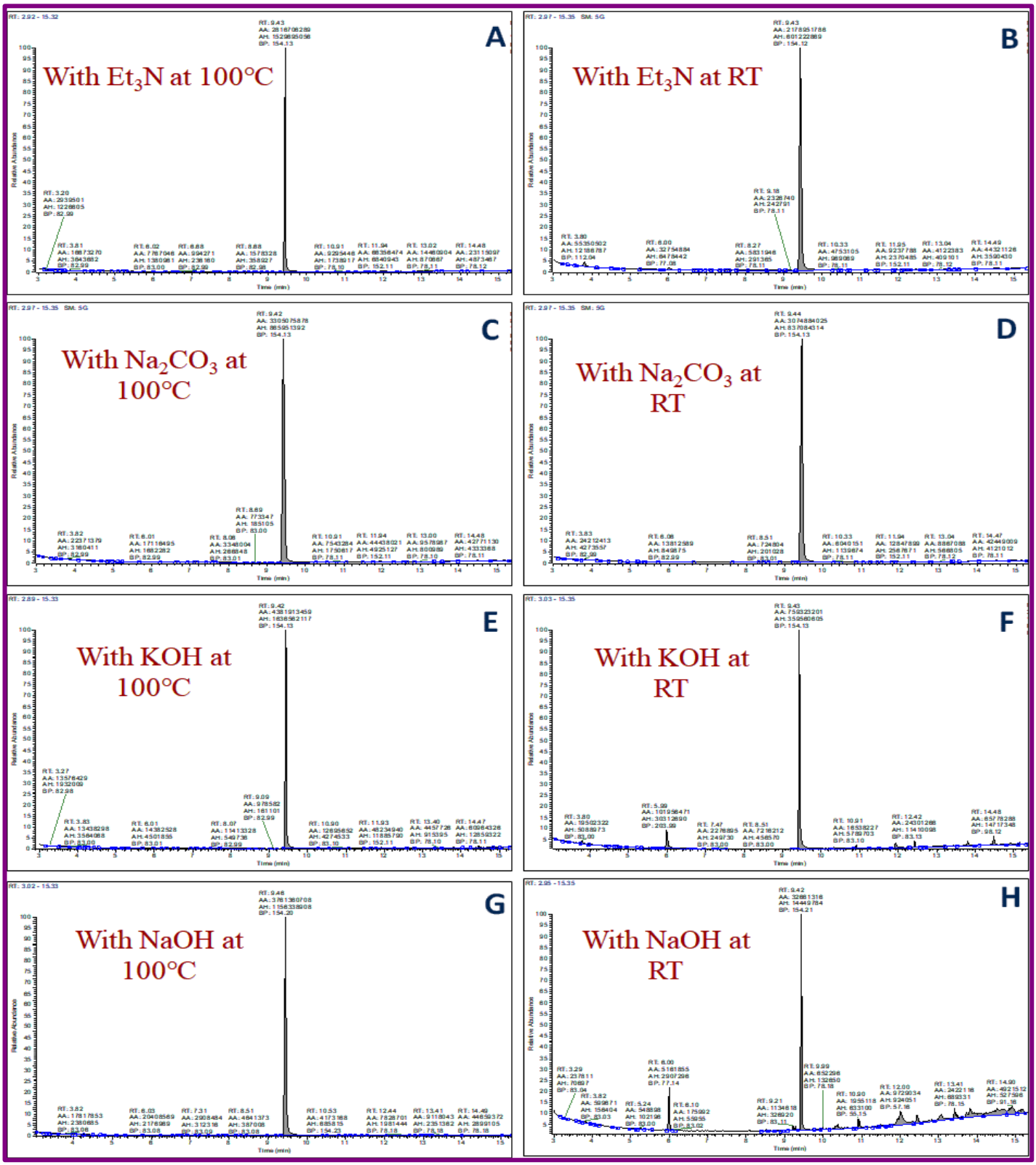

Figure 5.A3: GC-MS spectra of the product for Pd@IO-DTPA catalysed reaction between iodobenzene and phenylboronic acid performed using different base and water as a solvent

Optimization of amount of base

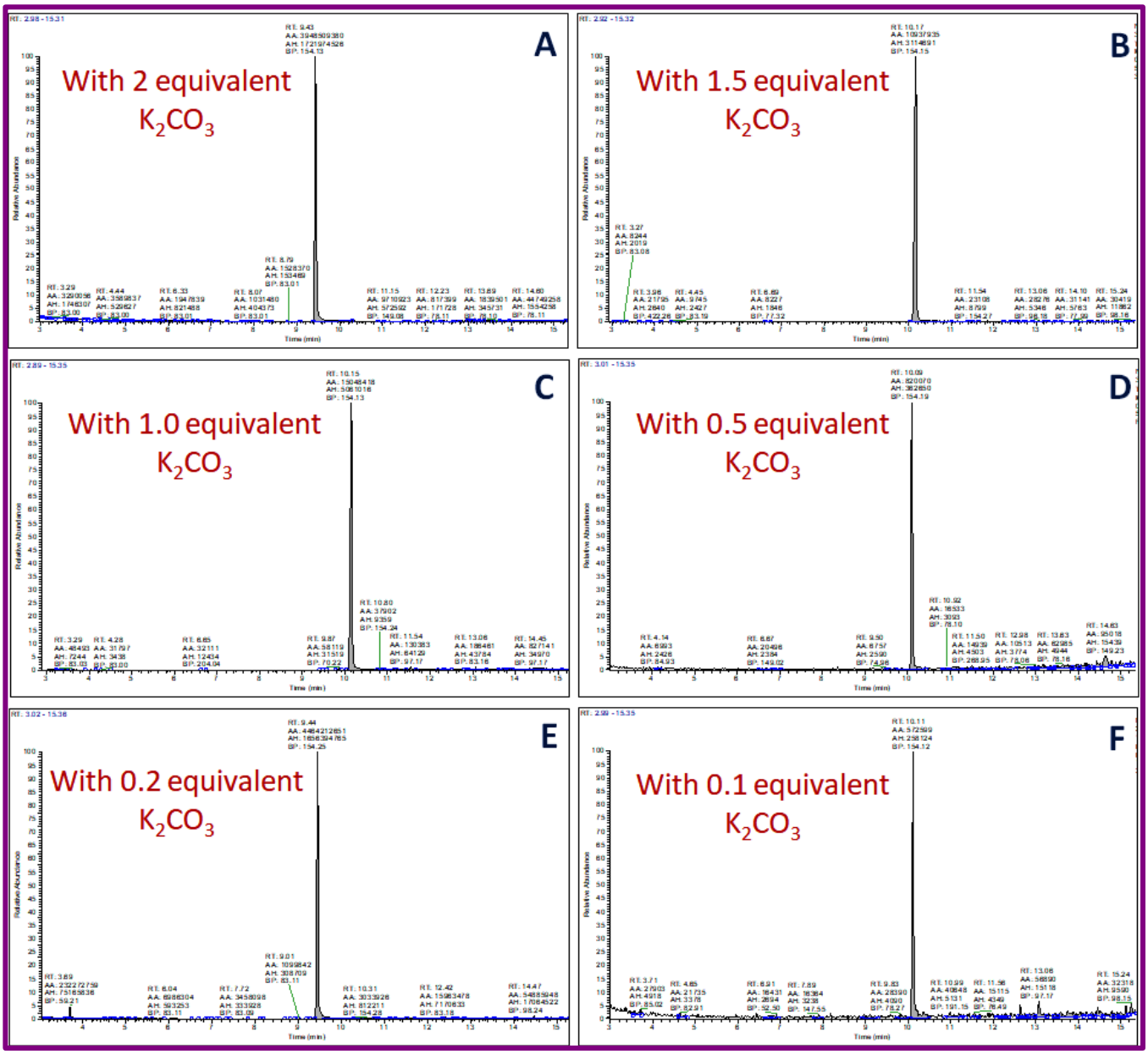

Figure 5.A4: GC-MS spectra of the product for Pd@IO-DTPA catalysed reaction between iodobenzene and phenylboronic acid performed using different amount of base and water as a solvent

Optimization of Time:

Time study of Pd@IO-DTPA catalysed reaction between iodobenzene and phenyl boronic acid performed at 35°C and at 100 °C. It was observed that reaction takes 7 hours for completion (Figures S5.8(A-G))

Entry	Catalyst (mg)	Solvent	Base	Temp (°C)	Time (h)	GC-MS Yield
1. 1	1	Water	K_2CO_3 (1 equi.)	30	12	100
2. 2	1	Water	K_2CO_3 (1 equi.)	30	8	100
3. 3	1	Water	K_2CO_3 (1 equi.)	30	7	100
4. 4	1	Water	K_2CO_3 (1 equi.)	30	6	88.9
5. 5	1	Water	K_2CO_3 (1 equi.)	30	5	72.3
6. 6	1	Water	K_2CO_3 (1 equi.)	30	4	71.7
7. 7	1	Water	K_2CO_3 (1 equi.)	30	3	60.8
8. 8	1	Water	K_2CO_3 (1 equi.)	30	2	49.5
9. 9	1	Water	K_2CO_3 (1 equi.)	30	1	33.23

Table 5.A14: *Optimization of time,* ***Reaction conditions****: Iodobenzene (1.59 mmol), Phenylboronic acid (1.59 mmol), Water (solvent) (10 ml), TLC (n-hexane), GC-MS (HPLC grade chloroform), Yields were obtained by GC-MS analysis*

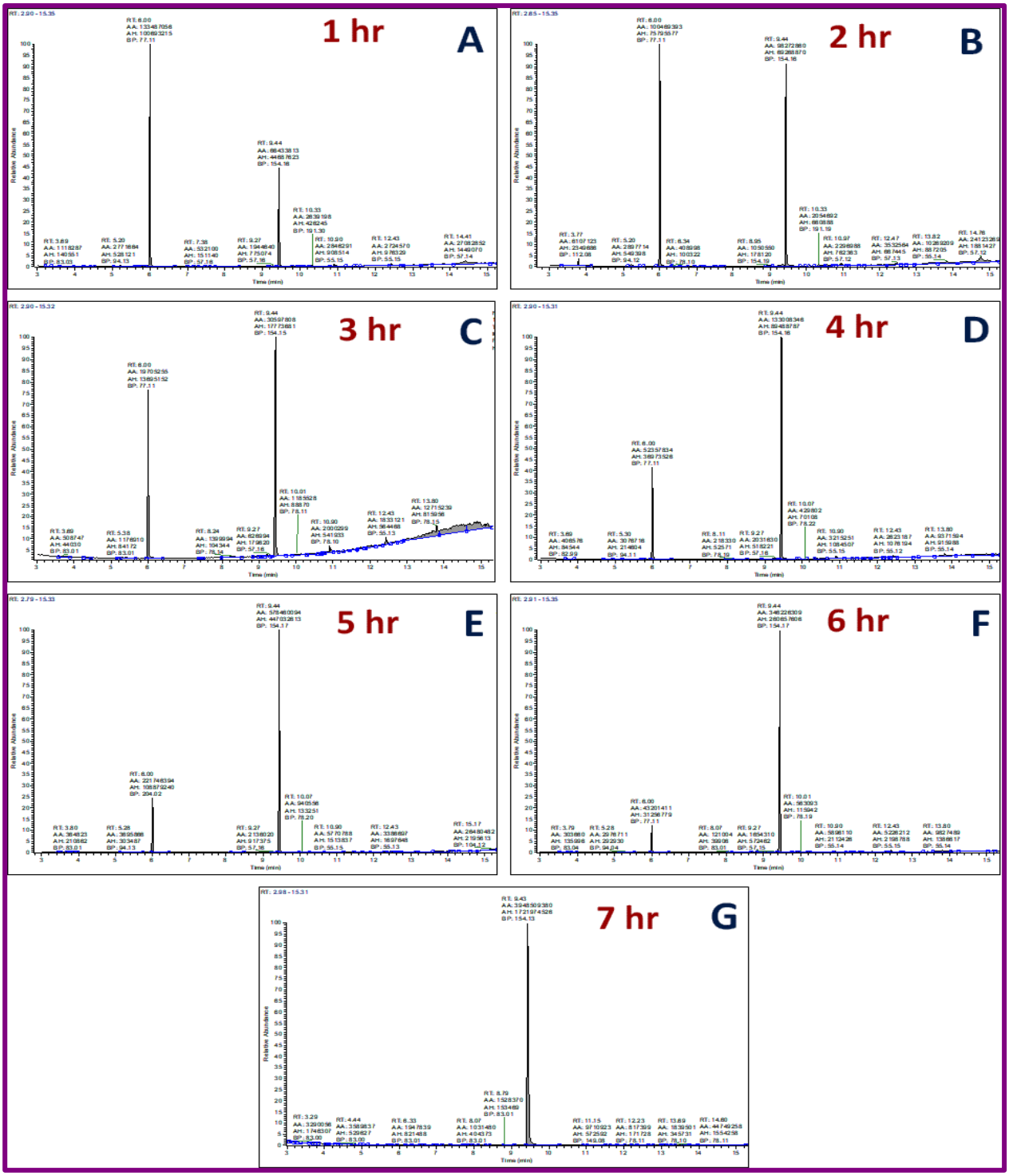

Figure 5.A5: *GC-MS spectra of the product for Pd@IO-DTPA catalysed reaction between Iodobenzene and phenyl boronic acid performed at 35 °C in the time range 1 to 7 hours*

GC-MS spectra of optimization of Suzuki coupling reaction catalysed by Pd@Ni@IO-DTPA

Table 5.A15: Optimization of Suzuki coupling reaction

Sr. No.	Catalyst (mg)	Solvent	Base	Temp (°C)	Time (h)	GC-MS Yield (%)
Optimization of Solvent						
1.	1	Ethanol	K_2CO_3 (2 equi.)	80	12	61.77
2.	1	Isopropanol	K_2CO_3 (2 equi.)	80	12	13.29
3.	1	DMF	K_2CO_3 (2 equi.)	100	12	20.66
4.	1	THF	K_2CO_3 (2 equi.)	80	12	0.07
5.	1	Toluene	K_2CO_3 (2 equi.)	100	12	0
6.	1	Ethanol: Water (1:1)	K_2CO_3 (2 equi.)	80	12	75.86
7.	1	Ethanol: Water (7:3)	K_2CO_3 (2 equi.)	80	12	100
8.	1	Isopropanol: Water (9:1)	K_2CO_3 (2 equi.)	80	12	100
9.	1	Isopropanol: Water (3:7)	K_2CO_3 (2 equi.)	80	12	100
10.	1	Isopropanol: Water (1:1)	K_2CO_3 (2 equi.)	80	12	100
11.	1	Water	K_2CO_3 (2 equi.)	80	12	100
12.	1	Water	K_2CO_3 (2 equi.)	100	12	100
13.	1	Water	K_2CO_3 (2 equi.)	80	12	100
14.	1	Water	K_2CO_3 (2 equi.)	60	12	100
15.	1	Water	K_2CO_3 (2 equi.)	40	12	100
16.	1	Water	K_2CO_3 (2 equi.)	30	12	100
17.	1	Water	Na_2CO_3 (2 equi.)	30	12	100
18.	1	Water	NaOH (2 equi.)	30	12	100
19.	1	Water	KOH (2 equi.)	30	12	100

20.	1	Water	TEA (2 equi.)	30	12	18.49
21.	1	Water	K_2CO_3 (2 equi.)	30	12	100
22.	1	Water	K_2CO_3 (1.0 equi.)	30	12	100
23.	1	Water	K_2CO_3 (0.5 equi.)	30	12	100
24.	1	Water	K_2CO_3 (0.3 equi.)	30	12	91.17
25.	1	Water	K_2CO_3 (0.1 equi.)	30	12	70.34
26.	1	Water	K_2CO_3 (1 equi.)	30	12	100
27.	1	Water	K_2CO_3 (1 equi.)	30	10	100
28.	1	Water	K_2CO_3 (1 equi.)	30	8	100
29.	1	Water	K_2CO_3 (1 equi.)	30	6	100
30.	1	Water	K_2CO_3 (1 equi.)	30	5	100
31.	1	Water	K_2CO_3 (1 equi.)	30	3	66.65
32.	1	Water	K_2CO_3 (1 equi.)	30	1	47.01
33.	1 (with 1.59 mmol starting material (0.00704 mol% Pd)	Water	K_2CO_3 (2 equi.)	30	5	100
34.	1 mg (with 2 mmol starting material) (0.0056 mol% Pd)	Water	K_2CO_3 (2 equi.)	30	5	100
35.	1 mg Ni@IO-DTPA	Water	K_2CO_3 (2 equi.)	100	12	0
36.	No catalyst	Water	K_2CO_3 (2 equi.)	100	12	0

Optimization of solvent:

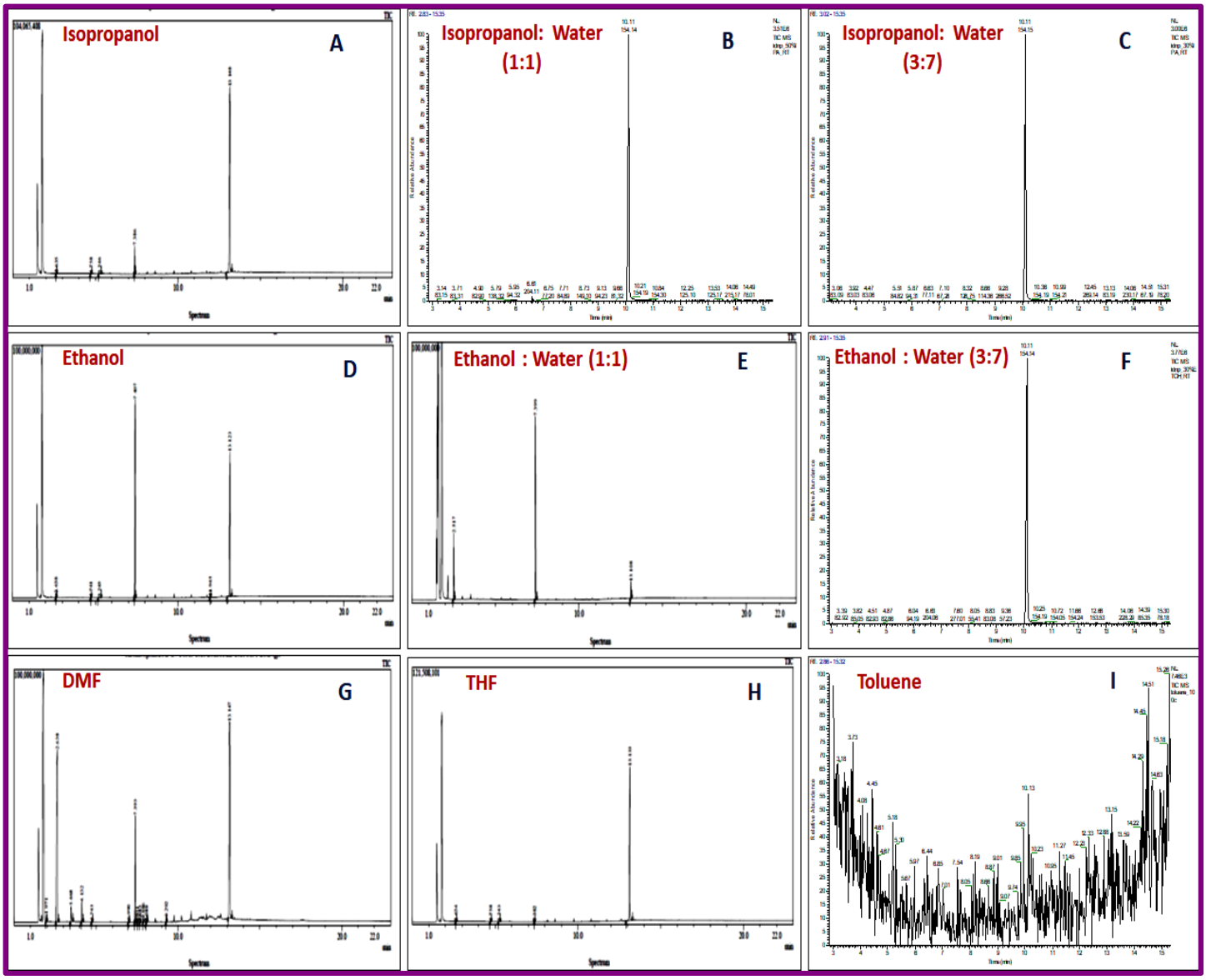

Figure 5.A6: *GC-MS spectra of Solvent optimization study of the product for Pd@Ni@IO-DTPA catalysed reaction between (1.59 mmol) Iodobenzene and (1.59 mmol) Phenylboronic acid performed using (2 equivalent) K_2CO_3 and at 30°C*

Optimization of temperature

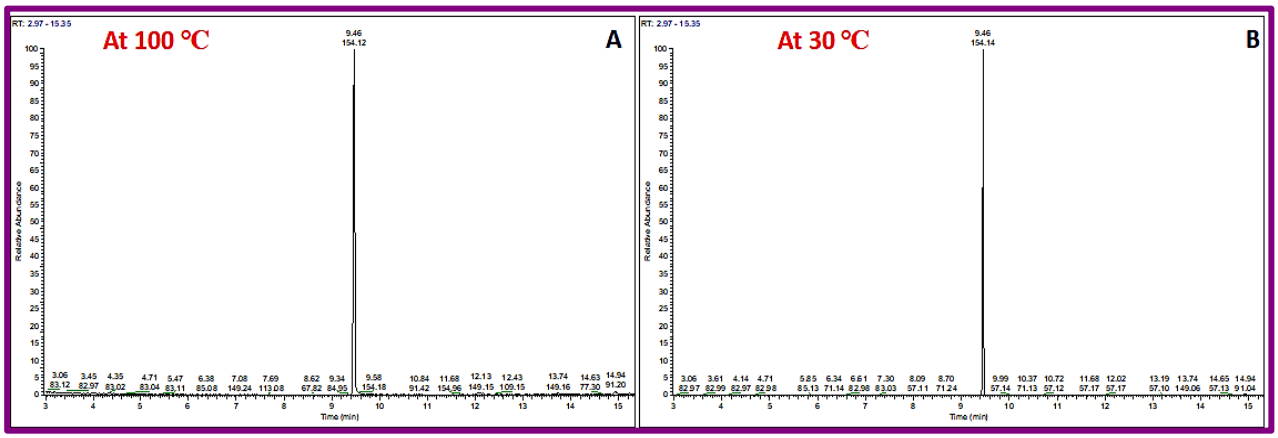

Figure 5.A7 *GC-MS spectra of Temperature optimization study of the product for Pd@Ni@IO-DTPA catalysed reaction between (1.59 mmol) Iodobenzene and (1.59 mmol) Phenylboronic acid performed using 2 equivalent of K_2CO_3 and at 30°C and 100 °C*

Optimization of Base

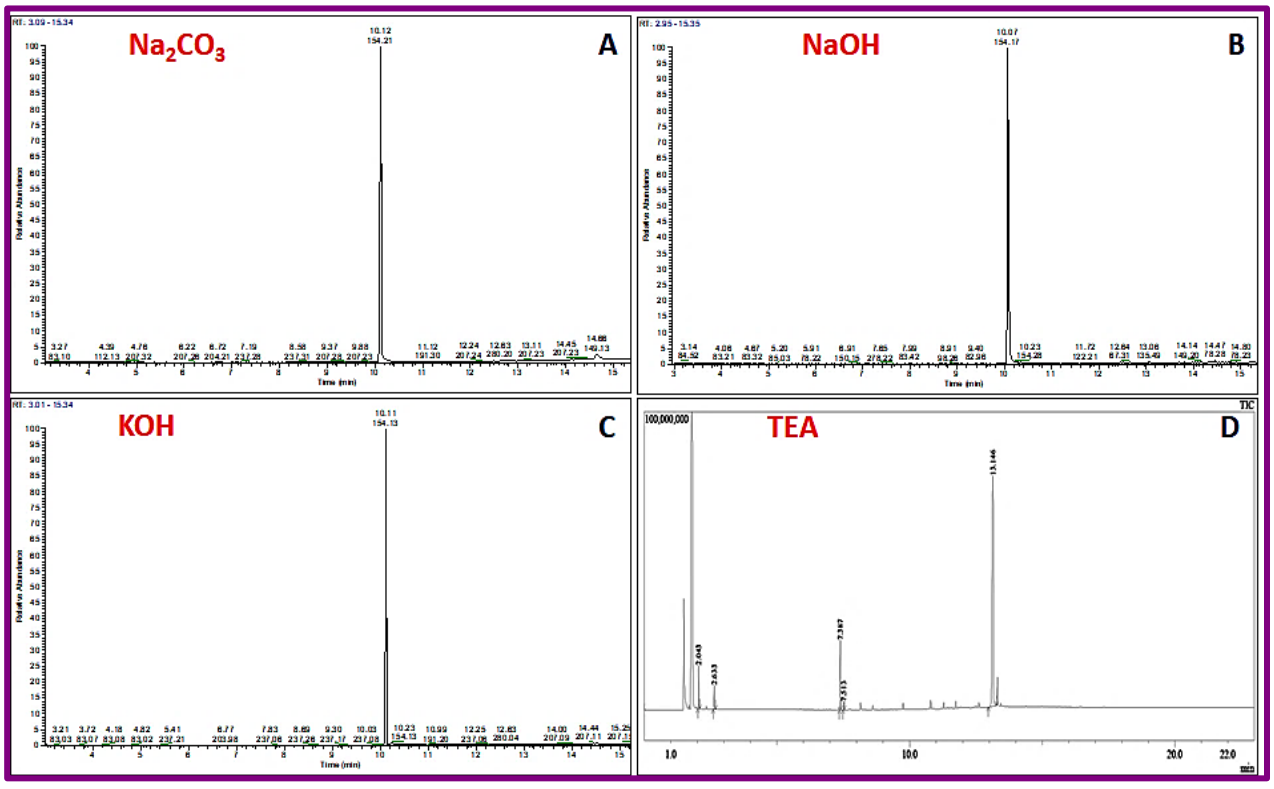

Figure 5.A8: *GC-MS spectra of Base optimization study of the product for Pd@Ni@IO-DTPA catalysed reaction between (1.59 mmol) Iodobenzene and (1.59 mmol) Phenylboronic acid performed using 2 equivalent of different bases and at 30°C.*

Optimization of amount of Base

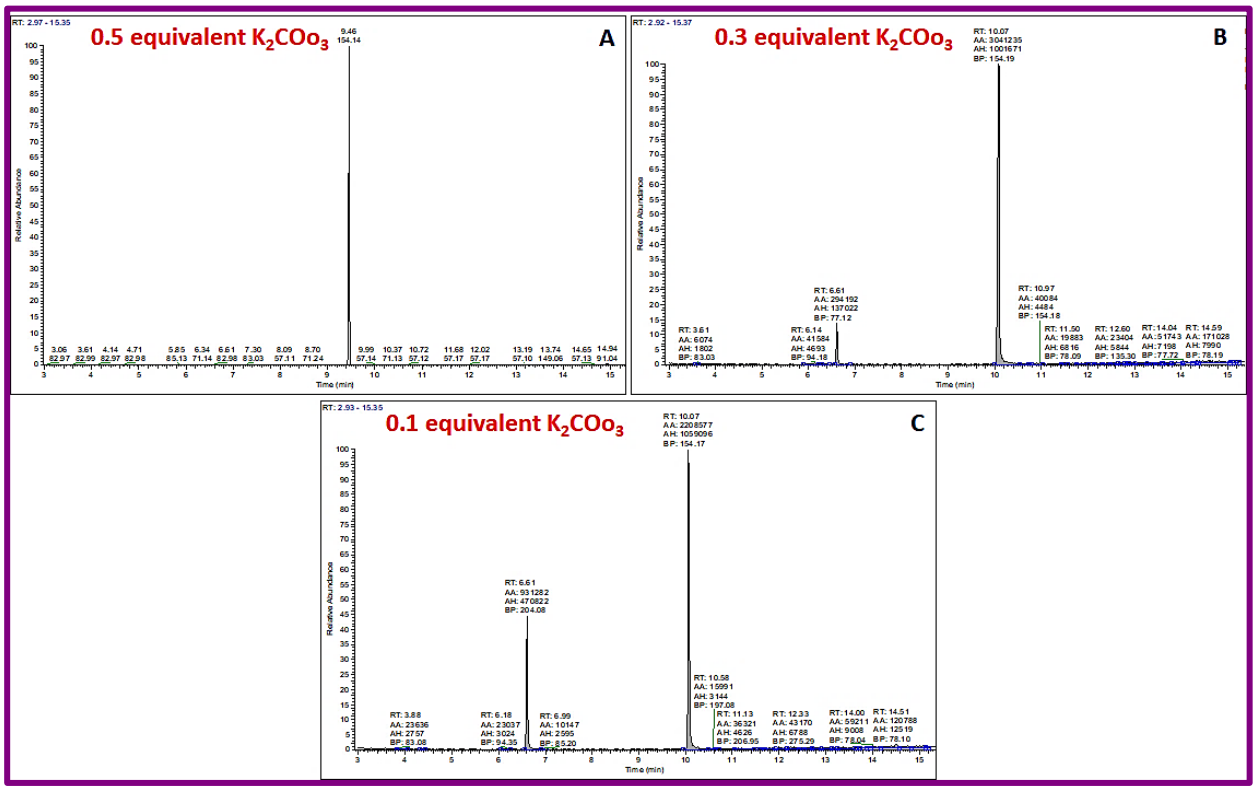

Figure 5.A9: *GC-MS spectra of amount of base optimization study of the product for Pd@Ni@IO-DTPA catalysed reaction between (1.59 mmol) Iodobenzene and (1.59 mmol) Phenylboronic acid performed using different amount of K_2CO_3 and at 30°C.*

Optimization of Time

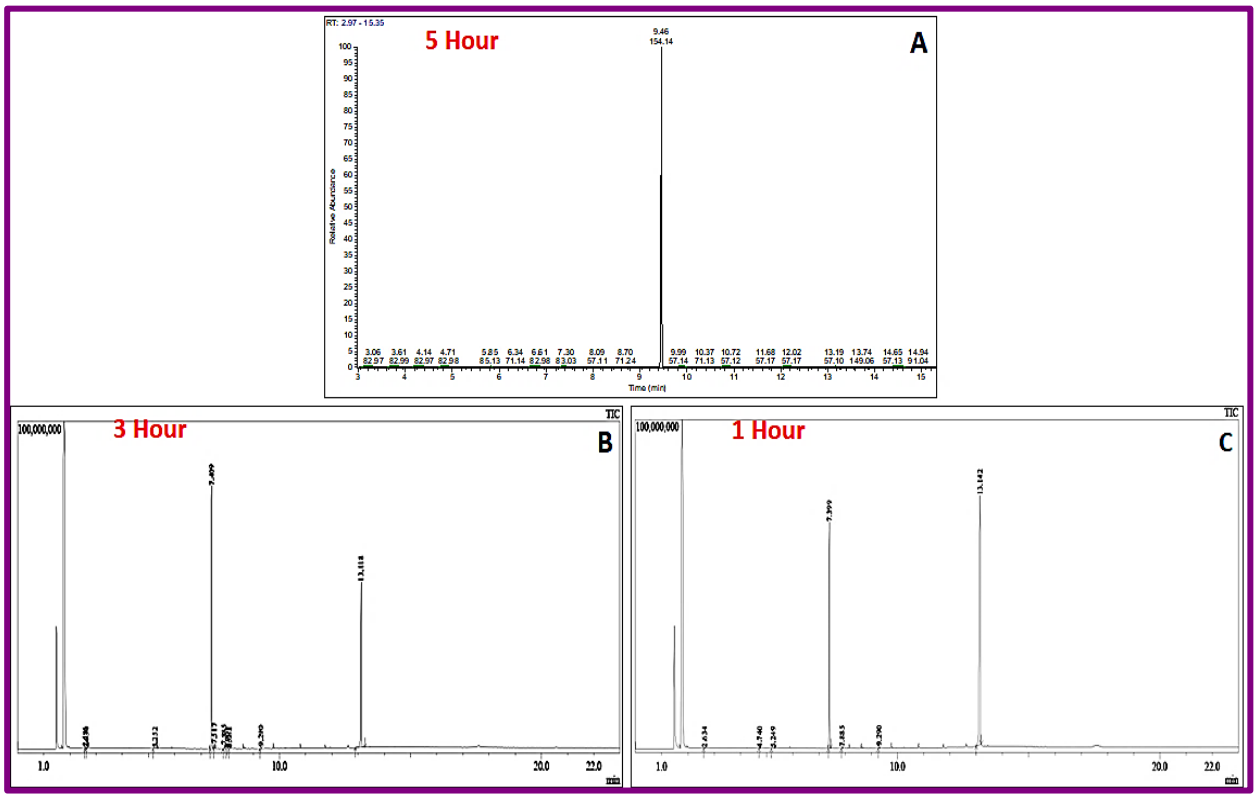

Figure 5.A10: *Pd@Ni@IO-DTPA catalysed reaction between (1.59 mmol) Iodobenzene and (1.59 mmol) Phenylboronic acid performed using 0.5 equivalent of K_2CO_3 and at 30°C.*

Optimization of amount of catalyst

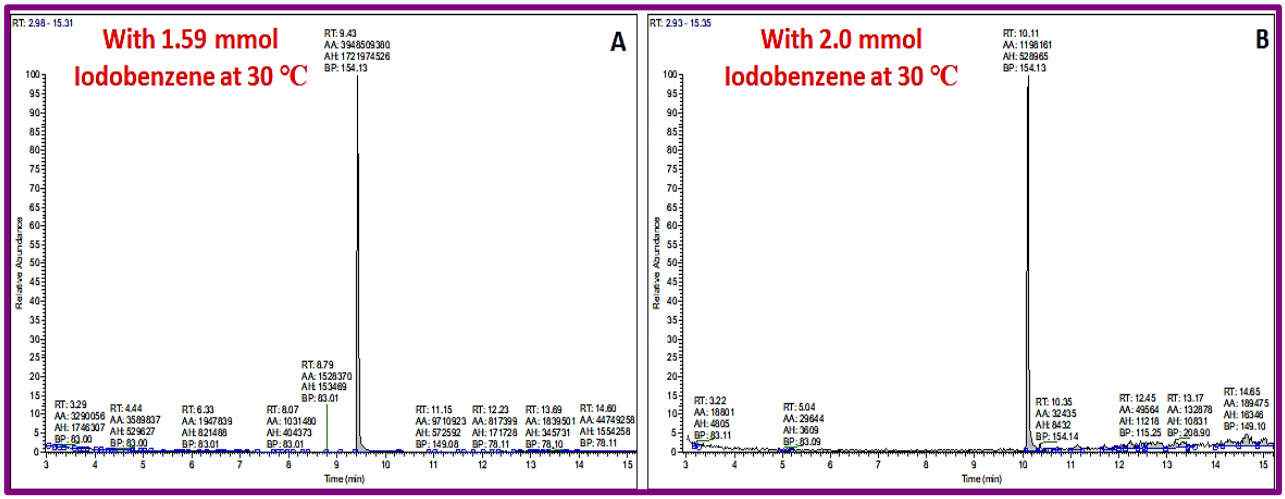

Figure 5.A11: *GC-MS spectra of Temperature optimization study of the product for Pd@Ni@IO-DTPA catalysed reaction between Iodobenzene and Phenylboronic acid performed using 0.5 equivalent of K_2CO_3 and at 30°C*

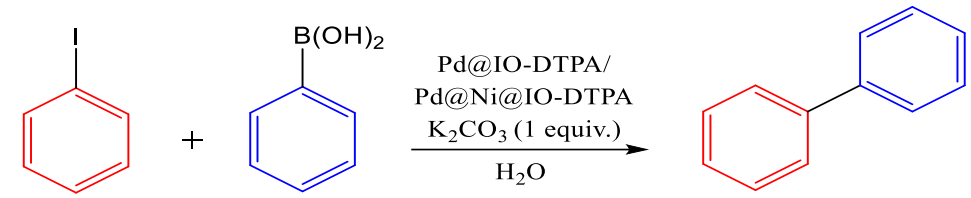

iodobenzene phenylboronic acid 1,1'-biphenyl

M.P: 70 °C

Molecular weight: 154.21 gm/mol

Pd@IO-DTPA

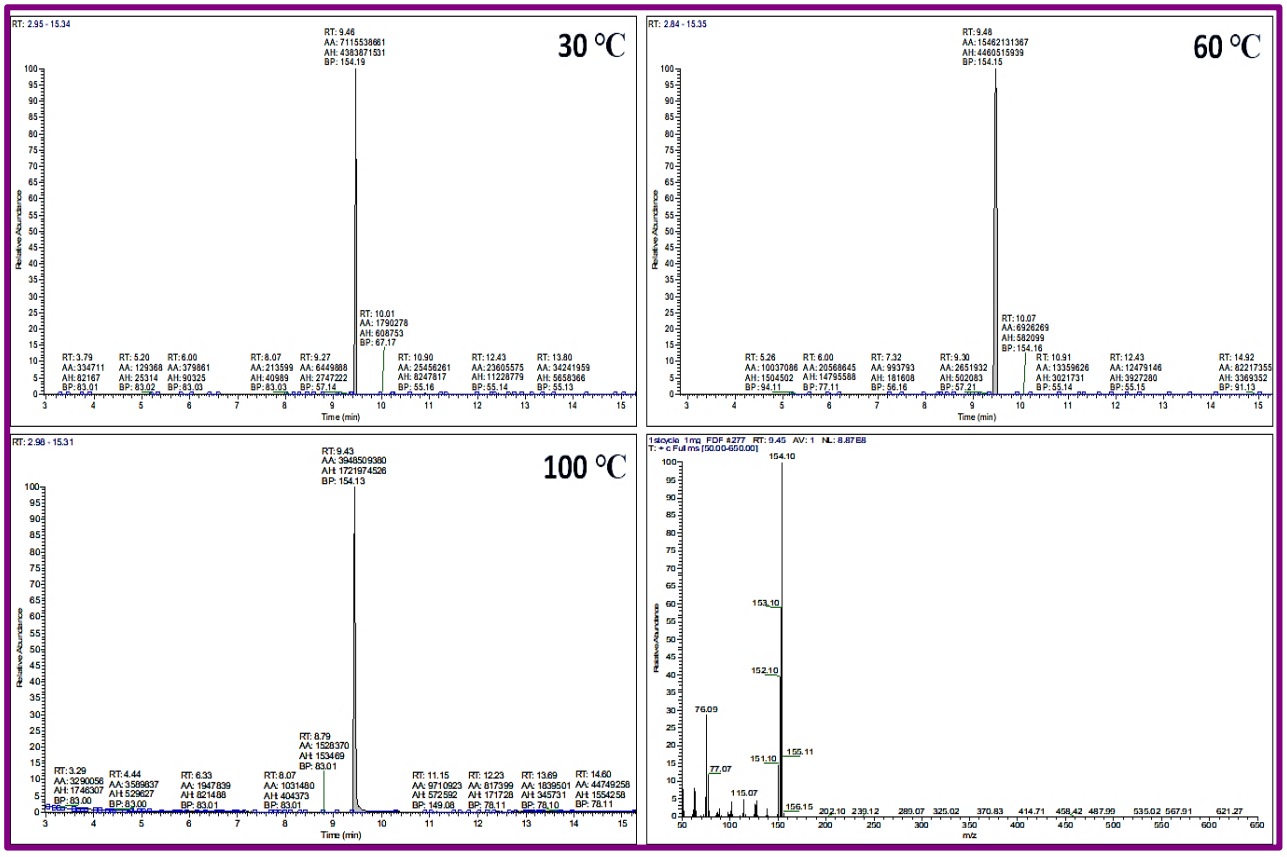

Figure 5.A12: GC-Ms spectra of crude product (Biphenyl) synthesized From Iodobenzene at RT, 60°C and 100 °C

Pd@Ni@IO-DTPA

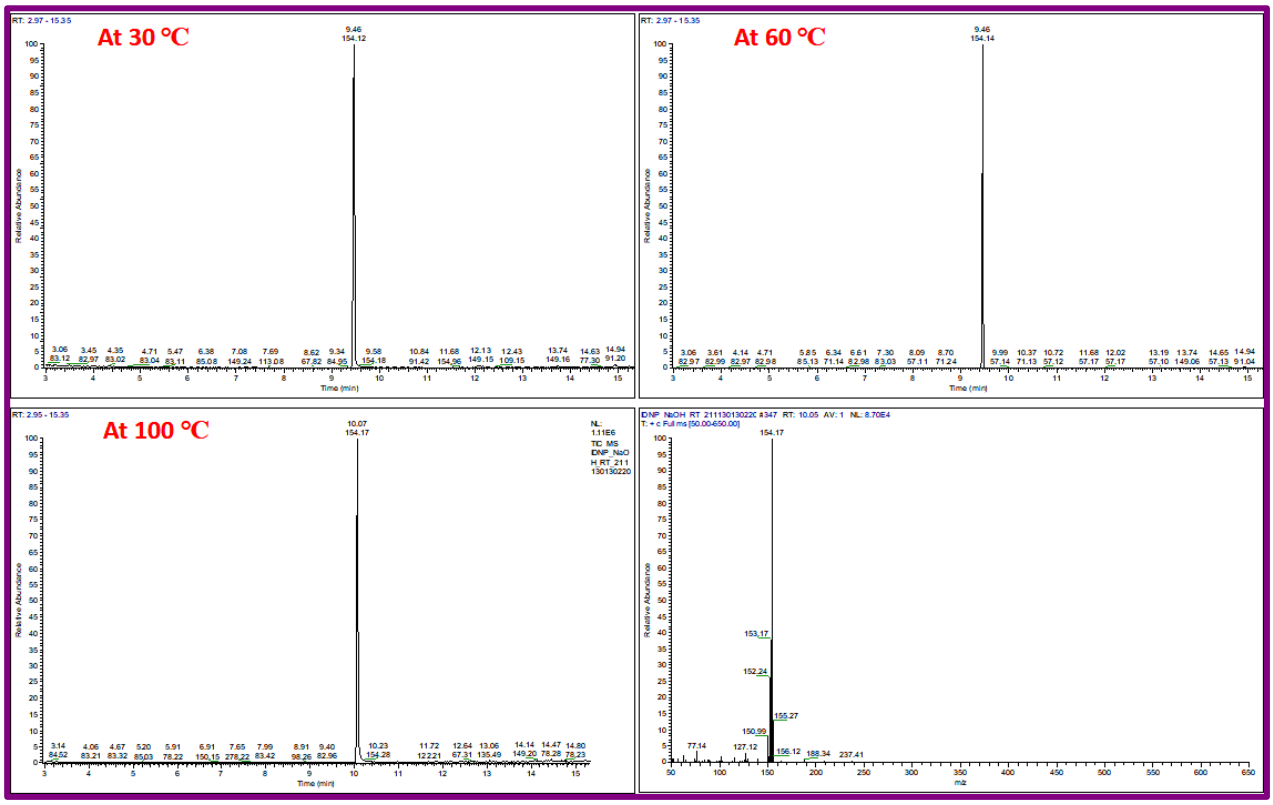

Figure 5.A13*:* GC-Ms spectra of crude product (Biphenyl) synthesized From Iodobenzene at RT, 60°C and 100 °C

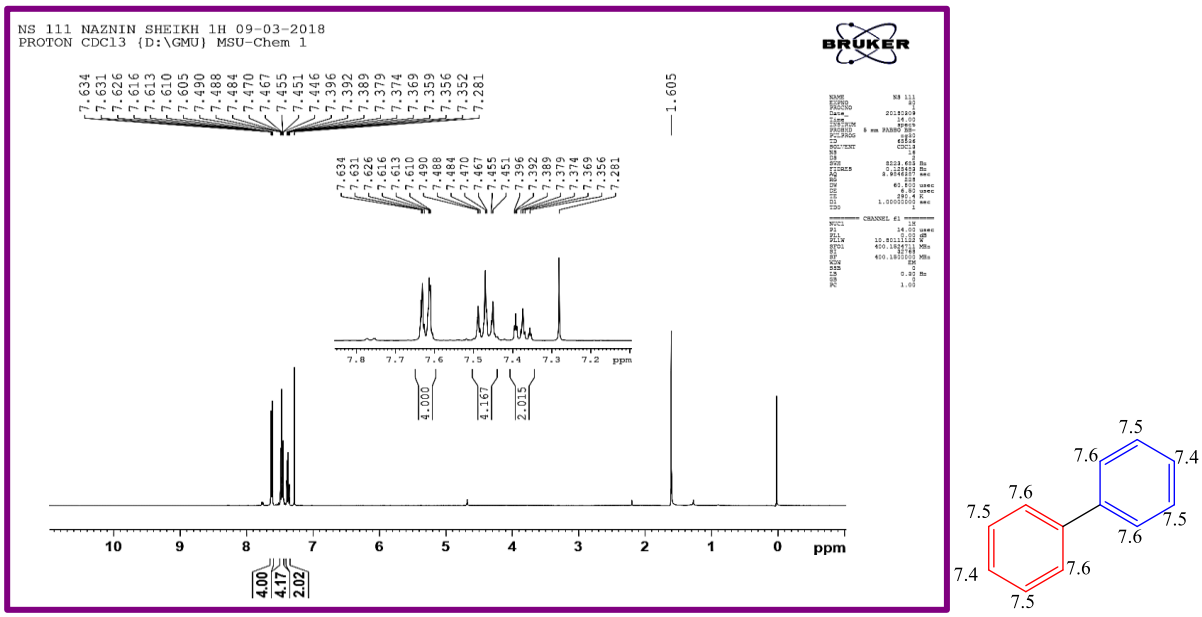

Figure 5.A14: NMR spectra of column purified (Biphenyl) synthesized From Iodobenzene

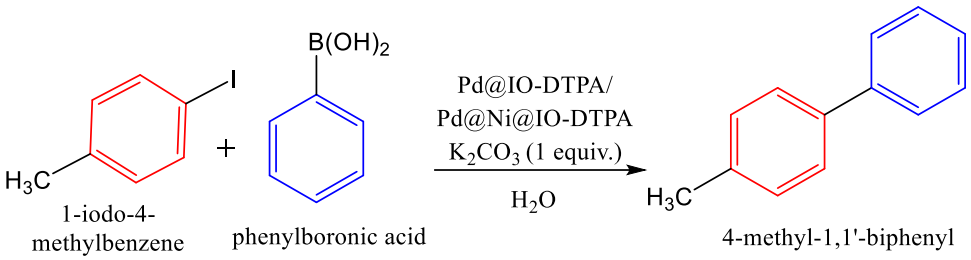

M.P: 49 °C

Molecular weight: 168.24 gm/mol`

Pd@IO-DTPA

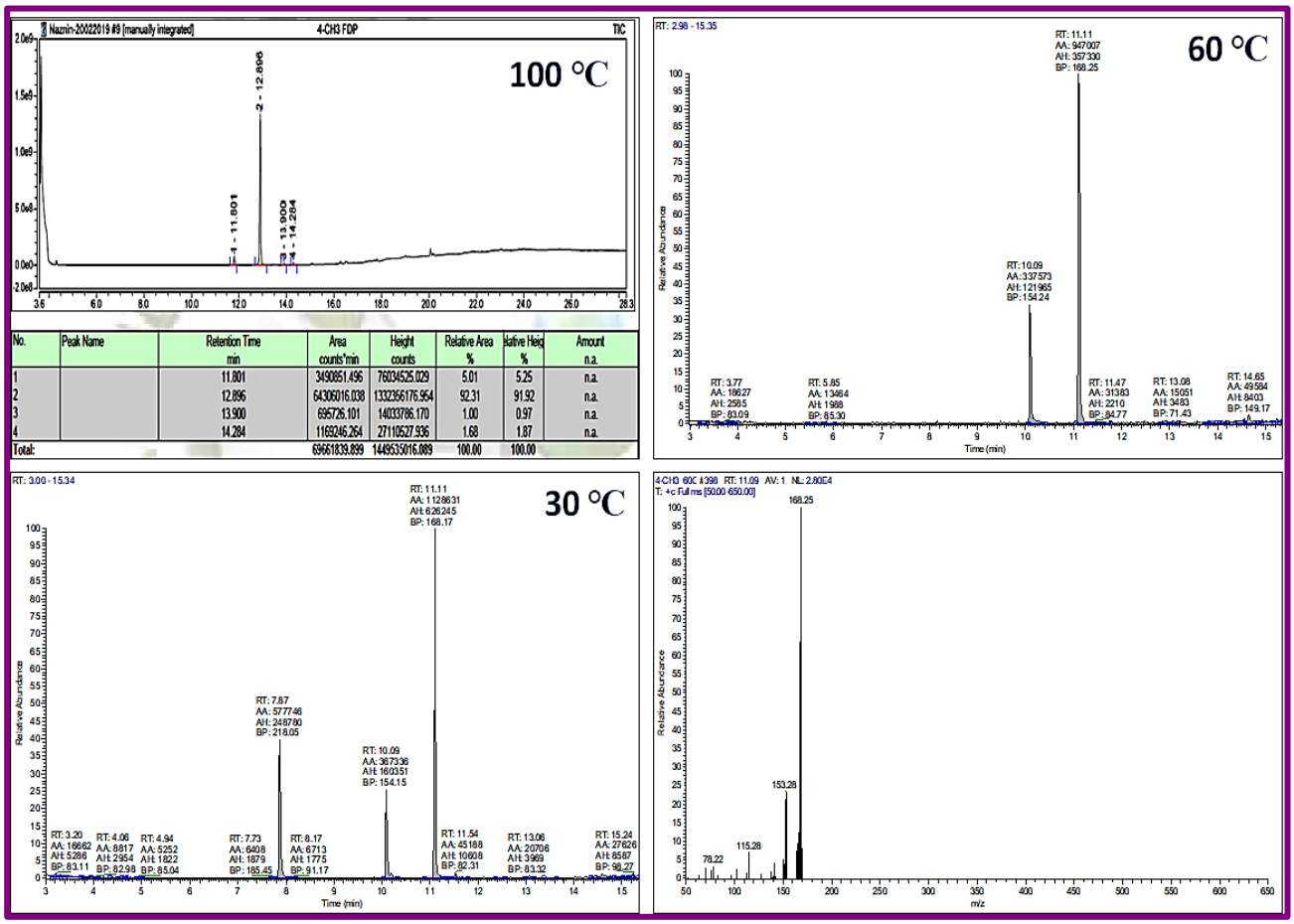

Figure 5.A15: *GC-Ms spectra of crude product (4-methyl-1,1'-Biphenyl) synthesized at RT, 60°C and 100 °C*

Pd@Ni@IO-DTPA

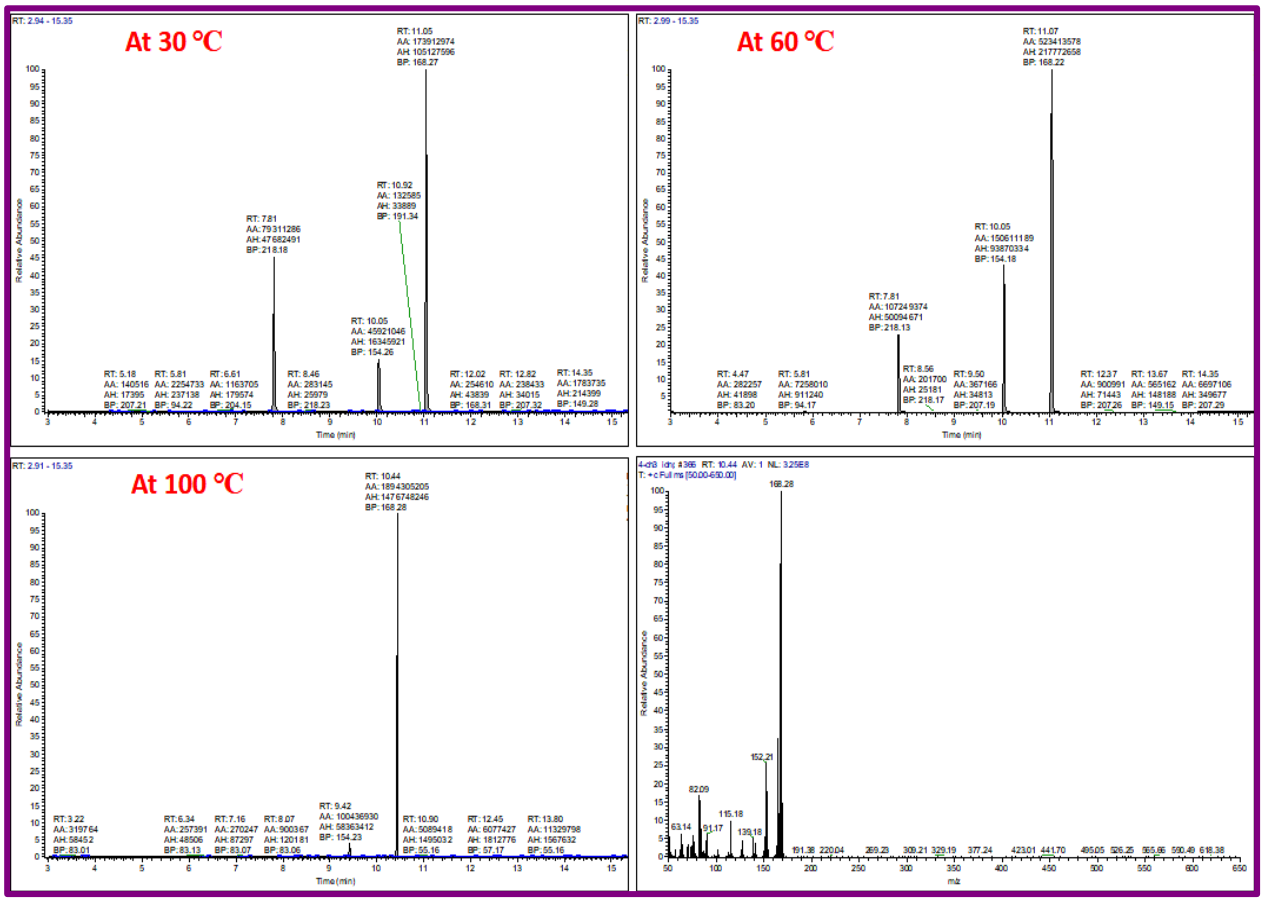

Figure 5.*A16*: *GC-Ms spectra of crude product (4-methyl-1,1'-Biphenyl) synthesized at 30, 60 and 100 °C*

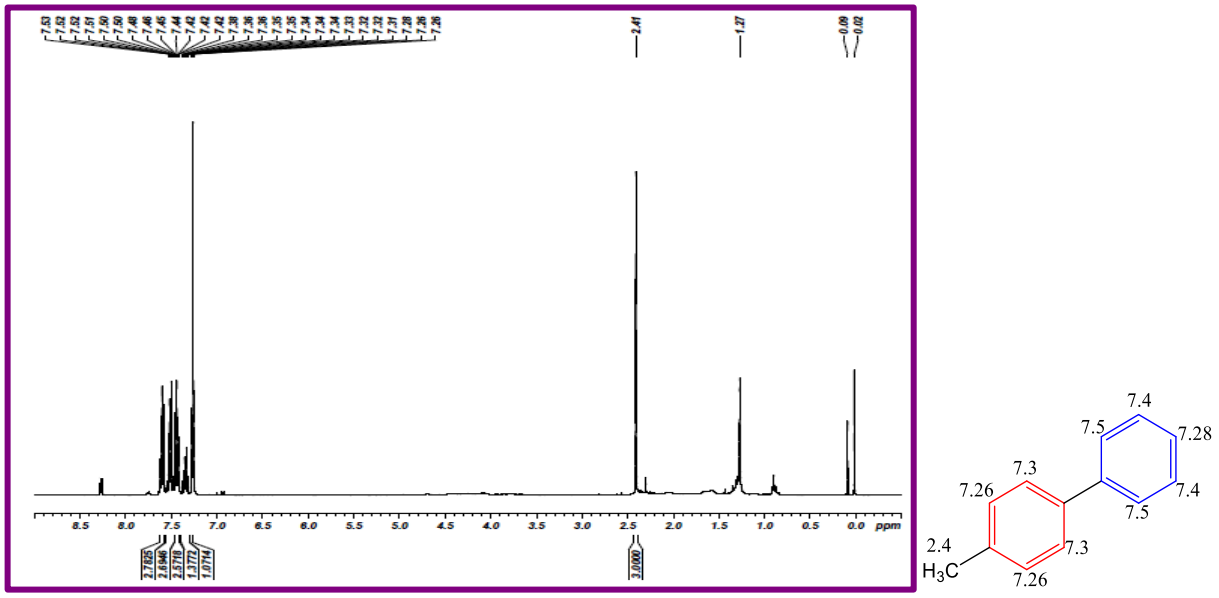

Figure 5.*A17:* *NMR spectra of column purified (4-methyl-1,1'-Biphenyl)*

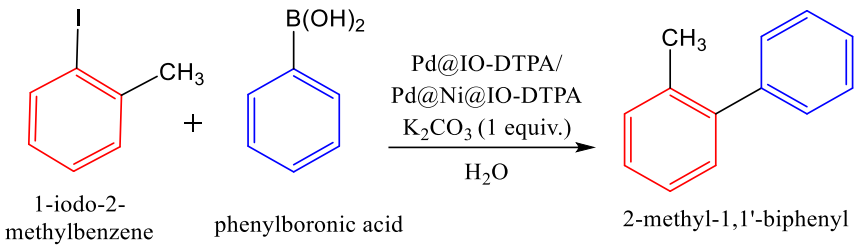

1-iodo-2-methylbenzene phenylboronic acid 2-methyl-1,1'-biphenyl

B.P: 255 °C

Molecular weight: 168.24 gm/mol

Pd@IO-DTPA

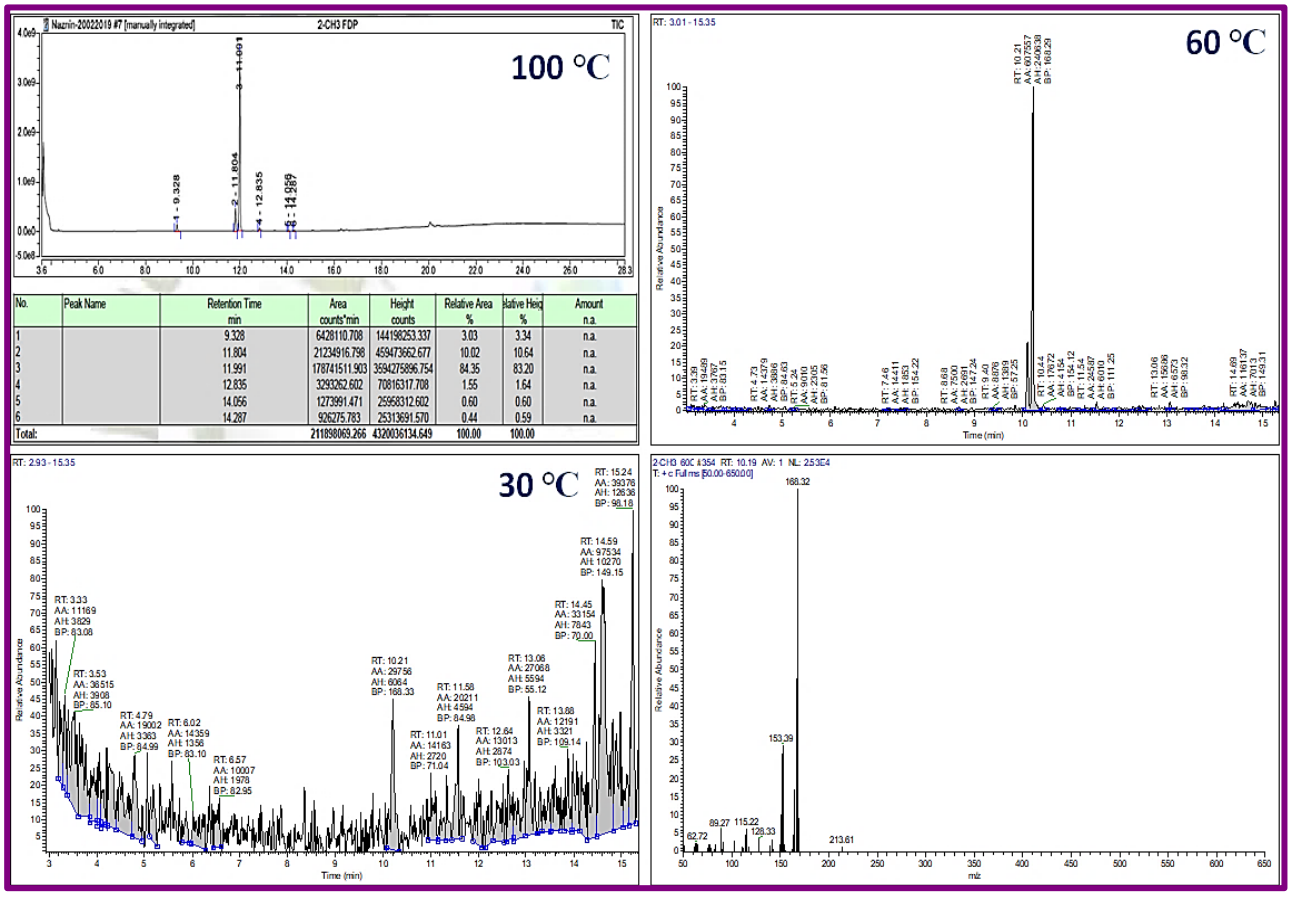

No.	Peak Name	Retention Time min	Area counts*min	Height counts	Relative Area %	Relative Height %	Amount
1		9.328	6428110.708	144198253.337	3.03	3.34	n.a.
2		11.804	21234916.798	459473662.677	10.02	10.64	n.a.
3		11.991	178741511.903	3594275896.754	84.35	83.20	n.a.
4		12.835	3293262.602	70816317.708	1.55	1.64	n.a.
5		14.056	1273991.471	25958312.602	0.60	0.60	n.a.
6		14.287	926275.783	25313691.570	0.44	0.59	n.a.
Total:			211898069.266	4320036134.649	100.00	100.00	

Figure 5.A18: *GC-Ms spectra of crude product (2-methyl-1,1'-Biphenyl) synthesized at RT, 60°C and 100 °C*

Pd@Ni@IO-DTPA

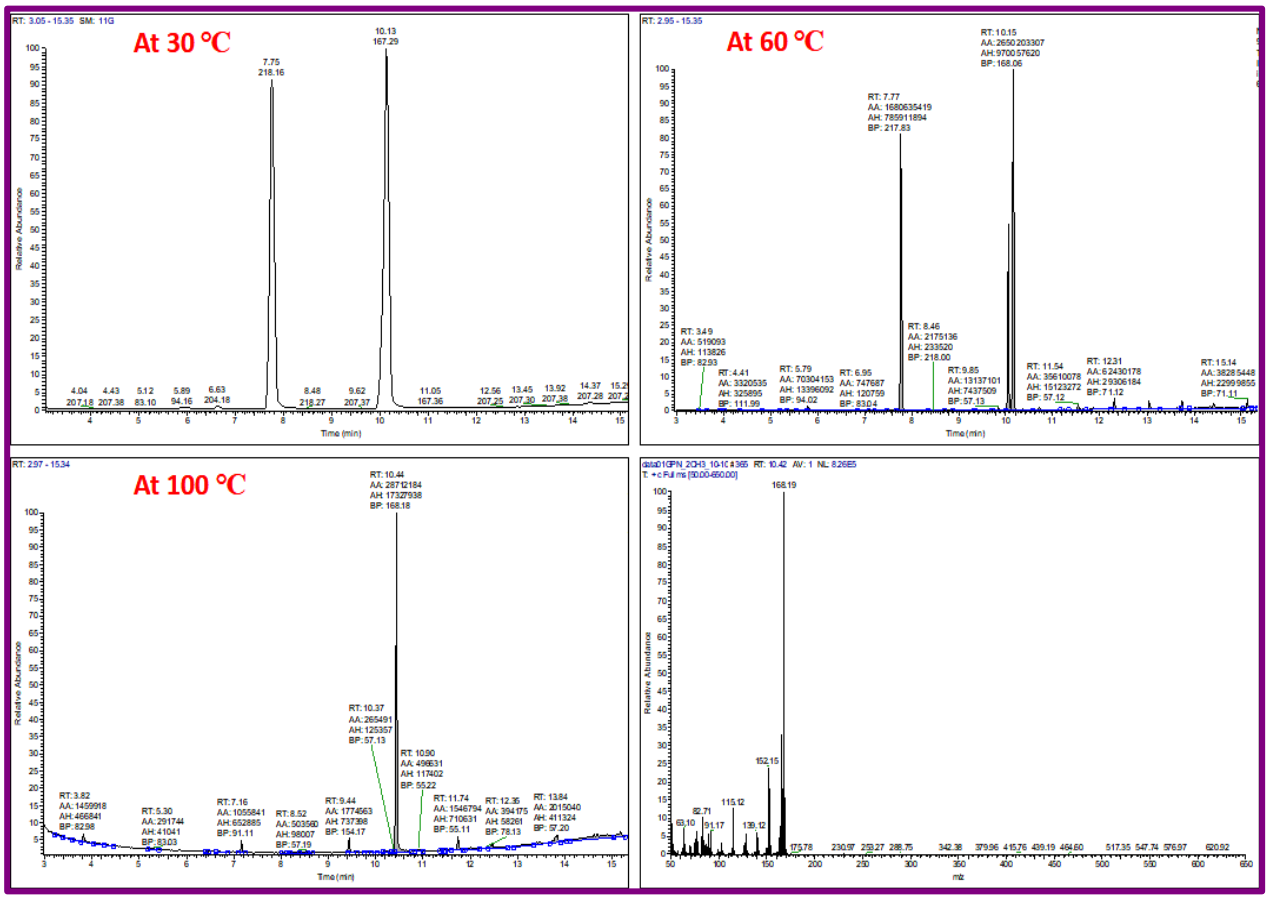

Figure 5.*A19*: *GC-Ms spectra of crude product (2-methyl-1,1'-Biphenyl) synthesized at 30, 60 and 100 °C*

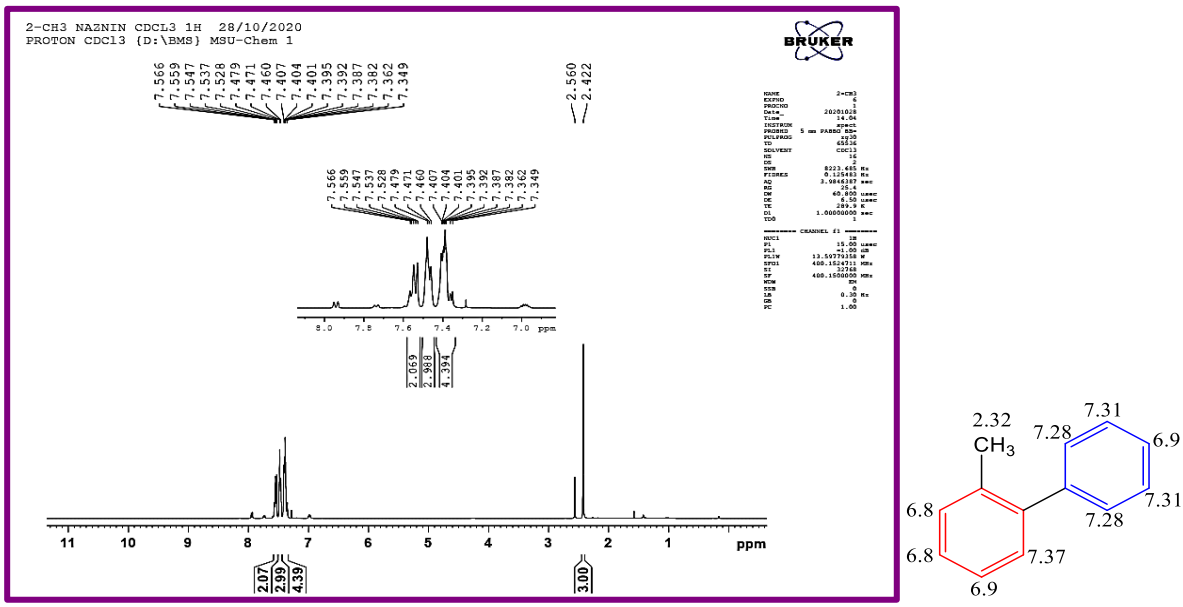

Figure 5.A20: NMR spectra of column purified (2-methyl-1,1'-Biphenyl)

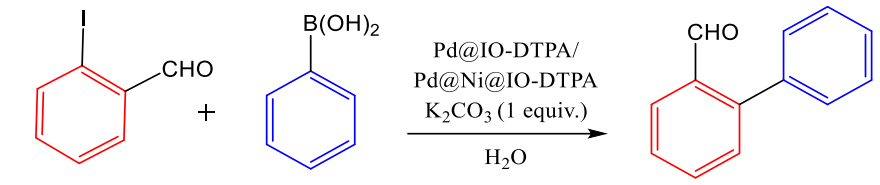

2-iodobenzaldehyde phenylboronic acid [1,1'-biphenyl]-2-carbaldehyde

B.P: 90 °C

Molecular weight: 182.2 gm/mol

Pd@IO-DTPA

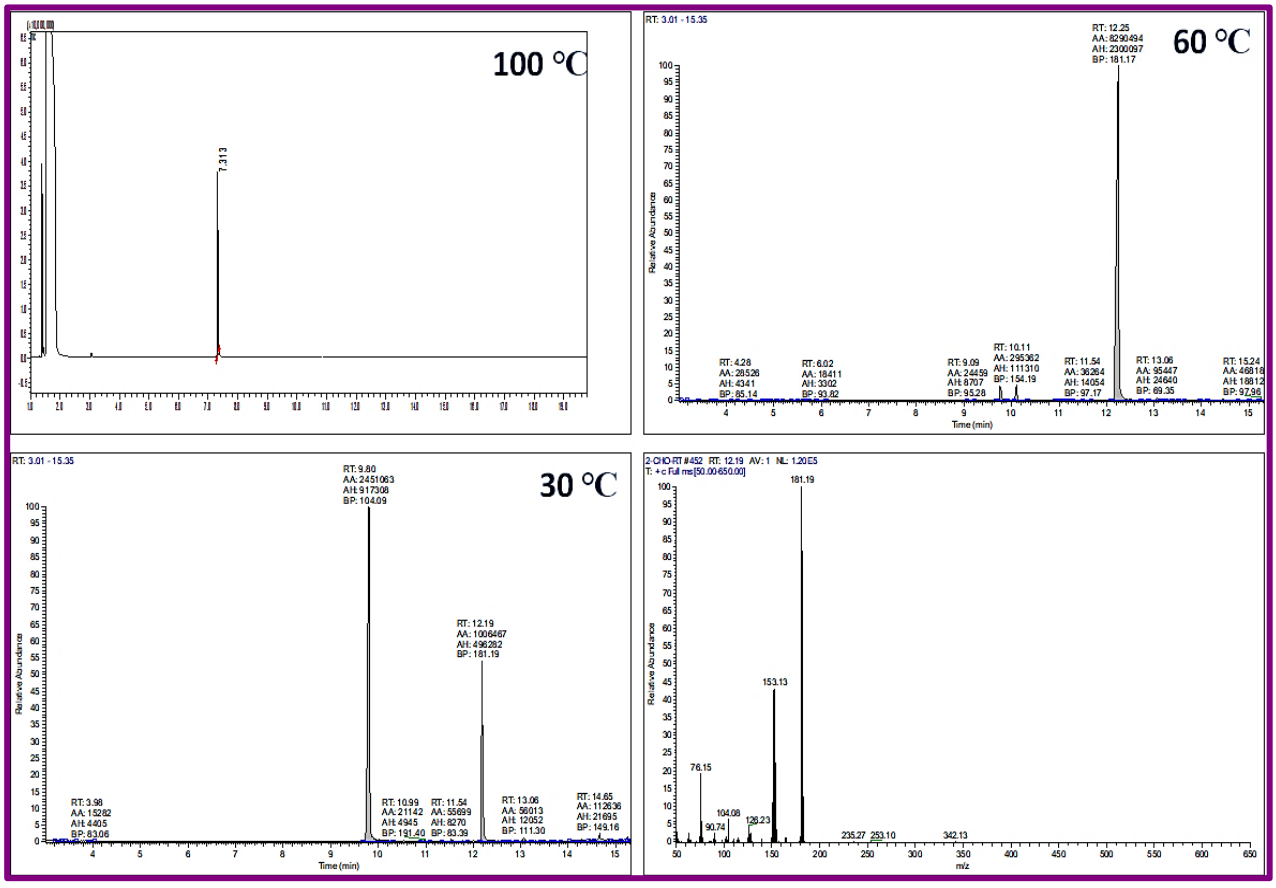

Figure 5.*A21:* *GC-MS spectra of crude product ([1,1'-biphenyl]-2-carbaldehyde) synthesized at RT, 60°C and 100 °C*

Pd@Ni@IO-DTPA

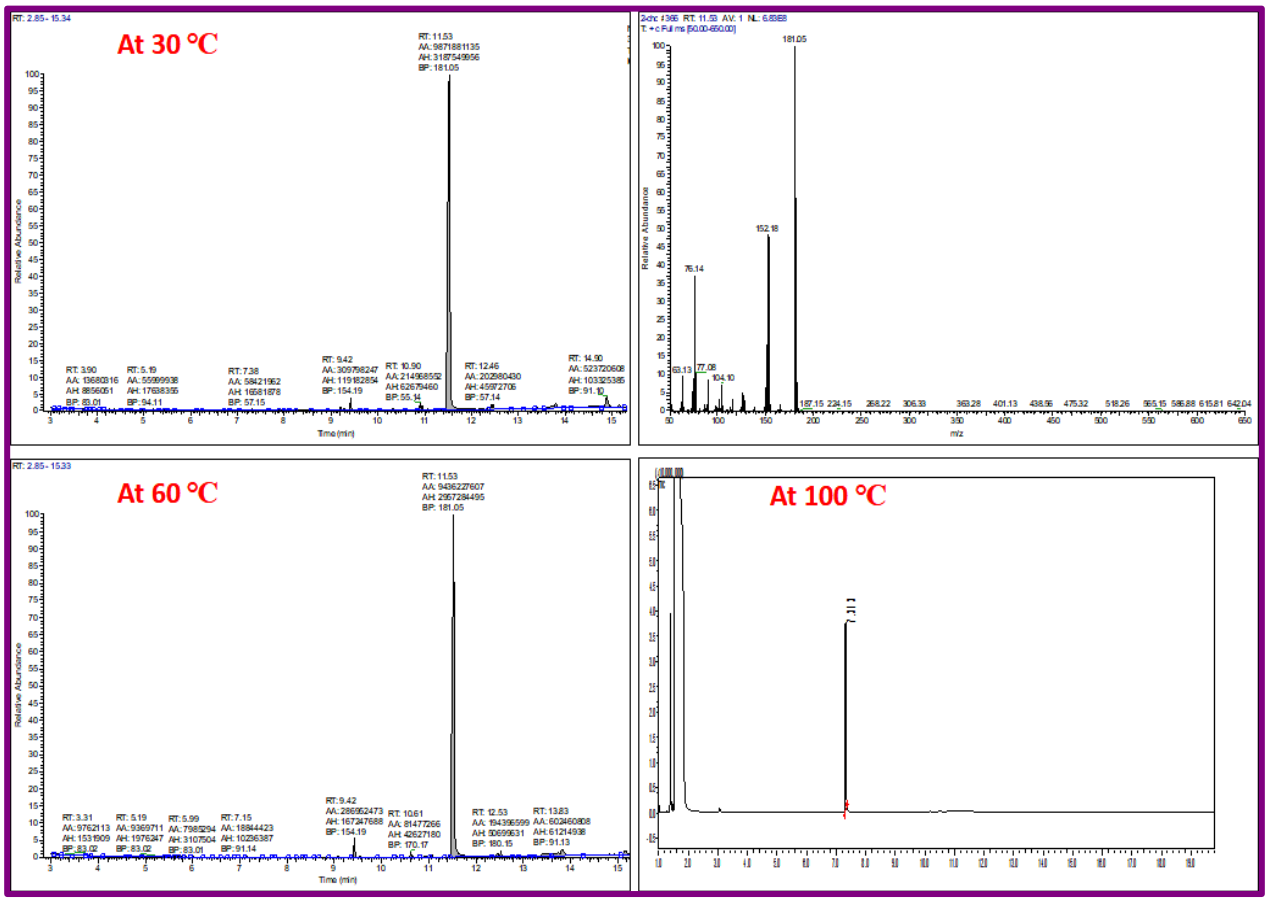

Figure 5.A22: *GC-MS spectra of crude product ([1,1'-biphenyl]-2-carbaldehyde) synthesized at 30°C, 60°C and 100 °C*

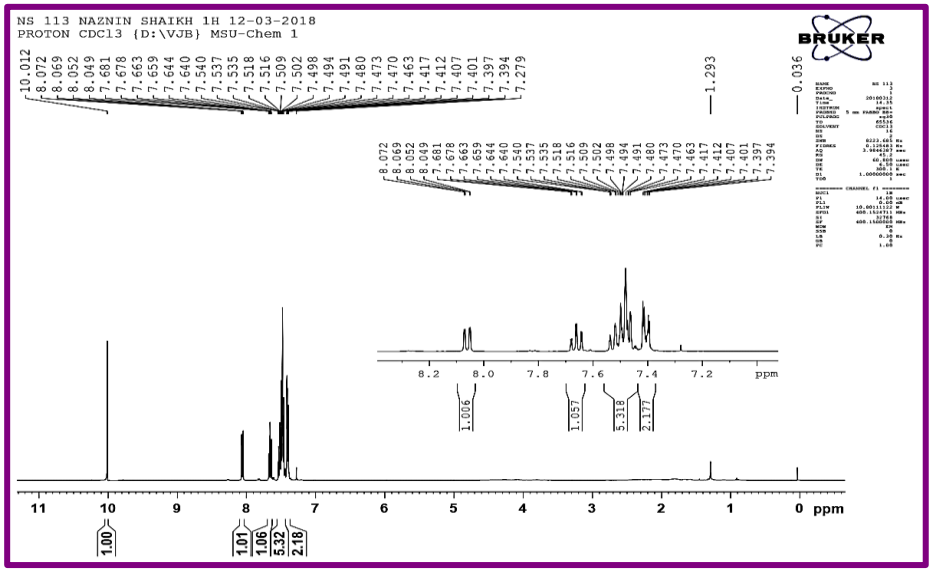

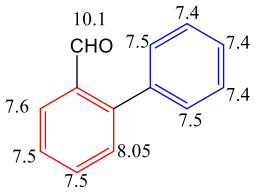

Figure 5.A23: *NMR spectra of column purified ([1,1'-biphenyl]-2-carbaldehyde)*

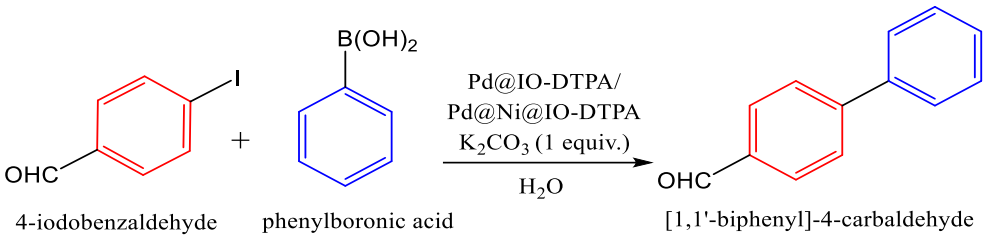

M.P. 60 °C

Molecular weight: 182.2 gm/mol

Pd@IO-DTPA

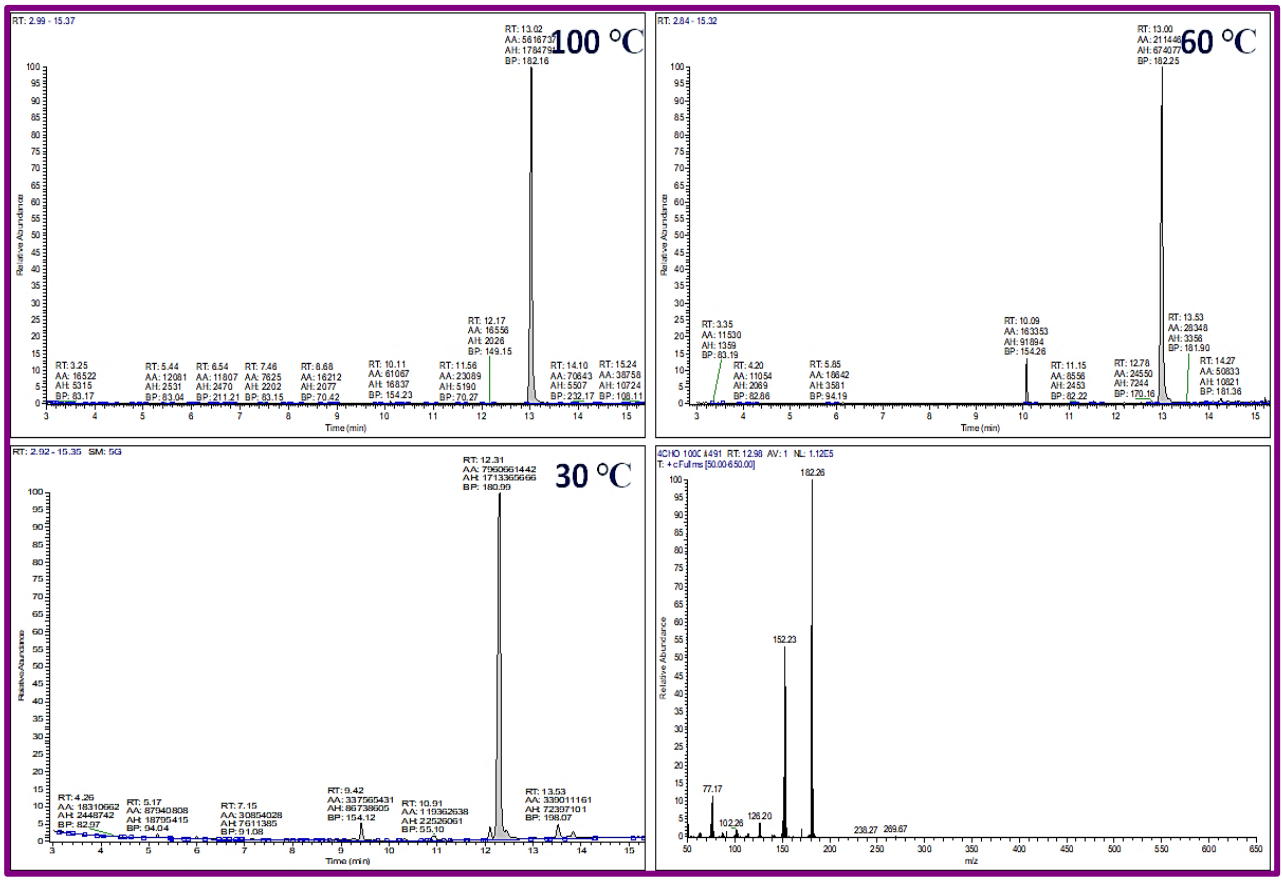

Figure 5.*A24*: *GC-Ms spectra of crude product ([1,1'-biphenyl]-4-carbaldehyde) synthesized at RT, 60°C and 100 °C*

Pd@Ni@IO-DTPA

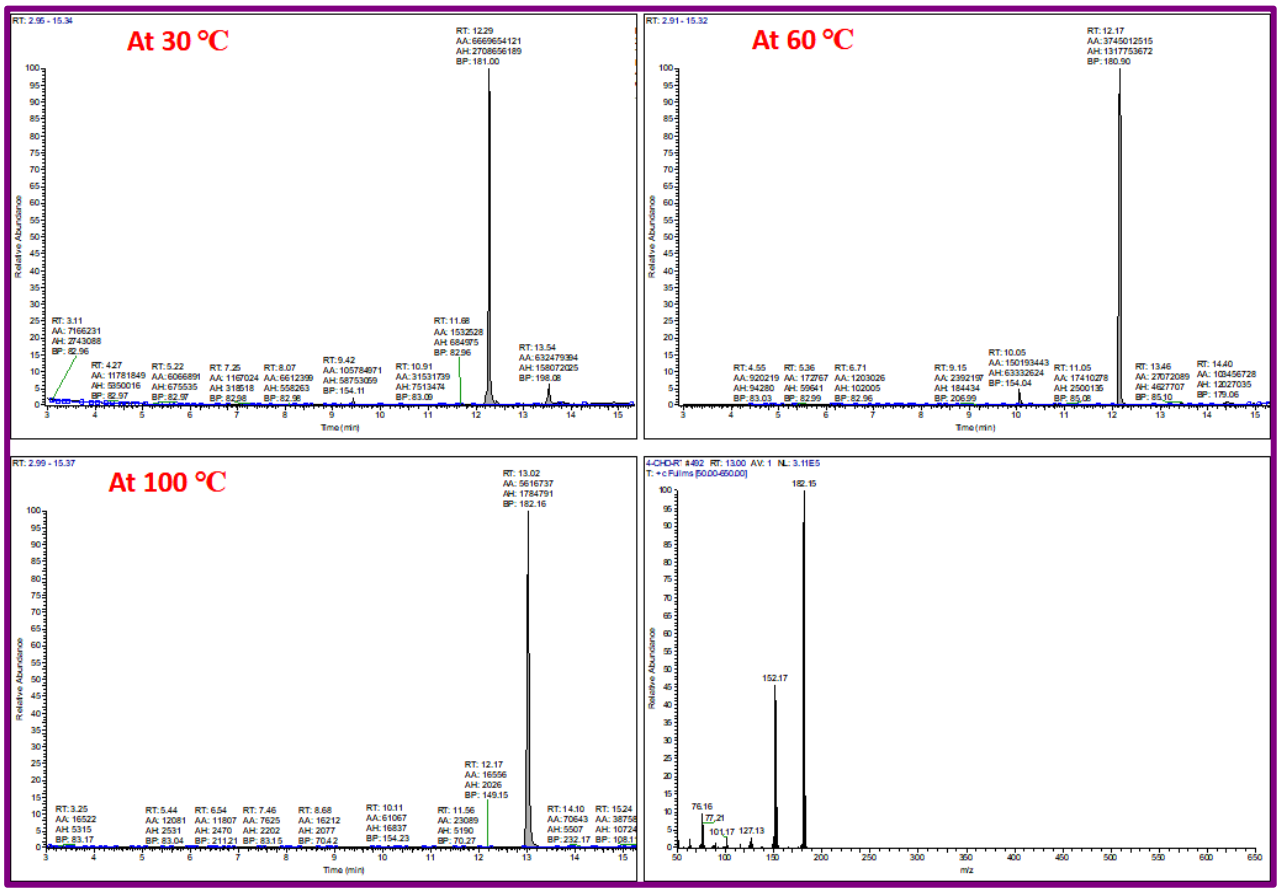

Figure 5.A25: *GC-Ms spectra of crude product ([1,1'-biphenyl]-4-carbaldehyde) synthesized at 30°C, 60°C and 100 °C*

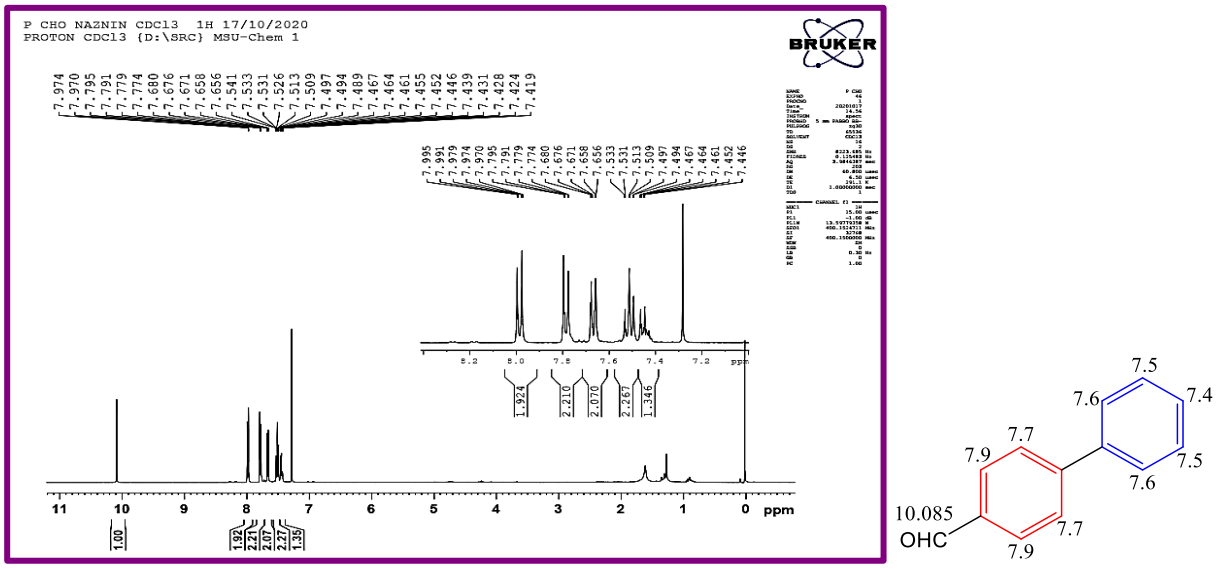

Figure 5.A26: *NMR spectra of column purified ([1,1'-biphenyl]-4-carbaldehyde*

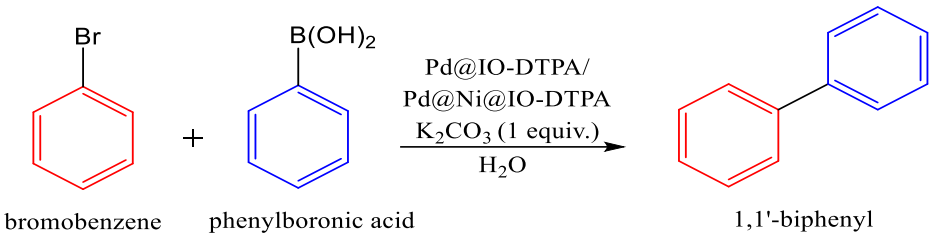

bromobenzene phenylboronic acid 1,1'-biphenyl

M.P: 70 °C

Molecular weight: 154.21 gm/mol

Pd@IO-DTPA

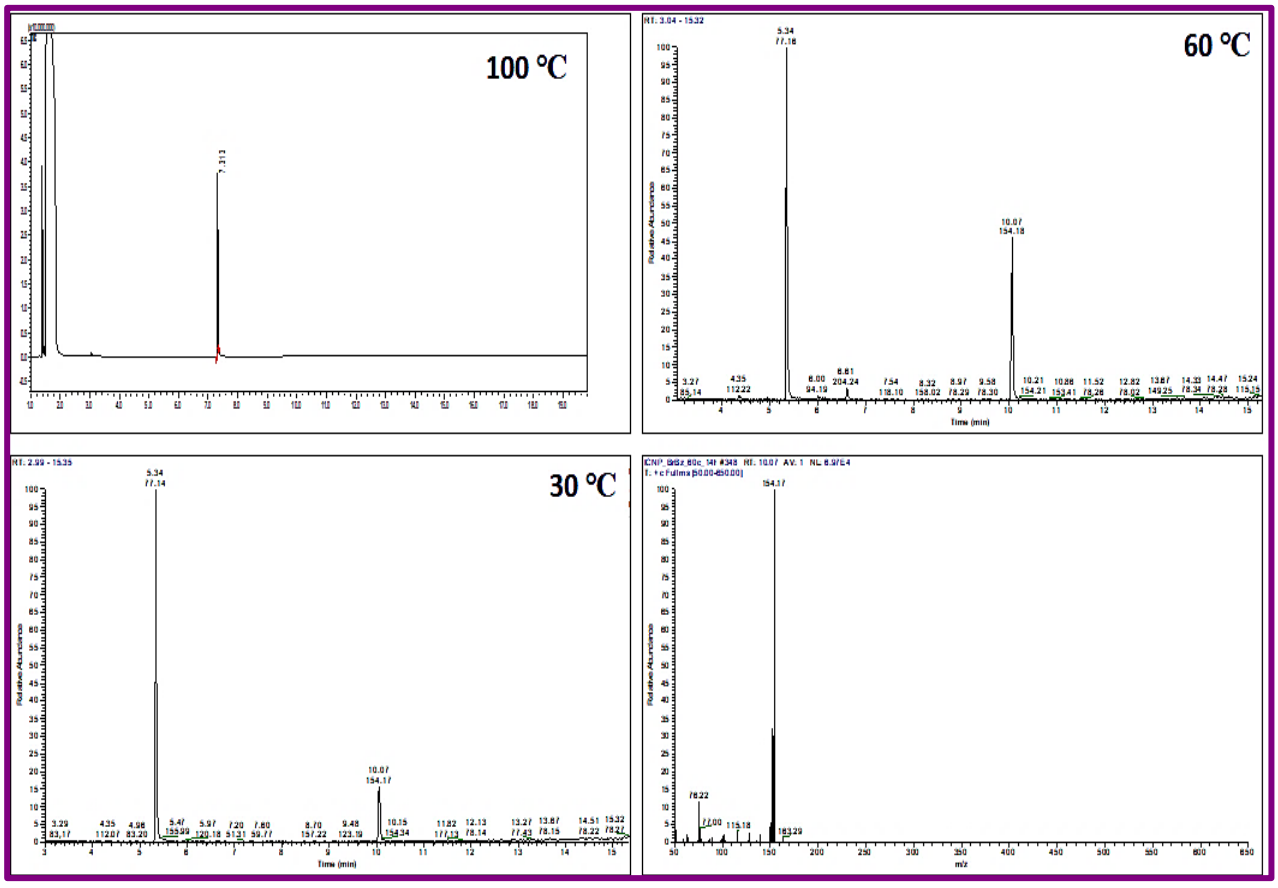

Figure 5.A27: GC-MS spectra of crude product (Biphenyl) synthesized From Bromobenzene at RT, 60°C and 100

Pd@Ni@IO-DTPA

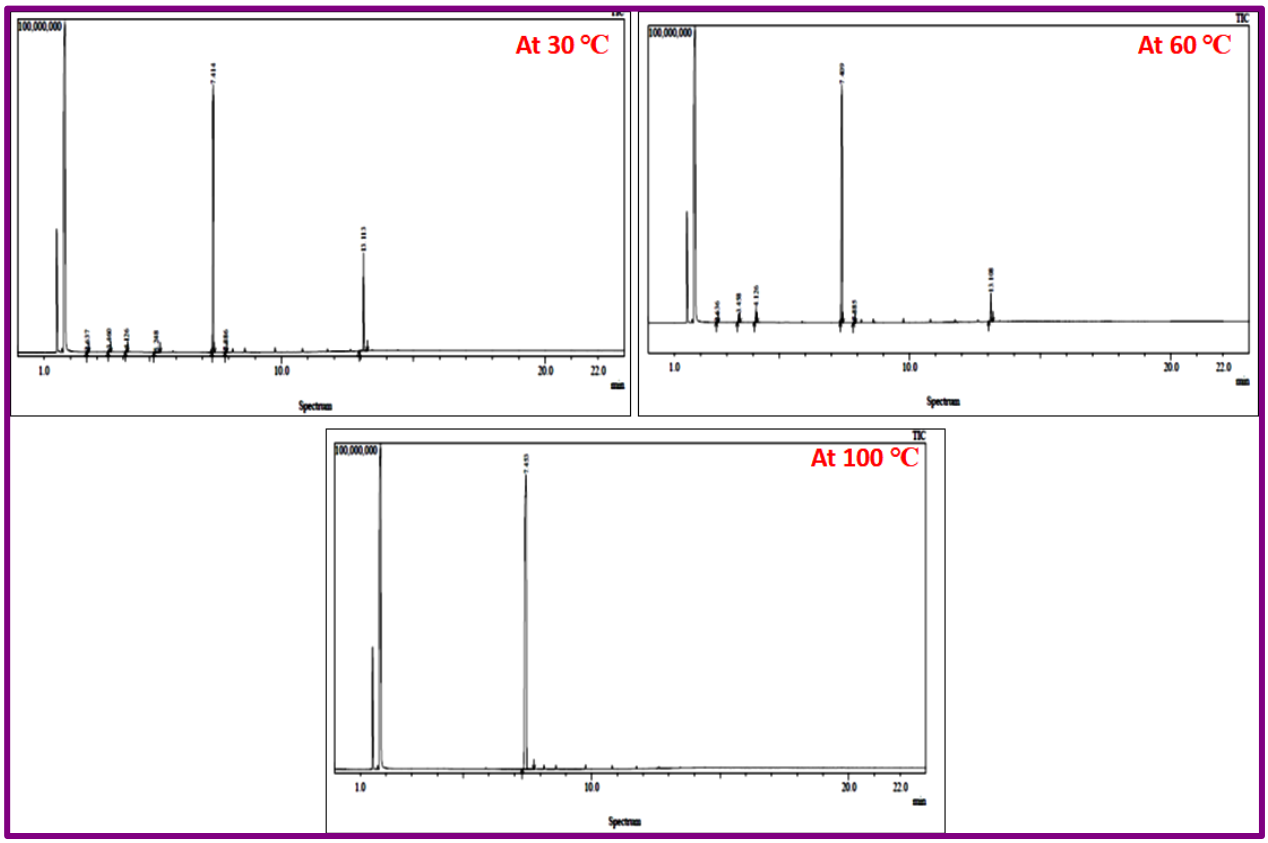

Figure 5.*A28*: *GC-MS spectra of crude product (Biphenyl) synthesized From Bromobenzene at 30°C, 60°C and 100 °C*

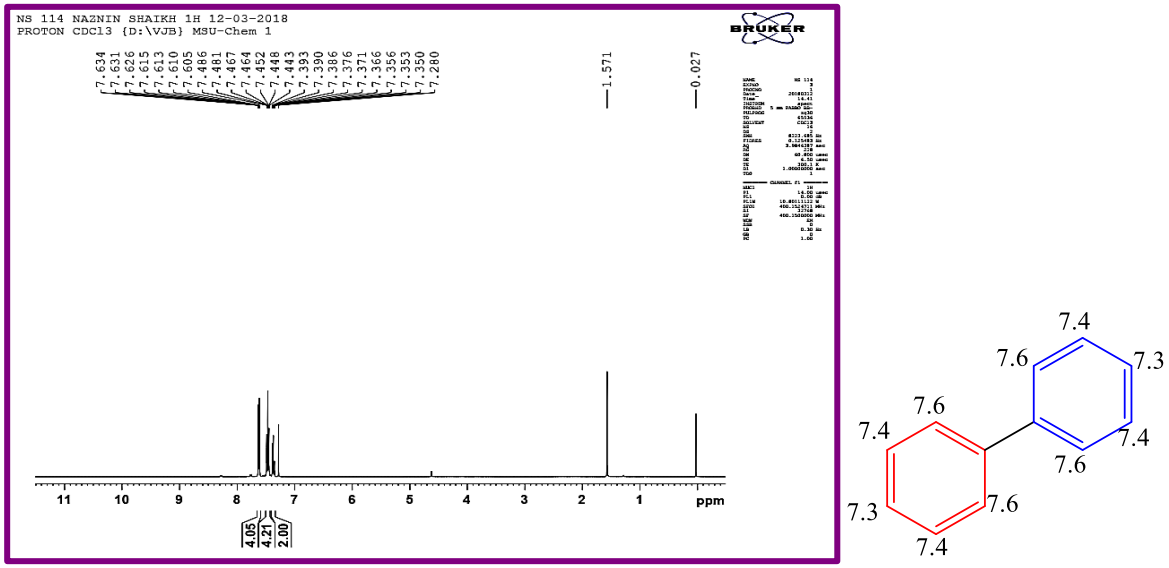

Figure 5.A29 NMR spectra of column purified Biphenyl synthesized From Bromobenzene

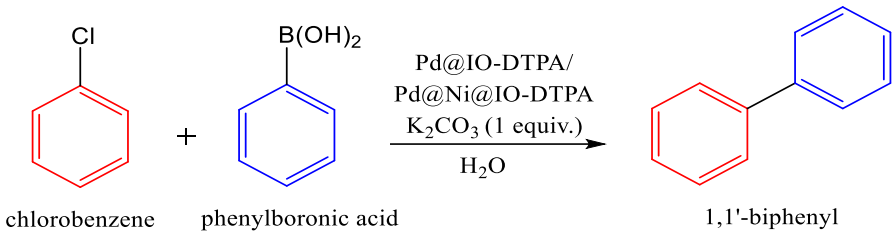

chlorobenzene phenylboronic acid 1,1'-biphenyl

M.P: 70 °C

Molecular weight: 154.21 gm/mol

Pd@IO-DTPA

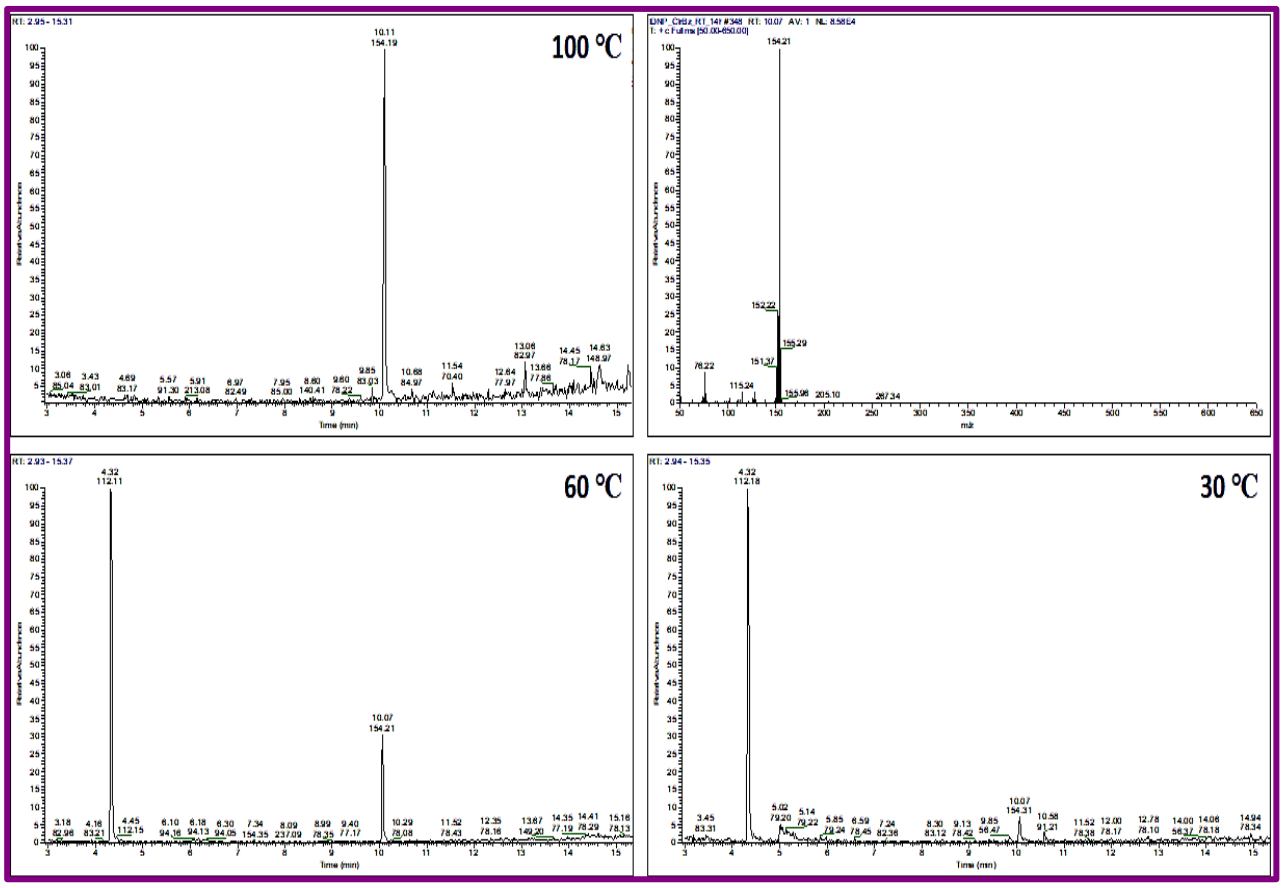

Figure 5.A30: GC-Ms spectra of crude product (Biphenyl) synthesized From Chlorobenzene at RT, 60°C and 100 °C

Pd@Ni@IO-DTPA

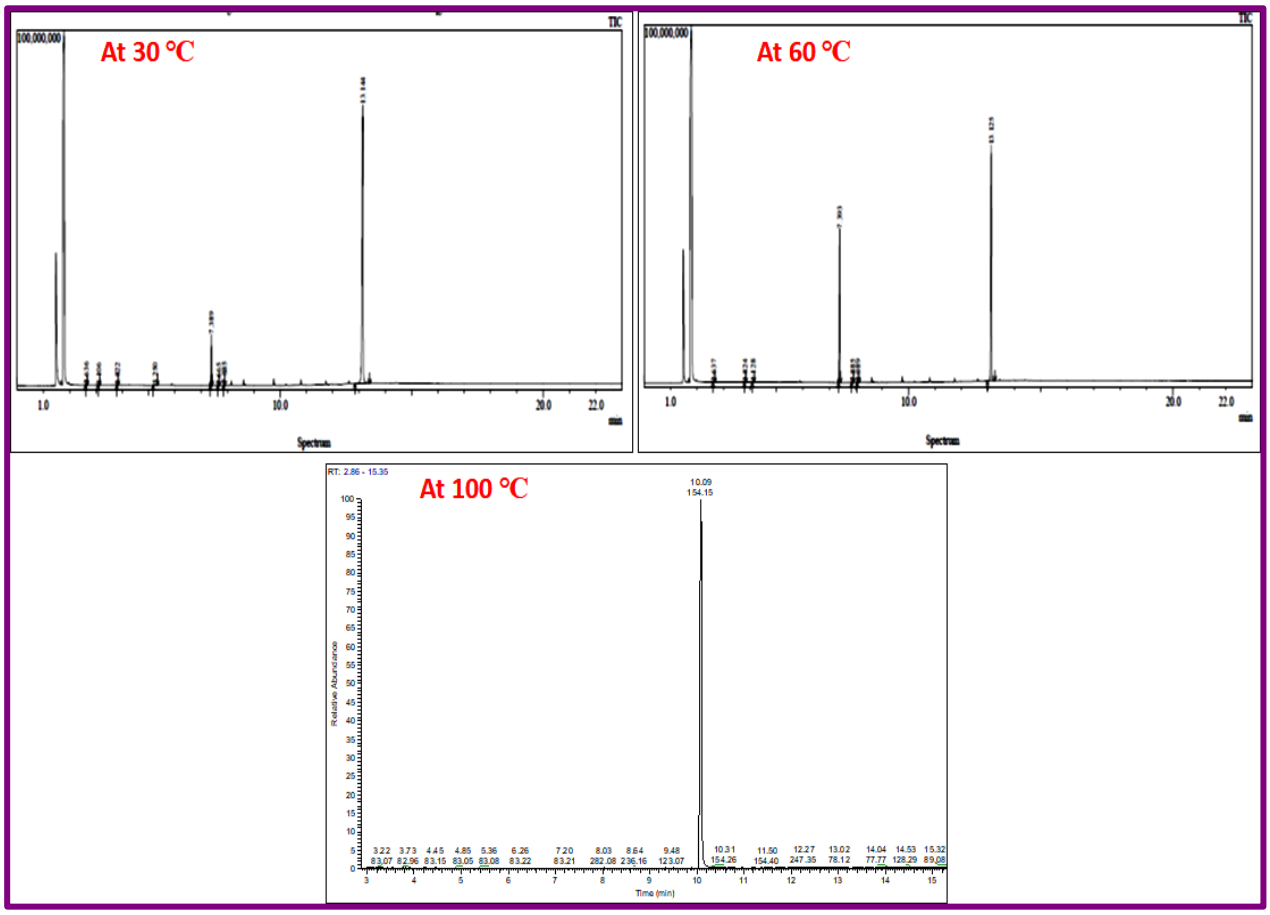

Figure 5.A31: GC-Ms spectra of crude product (Biphenyl) synthesized From Chlorobenzene at RT, 60°C and 100 °C

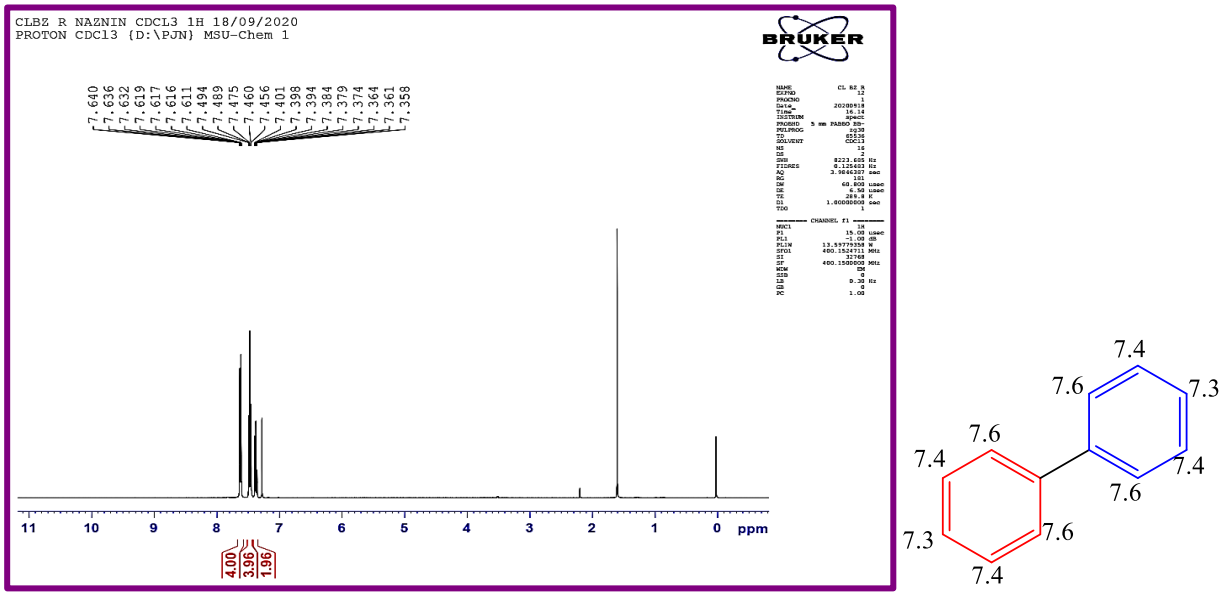

Figure *5.A32**: NMR spectra of column purified Biphenyl synthesized From Chlorobenzene*

Hot filtration test

A hot filtration test was performed under optimized condition to investigate the heterogeneous nature of the catalysts (Pd@Ni@IO-DTPA). After 2 h the catalyst was separated and the reaction was then continued further for 10 h. Products were isolated and analysed with GC-MS

Figure 5.A33: GC-Ms spectra of Hot filtration test for Pd@IO-DTPA

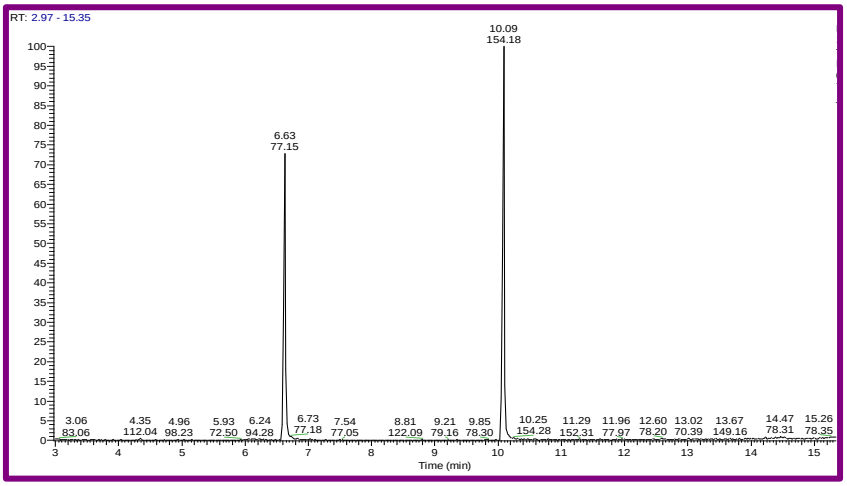

Figure 5.A34: GC-MS spectra of product obtained during Hot filtration test (Pd@Ni@IO-DTPA)

Recycling of catalyst

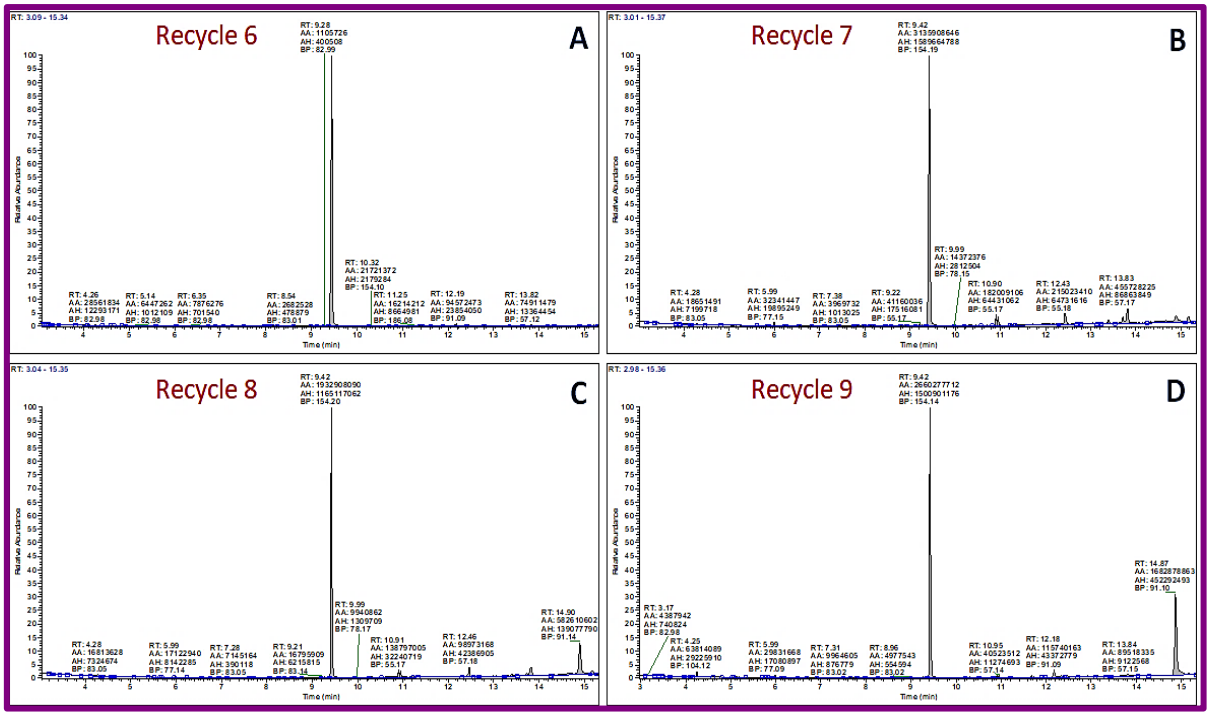

Figure 5.*A35*: *GC-MS spectra of the product for Recycled catalyst (Pd@IO-DTPA) catalysed reaction between Iodobenzene and phenyl boronic acid performed at 100 °C*

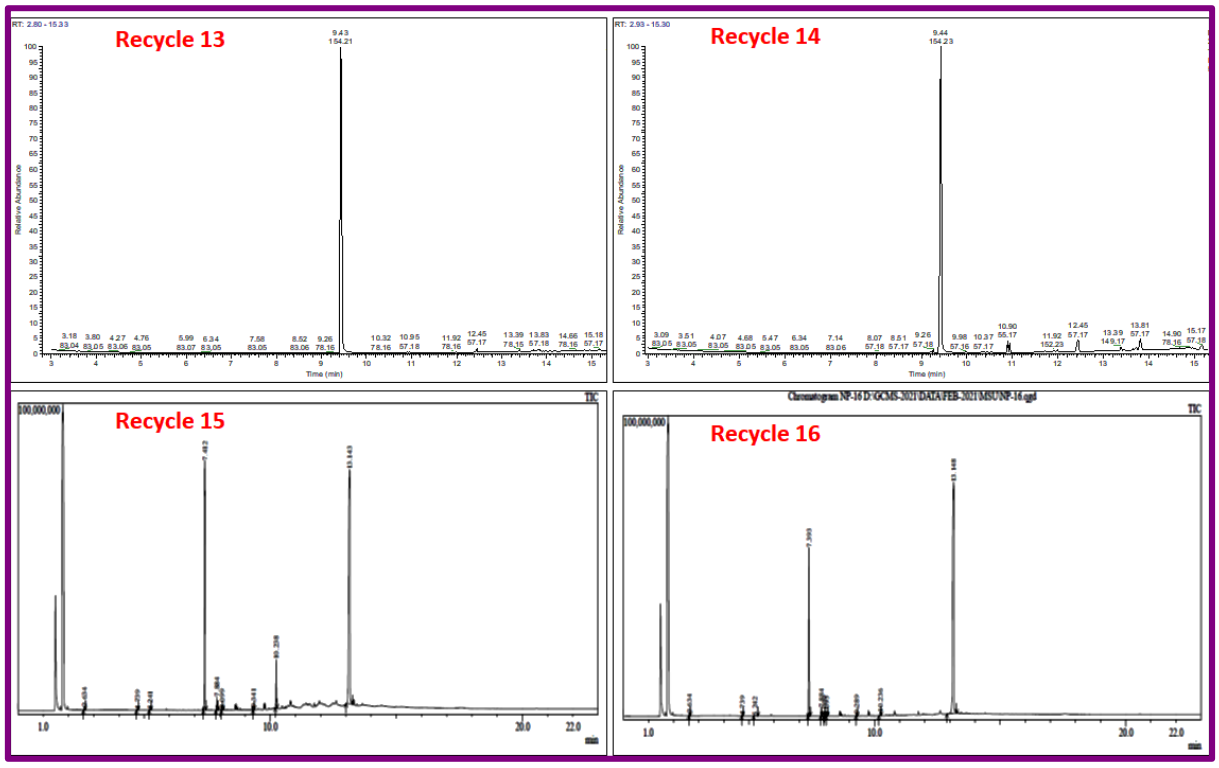

Figure 5.A36: GC-MS spectra of product obtained during Recycling cycle 13, 14, 15, and 16.

Reaction with Ni@IO-DTPA

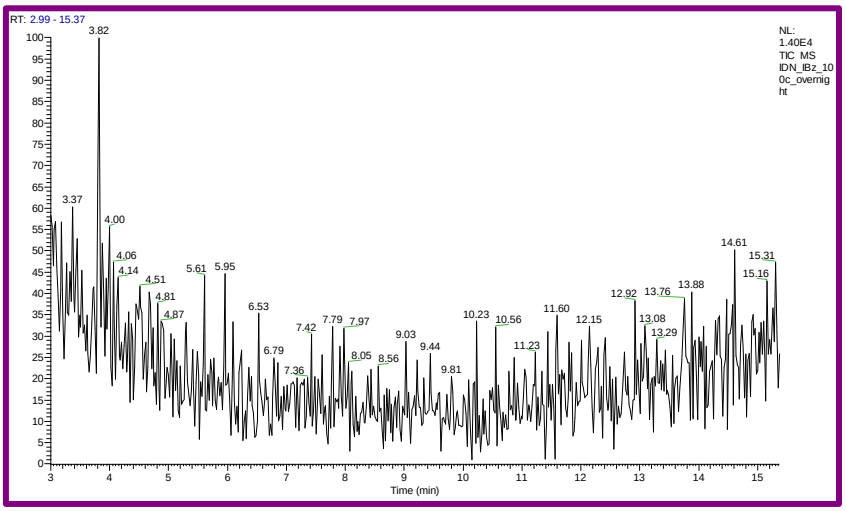

Figure 5.A37: GC-MS spectra of the product for Ni@IO-DTPA catalysed reaction between Iodobenzene and Phenylboronic acid performed using 1 equivalent of K_2CO_3 and at 100°C